Using GNSS to derive new information about Greenland and the Greenland Ice Sheet

Hansen, Karina

Publication date:
2022

Document Version
Publisher's PDF, also known as Version of record

DTU SPACE
National Space Institute

Using GNSS to derive new information about Greenland and the Greenland Ice Sheet

Karina Hansen PhD Thesis

Using GNSS to derive new information about Greenland and the Greenland Ice Sheet

Karina Hansen PhD Thesis
August, 2022

By
Karina Hansen

Cover photo: Karina Hansen, 2020
Published by: DTU, National Space Institute, Elektrovej, building 327 and 328, 2800 Kgs. Lyngby Denmark
www.space.dtu.dk
ISSN: [0000-0000] (electronic version)
ISBN: [000-00-0000-000-0] (electronic version)

ISSN: [0000-0000] (printed version)
ISBN: [000-00-0000-000-0] (printed version)

Summary

The Arctic is currently the region most susceptible to global climate change, experiencing the highest relative temperature rise. Furthermore, the possibility of rapid melt of the Greenland Ice Sheet (GrIS) is ranked among the most serious climate threats to our societies, with its potential contribution to global sea level rise regarded especially ominous. Completely melted the GrIS would be the equivalent to $\sim$7.4 m of global sea level rise. If the current increase in mass loss continues, the Greenland ice sheet alone may account for as much as $\sim$33 cm of global sea level rise by 2100, which is a significant increase compared to the $\sim$2.5 cm it contributed during the last century. The increased mass loss from the Greenland ice sheet and the growing interest in predicting future mass loss makes it increasingly important to unearth past climate, monitor the present and improve model predictions. This PhD project contributes to this by showing three new applications of existing Global Navigation Satellite System (GNSS) data that derive new information about Greenland and the GrIS.

In the first study we presented a novel method to estimate the dynamic ice loss of Greenland's three largest outlet glaciers: Jakobshavn Isbræ, Kangerlussuaq and Helheim. We measured the elastic displacements of the solid Earth caused by dynamic thinning using three Greenland GNSS Network (GNET) stations located near the glacier termini. When we compared our results with discharge, we found a time lag between the onset of dynamic thinning/thickening and glacier speedup/slowdown. Our results showed that dynamic thinning on Jakobshavn Isbræ occur 0.87 ±0.07 years before speedup. This implies that the GNSS time series can be used to predict speedup/slowdown of Jakobshavn Isbræ by up to 10.4 months. For Kangerlussuaq and Helheim the thinning occur 0.37 ±0.17 years (4.4 months) and 0.03 ±0.16 years (11 days) before speed up, respectively.

In the second study, we used ten-year long records of Surface Elevation Change (SEC) derived from three GNSS stations placed in the interior of the GrIS to assess the ability of CryoSat-2 radar altimetry to capture SEC during 2010-2021. We used GNSS Interferometric Reflectometry (GNSS-IR) to derive the best possible time series of continuous daily surface elevations. We compared GNSS derived SEC with CryoSat-2 derived SEC and found CryoSat-2 performs best at the northernmost GNSS site with a maximum difference of 12 cm. The strength of assessing satellite radar altimetry against permanent GNSS stations lie in the GNSS-IR methods ability to provide a continuous daily time series that capture both long-term and extreme short-term changes. Furthermore, we calculated the yearly SEC ($\partial h/\partial t$) for every available date pair in the GNSS derived surface elevation time series. We found $\partial h/\partial t$ varies throughout the year and that an April to April ice sheet wide $\partial h/\partial t$ campaign would represent the average $\partial h/\partial t$ from GNSS the best.

In the third study we used data from the GNET station at Station Nord (NORD) to demonstrate GNSS-IR can be used to derive terrain corrected snow thickness on Greenland bedrock. We identified snow free time periods and used the GNSS-IR results to estimate a 360° summer surface topography profile, which we then used as a reference for estimating snow thickness. We found the snow thickness generally increased throughout winter, where the snow surface builds up to an approximately flat surface despite bedrock topography, which results in big differences in snow thickness. Furthermore, we found the distinct pattern of the average snow thickness time series can be used to identify the onset of melt.

Resumé

Oversættelse af Julie Hansen

Brug af GNSS data til at undersøge forskellige aspekter af Grønland og Indlandsisen

Arktis er i dag det sted i verden, der er mest udsat i forhold til klimaforandringer, og hvor der opleves de højeste relative temperaturstigninger. Derudover regnes risikoen for, at indlandsisen på Grønland smelter og den havniveaustigning, som dette vil medføre, som en af de mest alvorlige klimatrusler mod vores samfund. En fuld afsmeltning af indlandsisen vil medføre en havniveaustigning på omkring 7,4 meter verden over. Fortsætter den nuværende stigning i massetab fra indlandsisen, vil afsmeltningen fra indlandsisen medføre en havniveaustigning verden over på op mod 33 cm i det 21. århundrede. Til sammenligning bidrog indlandsisen med en havniveaustigning på 2,5 cm i det 20. århundrede.

Indlandsisens tiltagende massetab og den stigende interesse i at kunne forudsige fremtidige massetab gør det tiltagende vigtigt at afdække tidligere klima, monitorere det nuværende klima og forbedre de modeller, der kan forudsige fremtidigt klima. Denne PhD-afhandling bidrager til dette ved at vise, hvordan eksisterende data fra Global Navigation Satellite System (GNSS) stationer på Grønland kan bruges til at udlede ny information om Grønland og Indlandsisen.

I afhandlingens første studie præsenteres en ny metode til at estimere den dynamiske kælving fra Grønlands tre største udløbsgletsjere Jakobshavn Isbræ, Kangerlussuaq og Helheim. Ved brug af tre Greenland GNSS Network (GNET) stationer nær gletsjerfronten måles jordens elastiske forskydning forårsaget af dynamiske tykkelses ændringer. Ved at sammenligne disse resultater med gletsernes kælving fandt vi en forsinkelse mellem de dynamiske tykkelsesændringer og gletsjernes hastighed. Resultaterne viser, at den dynamiske tykkelsesændring af Jakobshavn Isbræ sker 0.87 ±0.07 år før gletsjerens hastighedsændring hvilket indikerer, at GNSS tidsserier kan bruges til at forudsige hastighedsændringer af Jakobshavn Isbræ op til 10.4 måneder før de finder sted. For Kangerlussuaq og Helheim sker tykkelsesændringen henholdsvis 0.37 ±0.17 år (4.4 måeneder) og 0.03 ±0.16 år (11 dage) før hastighedsændringen.

I afhandlingens andet studie bruges ti års målinger af højdeændringer i overfladen fra tre GNSS stationer midt på indlandsisen og tilsvarende højdemålinger fra CryoSat-2 til at vurdere CryoSat-2's evne til at måle højdeændringer. Vi brugte GNSS interferometric reflectometry (GNSS-IR) til at udlede den bedst mulige daglige overfladehøjde-tidsserie. Ved at sammenligne overfladeelevationsændringer udledt fra GNSS og overfladeelevationsændringer udledt fra CryoSat-2 fandt vi, at CryoSat-2 giver mest præcise resultater ved den nordligste GNSS station, hvor den maksimale difference mellem resultaterne er 12 cm. Styrken ved at vurdere højdemålinger fra radar over for permanente GNSS stationer ligger i GNSS-IR metodens mulighed for at udlede sammenhængende, daglige tidsintervaller, der viser både langsigtede ændringer og ekstreme, kortsigtede ændringer. Derudover udregnede vi den årlige overfladeelevationsændring ($\partial h/\partial t$) for alle dato-par i den GNSS udledte overfladeelevationstidsserie og fandt, at $\partial h/\partial t$ varierer gennem året og at april er den bedste måned at lave en $\partial h/\partial t$ kampange, der inkluderer hele Indlandsisen.

I afhandlingens tredje studie bruges data fra GNET-stationen på Station Nord (NORD) til at demonstre, hvordan GNSS-IR kan bruges til at udlede den terræn-korrigerede snetykkelse på det grønlandske grundfjeld. Vi identificerede snefri perioder og brugte resultaterne fra GNSS-IR til at estimere en 360° sommer topografi-profil, som vi brugte som reference for at estimere snetykkelsen. Vi fandt på den baggrund, at snetykkelsen generelt stiger gennem vinteren, hvor sneoverfladen bygges op til en næsten flad overflade. Derudover fandt vi, at karakteristiske mønstre i den gennemsnitlige snetykkelsestidsserie kan bruges til identificere, hvornår smeltesæsonen starter.

Preface

This PhD thesis was prepared at the National Space Institute at the Technical University of Denmark (DTU Space) and submitted in fulfillment of the of the requirements for obtaining a PhD degree. The PhD project took place between September 2019 and August 2022 under the Supervision of Professor Shfaqat Abbas Khan and co-supervision of Professor Per Knudsen from DTU Space.

During the PhD project I got the opportunity to attend a couple of conferences, even though many conferences were canceled and/or moved due to COVID-19. In December 2021 I gave an invited oral presentation at AGU in New Orleans. In May 2022 I gave an oral presentation at EGU in Vienna.

The original plan for an external research stay was not possible due to COVID-19. Instead I had my external research stay at the Glaciology and Climate department at The National Geological survey of Denmark and Greenland (GEUS) in March 2022.

Karina Hansen
August, 2022

Acknowledgements

I would like to express my gratitude to my supervisors, Shfaqat Abbas Khan and Per Knudsen for their guidance and support.

I am grateful to William Colgan and Lars Stenseng for the crucial help and fruitful scientific discussion at different moments of the PhD. Many thanks to Rebecca Jackson for proof-reading this thesis and to my sister Julie Hansen for making sure the danish parts of this thesis are understandable. Thanks to Signe Bech Andersen for making my last minute external research stay at GEUS possible at such short notice and to all at the Glaciology and Climate department for making me feel right at home.

Thanks to all my colleagues at the GEO-department at DTU Space, to Ole Baltazar Andersen and Mads Ehrhorn for bringing cake during the final months of this PhD, to the lunch club reminding me breaks are a key part of a productive workday and finally to Nicolaj Hansen for keeping me sane during the final month.

Many thanks to my family and friends for supporting my and to August for his love and ability to make me smile when I return home from the office tired and hangry. Finally, special thanks to my mother for teaching me read and to my father for always pushing my limits, without them I surely wouldn't have been able to complete this PhD.

List of Papers

This project fed into one peer-reviewed paper, one paper submitted to a peer-reviewed journal and one manuscript presented in this thesis.

I. K. Hansen, M. Truffer, A. Aschwanden, K. Mankoff, M. Bevis, A. Humbert, M. R. van den Broeke, B. Noël, A. Bjørk, W. Colgan, K. H. Kjær, S. Adhikari, V. Barletta, and S. A. Khan. Estimating ice discharge at greenland's three largest outlet glaciers using local bedrock uplift. *Geophysical Research Letters*, 48(14):e2021GL094252, 2021

II. K. Hansen, W. Colgan, K. M. Larson, M. J. Willis, V. Helm, and S. A. Khan. Assessment of esa cryosat-2 radar altimetry data using gnss data at three sites on the greenland ice sheet, a. submitted to Journal of Geophysical Research: Earth Surface

III. K. Hansen, T. S. Dahl-Jensen, and L. Stenseng. Terrain corrected snow thickness from gnss-ir at station nord, b. draft intended for submission to the GEUS bulletin

List of Figures

Acronyms

3D three-dimensional.

BeiDou BeiDou Navigation Satellite System.

CryoSat-2 Cryosphere satellite.

DEM Digital elevation model.

ERS European Remote Sensing satellite.

ESA European Space Agency.

Galileo European Global Navigation Satellite System.

GIA Glacial Isostatic Adjustments.

GLISN Greenland Ice Sheet Monitoring Network.

GLONASS Global'naya Navigatsionnaya Sputnikovaya Sistema.

GLS1-3 GLS1, GLS2 and GLS3.

GNET Greenland GNSS Network.

GNSS Global Navigation Satellite System.

GNSS-IR Global Navigation Satellite System Interferometric Reflectometry.

GPS Global Positioning System.

GRACE Gravity Recovery and Climate Experiment.

GRACE-FO Gravity Recovery and Climate Experiment Follow On.

GRACE/-FO Gravity Recovery and Climate Experiment/ Follow On.

GrIS Greenland Ice Sheet.

ICEBridge airborne altimetry Bridge between ICESat satellites.

ICESat Ice, Cloud and land Elevation Satellite.

ICESat-2 Ice, Cloud and land Elevation Satellite 2.

IOM Input-Output Method.

IPCC Intergovernmental Panel on Climate Change.

IRNSS Indian Regional Navigation Satellite System.

PROMICE Programme for Monitoring of the Greenland Ice Sheet.

QZSS Quasi-Zenith Satellite System.

RACMO2.3p2 Regional Atmospheric Climate Model.

RH Reflector Height.

SEC Surface Elevation Change.

SMB Surface Mass Balance.

SNR carrier to noise ratio.

Contents

CHAPTER 1

Introduction

1.1. Motivation

The Arctic is currently the region most susceptible to global climate change, experiencing the highest relative temperature rise (Moon et al., 2021; Meredith et al., 2019). Furthermore, the possibility of rapid melting of the Greenland Ice Sheet (GrIS) is ranked among the most serious climate threats to our societies (Lenton et al., 2008). Especially ominous is its potential contribution to global sea level rise, but the increased supply of melt water to the salinity sensitive North Atlantic may also have dire consequences for the thermohaline circulation on a global scale (Levermann et al., 2012).

The GrIS is by far the largest freshwater reservoir in the Northern Hemisphere, with an ice volume of approximately $2.96 \cdot 10^6$ km^3 (Bamber et al., 2013). If melted completely, this is the equivalent to approximately 7.4 m of global sea level rise. In 2007 the Intergovernmental Panel on Climate Change (IPCC) estimated the GrIS had a yearly contribution to sea level rise of 0.21 ±0.07 mm yr^{-1} during 1993-2003, based on an annual mass loss in that period of 50 to 100 Gt yr^{-1} (IPCC, 2007). In 2006 Rignot and Kanagaratnam (2006) reported an increased mass loss from the GrIS, with an estimated loss of about 244 ±41 Gt yr^{-1} in 2005, which is equivalent to a 0.57 ±0.1 mm yr^{-1} contribution to global sea level rise. A further increase of mass loss was found between 2018-2020, where the yearly loss was approximately 270 Gt yr^{-1} (Nicolaj Hansen, personal communication, July 5, 2022). If the increase in mass loss continues, the GrIS alone may account for as much as 33 cm of global sea level rise by 2100 (Aschwanden et al., 2019), which is a significant increase compared to the GrIS contribution of 2.5±0.9 cm during the last century (Kjeldsen et al., 2015).

The increased mass loss the GrIS has experienced during the last two decades and the growing interest in predicting future mass loss makes it increasingly important to unearth past climate, monitor the present and improve model predictions. These three sides of the same story all play a key part in understanding the state of the current climate and the evolution of climate going forward. Past climate records can, amongst other things, shed light on previous states of the atmosphere and ice extents (e.g., Dansgaard et al., 1993; Lisiecki and Raymo, 2005). Monitoring the present climate reveals both its current state compared to past climate records (e.g., Meredith et al., 2019) as well as constantly improving the collective understanding of the many intricate parts of the climate system (e.g., Karlsson et al., 2021). Improving model predictions is largely connected to both past and present climate as the quality of model outputs is largely dependent on the quality of prior knowledge, the data forcing the model and a physical understating of the process the model hope to recreate.

1.2. Objective of the project and structure

The aim of this PhD project was to develop new approaches for using Global Navigation Satellite System (GNSS) data to study Greenland and contribute knowledge of the ongoing effects of global climate change, both on and off the ice sheet. This objective was met by dividing the project into three studies using three different approaches, two of which build on a newer way of processing GNSS data. The first study aimed to explain the deformation changes observed by Greenland GNSS Network (GNET) stations near large glaciers, by comparing elastic uplift and solid ice discharge. The second study aimed to make an assessment of the ability of CryoSat-2 altimetry to capture both long and short-term changes to the interior of the GrIS, by comparing CryoSat-2 derived Surface Elevation Change (SEC) with three ten-year surface elevation time series from permanent GNSS stations. The third study aim to show that snow thickness on bedrock can be derived from GNET stations using Global Navigation Satellite System Interferometric Reflectometry (GNSS-IR).

Our work on these three studies is presented according to the following structure. An introduction to the different concepts which underlie the studies and GNSS processing methods is given in the remainder of Chapter 1. The three scientific articles on which this thesis is based are summarised in Chapter 2, the location of the GNSS stations used in the different studies can be seen in figure 1.1, while the paper transcriptions are in the Appendix. Chapter 3 presents work in progress that ties into the third study. Chapter 4 discusses different aspects of the three studies and whether the approaches presented in each study can be applied to additional data. Finally, Chapter 5 summarises our findings.

1.3. Observations of Greenland Mass Change

A wide range of satellite sensors, model outputs and observation methods are used to study the GrIS. Some of the more common approaches to study mass changes include satellite gravimetry, satellite and airborne altimetry and the Input-Output Method (IOM). Satellite gravity measurements from the GRACE and GRACE-FO satellites can be converted into mass change (Chen et al., 2006; Sasgen et al., 2020; Velicogna and Wahr, 2006). Airborne and satellite altimetry measure ice surface height and provide SEC used to estimate ice volume changes (Helm et al., 2014; Khan et al., 2014a; Pritchard et al., 2009). The IOM depends on output from Surface Mass Balance (SMB) models to account for surface mass changes (Van den Broeke et al., 2016) and ice discharge through flux gates to account for glacier dynamics (Rignot and Kanagaratnam, 2006).

Each method has a unique combination of strengths and weaknesses, which qualify them for different use cases and account for discrepancies between their results (see fig. 1.2). GRACE/-FO provides solutions at a monthly temporal resolution. However, the solutions have a coarse spatial resolution, which means mass change results from GRACE/-FO are not suitable to study individual glaciers (Barletta et al., 2013). Satellite and airborne altimetry provide a high spatial resolution but limited temporal sampling, which is monthly to annual depending on the mission (Khan et al., 2014b; Schenk et al., 2014). The IOM has the advantage that it identifies the physical processes responsible for the mass changes. Since 2016 the IOM has provided weekly solutions (King et al., 2020) while yearly solutions are available since 1972 (Mouginot et al., 2019). However, while GRACE/-FO provides direct estimates of mass changes, both altimetry and the IOM need several models and/or prior knowledge to derive the ice mass changes, resulting in relatively high uncertainties in ice mass loss estimates. Furthermore, it is apparent from figure 1.2 that different data processing approaches within one method also yield different results,

Figure 1.1: Map of Greenland from QGreenalnd (Moon et al., 2021). The Grey dots scattered along the Greenland coast line indicate positions of GNET stations. The blue dots on the interior of the Greenland ice sheet indicate positions of 3 GLISN GNSS stations. The data from GNET stations KAGA, KUAQ and HEL2 are used in paper I. The data from GLISN stations GLS1 (Detrick and Anderson, 2011a), GLS2 (Detrick and Anderson, 2012) and GLS3 (Detrick and Anderson, 2011b) are used in paper II. The data from GNET stations NORD is used in paper III

which highlights the need for improving prior knowledge and the general understanding of the physical processes both observed and modelled.

1.4. Airborne and Satellite Altimetry

Airborne and satellite altimetry is an efficient technique for mapping the surface elevation of anything from solid earth to ocean at a high spatial resolution. Since the launch of the European Remote Sensing satellite (ERS) in June 1991 (van't Klooster, 2011), satellite radar and laser altimetry have measured ice sheet and glacier surface elevation change, providing continuous estimates of ice volume loss through several satellite missions (ERS1/2, ICESat and ICESat-2, and CryoSat-2), using airborne missions to bridge the gap between ICESat and ICESat-2 (Operation ICEBridge). These altimetry missions, which employ both laser and radar altimeters, have different spatial and temporal resolutions dependent on the satellite return period, the track spacing and the altimeter type.

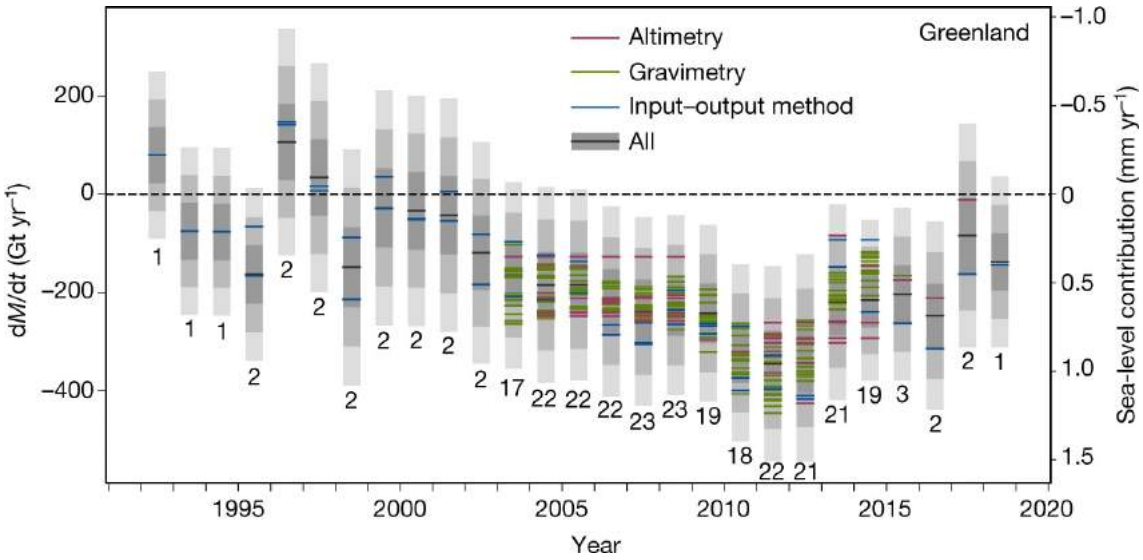

Figure 1.2: Figure from Shepherd et al. (2020) showing rate of mass change (dM/dt, where M is mass and t time) of the GrIS determined from the satellite-altimetry, IOM and gravimetry assessments included in this study. In each case, dM/dt is computed at annual intervals from time series of relative mass change using a 3-yr window. An average of the estimates across each measurement technique is also shown for each year (black line). The estimated 1σ, 2σ and 3σ ranges of the class average are shaded in dark, mid and light grey, respectively; 97% of all estimates fall within the 1σ range, given their estimated individual errors. The equivalent sea level contribution of the mass change is also indicated (right vertical axis), and the number of individual mass-balance estimates collated at each epoch is shown below each bar.

The theory behind laser and radar altimetry is very similar. The biggest difference between the two is that laser altimeters transmit light pulses, whereas radar altimeters transmit microwave pulses. The altimetry technique obtains surface heights by estimating the distance between the altimeter and the surface below it from measurements of the pulse travel time. As Figure 1.3 illustrates there are a couple of differences associated with the different pulses. Firstly, the radar pulse footprints are significantly larger than the laser pulse footprints. Secondly, radar pulses tend to penetrate through dry snow, while laser always bounces back from the first surface it encounters. The disadvantage of the lasers ability to bounce of the first given surface is that laser pulses can not penetrate through clouds.

1.5. Vertical Land Motion

Isostatic adjustments are relatively small 3D movements of the Earth's crust in response to mass changes on the Earth's surface (see figure 1.4). The movements can be up to cm yr^{-1} scale and are therefore large enough to be measured by GNSS stations attached to bedrock. The isostatic adjustments of Greenland bedrock are caused by a combination of viscoelastic and elastic adjustments, which are on very different time scales. The viscoelastic adjustment, often referred to as Glacial Isostatic Adjustments (GIA), is an ongoing rebound from deglaciation following the last glacial maximum $\sim$20,000 years ago (Khan et al., 2008). Because the adjustment happens slowly, the magnitude of it can be considered constant within shorter time scales (Velicogna, 2009). The elastic adjustment is a near instantaneous elastic response to present-day mass changes (Bevis et al., 2012).

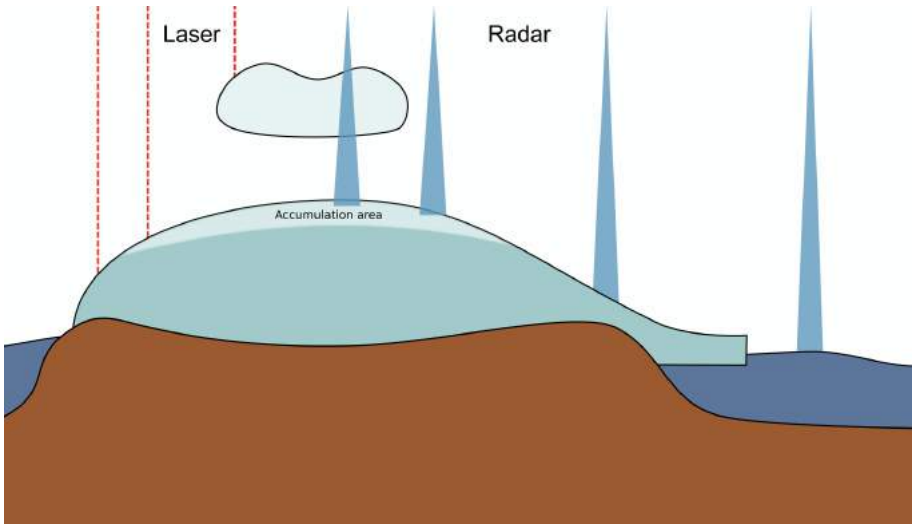

Figure 1.3: illustration provided by Trine S. Dahl-Jensen. The illustration shows an ice sheet on bedrock at an arbitrary point in time, with both laser and radar altimetry pulses reaching the surface of the ice sheet. The laser altimetry pulses bounce of the first surface the pulse hits indifferent of the surface being bare ice, dry snow or a cloud. In contrast, the radar altimetry pulses bounce of some surface types and penetrate through others.

Because elastic adjustments happens near instantaneous there is a response every time mass is added to or subtracted from the GrIS.

The elastic adjustments in Greenland can largely be attributed to two processes that contribute to mass changes of the GrIS in different ways. The first, SMB, is the mass changes caused by weather e.g. snow fall or surface melt. The other, dynamic thinning or thickening are changes in ice thickness that are not driven by components included in SMB. Even though the two processes both contribute to surface elevation change of the GrIS they have different spatial patterns. SMB induced changes often have a relatively large footprint, due to being driven by weather. Whereas, dynamic induced changes are typically largest along the main glacier flowlines and near the glacier terminus (Khan et al., 2020; Khazendar et al., 2019). Because mass changes of the GrIS are by far the largest component of elastic adjustments in Greenland, other factors are rarely discussed, such as adjustments triggered by significant amount of snow fall on bedrock or the drainage of large lakes (e.g., Kjeldsen et al., 2014).

1.6. Global Navigation Satellite System

1.6.1. GNSS positioning

In classic geodesy GNSS stations are used to measure precise 3D positions. A generic GNSS station consists of an antenna, a receiver, a monument, some form of power supply and various cables. When talking about the position of a GNSS station it generally refers to the position of the antenna, because it is the antenna that interacts with the satellites. The position of a GNSS antenna is computed from measurements of the distance between the antenna and all the GNSS satellites the GNSS station is in contact with (see fig. 1.5). The minimal number of distance measurements needed between GNSS satellites and a GNSS antenna to compute the position is four, one for each of the unknowns that needs to be determined (x, y, z, t). Naturally an increase in number of measurements increases the precision (Luo et al., 2021), which is why the number of GNSS satellites in orbit has

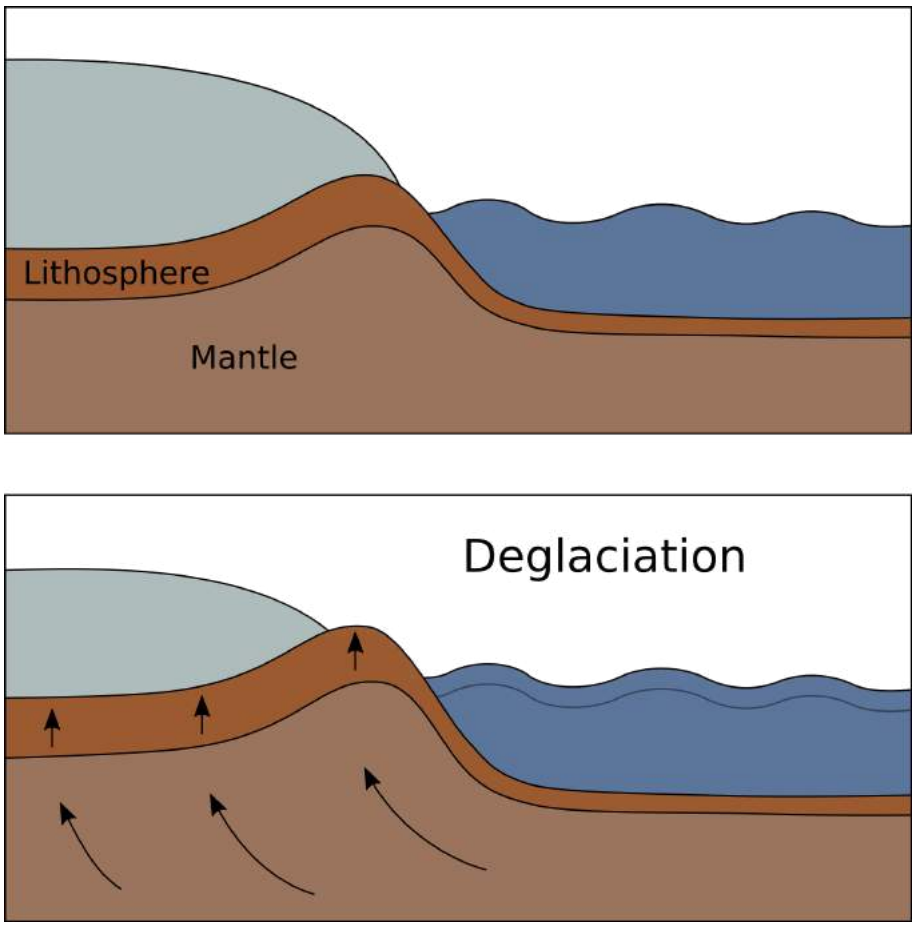

Figure 1.4: Illustration provided by Trine S. Dahl-Jensen. The upper illustration shows an ice sheet on bed rock at an arbitrary point in time. The lower illustration shows isostatic adjustments caused by mass loss from the shrinking ice sheet.

increased significantly the U.S. Department of Defense developed the space-based positioning, navigation, and timing system in the late 1960s and early 1970s (McNeff, 2002). There are currently four GNSS constellations and a two regional navigation satellite systems constellations (IRNSS, QZSS). The original global navigation satellite constellation, the Global Positioning System (GPS), is American and was for many years synonymous with all navigation and positioning. The second GLONASS, is Russian and their first satellite was launched a couple of years after GPS in 1980s (Revnivykh et al., 2017). The third BeiDou, is Chinese and their first satellite was launched in 2000 (Han et al., 2011). The fourth Galileo, is from the European Space Agency (ESA) and is the newest with the first launch in 2011 (Benedicto et al., 2000).

Simplified, the distance is measured by timing the signal the satellite is transmitting. Most of the software for computing the daily average 3D position of a GNSS antenna are very robust, as the methods have been developed, used and improved for more than 40 years. The precision of the 3D position is very much dependent on the ability to simultaneously observe signals from all GNSS satellites visible to the GNSS station and corrections for well known error sources (Karaim et al., 2018). The typical error sources can all be modelled or estimated and include satellite orbits and clocks, precise models of the Earth e.g. of its rotation, atmospheric delays and multipath frequencies, which are caused by interference from signal reflections (see fig. 1.5 and 1.6). As the only one of the know

error sources, multipath frequencies are ignored when computing position. The reason multipath frequencies are not corrected for is threefold. Firstly, they are difficult to model, as they are site specific. Secondly, many geoscience problems can be solved without correction, as they can be resolved by averring over longer time periods. Thirdly, choke ring antennas have reduced but not eliminated multipath frequencies, which is why the development of choke rings is generally perceived as an improvement.

1.6.2. GNSS Interferometric Reflectometry

In contrast to GNSS positioning, the GNSS-IR method is built around the multipath frequencies whilst ignoring the rest of the signal.

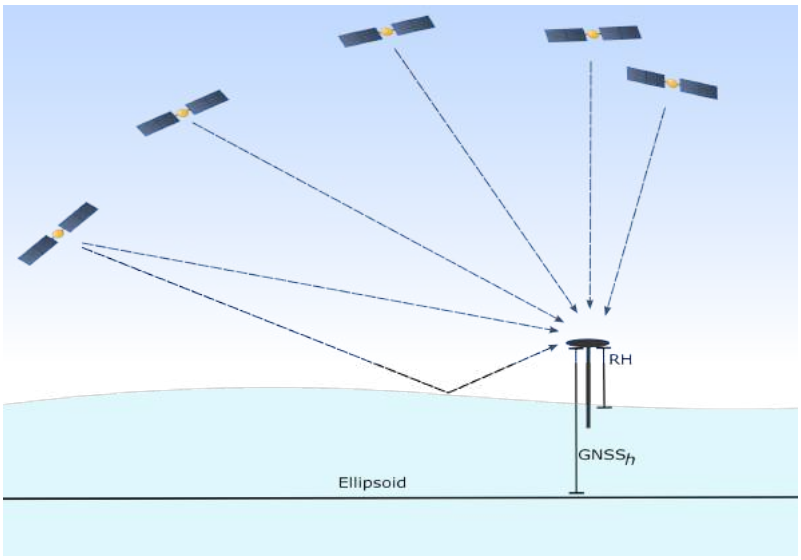

Figure 1.5: Simple illustration of a GNSS station on an ice sheet receiving signals from multiple GNSS satellites simultaneously. The Ellipsoid line indicate the reference for the computed 3D position. GNSS$_\mathbf{h}$ illustrate the z component of the computed 3D position. RH illustrate the computed RH from SNR data. One of the satellites are low enough in the horizon that both the direct signal and the signal reflection reach the antenna.

GNSS-IR is a method for processing GNSS data that, among other things, makes it possible to find the vertical distance between a GNSS antenna and the surrounding surface, often referred to as the Reflector Height (RH) (Larson et al., 2015, 2020; Roesler and Larson, 2018). GNSS-IR has been established within this century, with some of the first publications using the method published in the early 2000s (e.g., Anderson, 2000). Even though GNSS-IR is fairly new, the mathematical formula for estimating multipath frequencies has been known for a long time. In 1988 Georgiadou and Kleusberg (1988) showed the path delay δ, phase shift Ψ and multipath frequency f_Ψ can be expressed as equations 1.1, 1.2 and 1.3, respectively.

$$\delta = 2\mathrm{RH} \cdot \sin(\alpha) \tag{1.1}$$

$$\Psi = 2\pi \cdot \frac{2 \cdot \mathrm{RH}}{\lambda} \sin(\alpha) \cdot \Psi_0 \tag{1.2}$$

$$f_\Psi = \frac{2 \cdot \mathrm{RH}}{\lambda} \cos(\alpha) \cdot \frac{\mathrm{d}\alpha}{\mathrm{d}t} \tag{1.3}$$

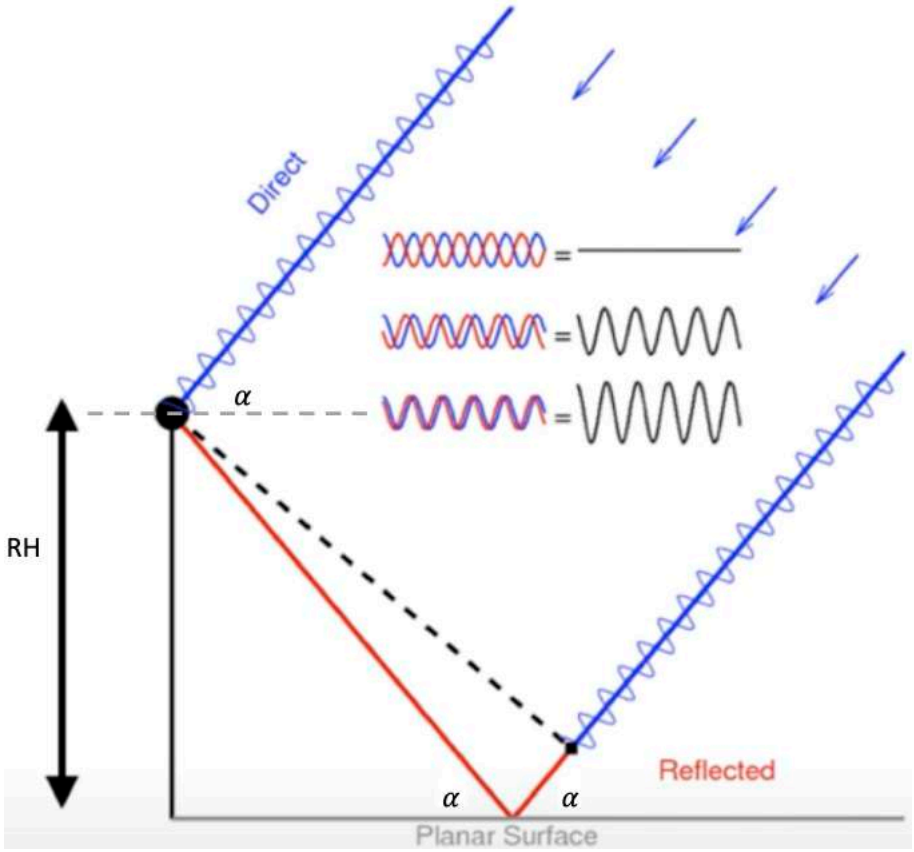

Figure 1.6: Illustration of GNSS-IR from Kristine Larson (gnssrefl GitHub, Larson (2021)). The blue lines illustrate the direct signal. The red line illustrate the signal reflection. Three interference examples are shown between the direct signal illustrations. The black dot illustrate the GNSS antenna and α illustrate the elevation angle.

Where the phase delay Ψ_0 is a possible fixed offset, λ is the signal wavelength and the elevation angle (α) is the angle of the signal at the GNSS antenna with respect to the horizon (see fig. 1.6). Axelrad et al. (2005) showed the expression for multipath frequencies can be simplified by changing the variable from α to $\sin(\alpha)$ (fig. 1.7), thereby eliminating the derivative term, leaving an expression for the multipath frequency that relate to RH and λ in a simple way (eq. 1.4).

$$f_\Psi = \frac{2 \cdot \mathrm{RH}}{\lambda} \tag{1.4}$$

Multipath frequencies are observed in three different ways. The first way is in pseudorange data, which is mainly used by the navigation community, it has large errors and is noisy (e.g., Chuang et al., 2013). The second way is in the carrier phase data, which is used by geodesists, surveyors and geophysicists. Carrier phase data was earlier used to study the multipath frequency problem (e.g., Cardellach et al., 2004), but it was complicated because a combination of multiple satellites was needed and because it contained other error sources. The third way is by carrier to noise ratio (SNR) data, also referred to as signal strength or signal to noise ratio. SNR data is not used for anything besides multipath frequency studies as it does not contain information related to position, which is what GNSS was developed for (McNeff, 2002). Figure 1.7 clearly illustrates how simple

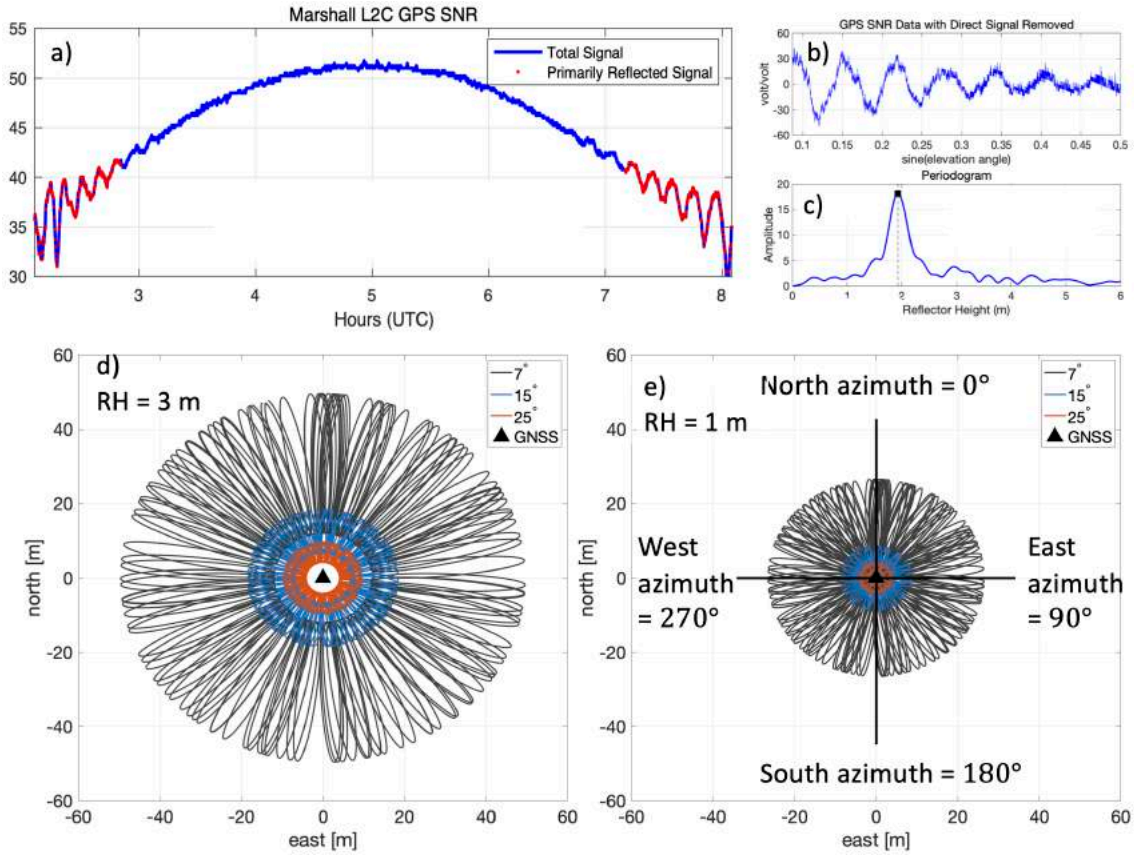

Figure 1.7: a) SNR data plotted as a function of time from Kristine Larson (gnssrefl GitHub, Larson (2021)). b) SNR data, with the direct signal removed, plotted as a function of $\sin(\alpha)$ from Kristine Larson (gnssrefl GitHub, Larson (2021)). c) Illustration of periodogram used to estimate the RH by identifying the peak from Kristine Larson (gnssrefl GitHub, Larson (2021)). d) Illustration of GNSS-IR footprint size at different elevation angles when the RH = 3 m. e) Illustration of GNSS-IR footprint size at different elevation angles when the RH = 1 m and the directions different azimuth angles correspond to.

SNR data is. Plotted over time, is has an overall polynomial shap where the relatively smooth part in the middle of the signal is the time period where the elevation angle is large enough to eliminate multipath frequencies. The approximate sinusoids in either end of the signal are caused by interference from signal reflections. Besides the simplicity, another benefit to SNR data is that it makes it possible to distinguish the satellites from one another, thus making it possible to compute the RH from one satellite at a time.

The GNSS-IR software used in this thesis (gnssrefl, Larson (2021)) finds the RH from SNR data based on the theoretical knowledge of what a multipath frequency should be (eq. 1.3, Georgiadou and Kleusberg (1988)) and the change in variables concept introduced by Axelrad et al. (2005). Using the Axelrad et al. (2005) concept speeds up the estimation of RH as the expression for modeling the SNR data is simplified to eq. 1.5 (Roesler and Larson, 2018).

$$\text{SNR} = A(\alpha) \cdot \sin\left(2\pi \cdot \frac{2\text{RH}}{\lambda} \cdot \sin(\alpha) + \Psi_0\right) \tag{1.5}$$

Where the signal wavelength λ is known, $A(\alpha)$ represent the amplitude of the SNR data and Ψ_0 is the phase delay. The amplitude is not constant, as it monotonically decreases as the satellite rises, and is impacted by reflection material and surface roughness (Nievinski and Larson, 2014). The RH is extracted from the SNR data by using the Lomb Scargle periodogram to extract the SNR spectral content (Lomb, 1976; Vetterling et al., 1992) and scaling the sampling variable (sin(α)) by a wavelength factor (Roesler and Larson, 2018). Equation 1.4 clearly shows the limitation of the method, as it is impossible to accurately distinguish RH from the direct signal when RH $\approx 2\lambda$, meaning RH $<$ 0.5m can not be extracted.

The area of the surface surrounding a GNSS station included in the computation is partly site specific and partly controlled by the gnssrefl user. Figure 1.7 shows the observation radius for three different elevation angles with two different RH. The user is able to control the elevation angle range, thereby controlling the observation radius to some degree. But the limit of the observation radius comes from the RH as an antenna installed on a 3 m monument has the potential to cover a much larger area than an antenna installed on a 1 m monument. The available azimuth angles can also be both site specific and controlled by the gnssrefl user. At some positions in the Northern Hemisphere are there no observations in the northern azimuth angles because no satellites rise or descent in that direction. Likewise, are there no observations in the southern azimuth angles for some positions in the Southern Hemisphere. Furthermore, structures such as buildings, mountains and forests can block satellite signals, which means the satellite signal only reaches the antenna when the elevation angle is too high for multipath frequencies. But the user can also limit the azimuth angle interval the RH is computed for, which can make sense when studying something in a specific direction or wanting to exclude directions where man-made structures introduce reflections.

As mentioned above can GNSS-IR be used to derive other parameters than the RH. When RH is fixed, Ψ_o can be used to derive surface soil moisture (Larson et al., 2008, 2009; Chew et al., 2016) and $A(\alpha)$ can be used to measure vegetation water content (Wan et al., 2015).

CHAPTER 2

Summary of Papers

2.1. Paper I

K. Hansen, M. Truffer, A. Aschwanden, K. Mankoff, M. Bevis, A. Humbert, M. R. van den Broeke, B. Noël, A. Bjørk, W. Colgan, K. H. Kjær, S. Adhikari, V. Barletta, and S. A. Khan. Estimating ice discharge at greenland's three largest outlet glaciers using local bedrock uplift. *Geophysical Research Letters*, 48(14):e2021GL094252, 2021 (Appendix A)

A wide range of sensors and methods have been used to examine changes of the GrIS (e.g., Sasgen et al. (2020); Helm et al. (2014); Rignot and Kanagaratnam (2006); Van den Broeke et al. (2016)), each with a unique combination of strengths and weaknesses. A common denominator for many of these studies is the fact that they in one way or another build on satellite data, which means they are all limited in their temporal resolution.

The aim of this paper was to estimate local dynamic ice loss from direct observations of uplift using GNSS stations on bedrock, thereby expanding the use of GNSS data to study mass changes of the GrIS. GNSS data, in contrast to satellite data, has a daily temporal resolution, making it possible to reveal short-term mass fluctuations and improve our understanding of glacier dynamics at a daily timescale (Adhikari et al., 2017; Khan et al., 2010).

We studied Greenland's three largest outlet glaciers; Jakobshavn Isbræ, Kangerlussuaq glacier and Helheim glacier. We focused on the GNSS stations closest to the glaciers termini because the magnitude of the Earth's elastic response to mass changes decreases as the distance to the mass loss center increases (Adhikari et al., 2017; Wahr et al., 2013). To isolate dynamic induced deformation we corrected each GNSS uplift time series for elastic deformation caused by SMB and Viscoelastic deformation caused by GIA. The elastic uplift due to SMB was estimated by a three step process. First, we integrated the RACMO2.3p2 SMB product over the drainage basin of each glacier (van Wessem et al., 2022). Second, we removed the mean 1961-1990 SMB to obtain SMB mass anomalies. Third, we modelled the elastic uplift due to SMB mass anomalies with the green's function for elastic Earth model iasp91 derived by Wang et al. (2012). In order to ignore Viscoelastic uplift, which can be considered constant over our time period (Velicogna, 2009), we detrended each uplift time series by fitting and removing the linear and yearly term.

We then compared our dynamic induces uplift time series with solid ice discharge, measured using the flux gate method (Mankoff et al., 2019, 2020). For the uplift and discharge time series to be comparable we made a cumulative discharge time series, removed the associated basin-wide 1961-1990 mean SMB, estimated using RACMO2.3p2, and detrended the time series by fitting and removing the linear and yearly term. We found a time lag between the two time series, with the dynamic changes consistently preceding

changes in ice discharge. Because the flux gate method largely depends on glacier velocity, we concluded dynamic changes to ice thickness precede glacier velocity changes. To find the time lag between dynamic thinning/thickening and velocity changes we developed a simple linear relation between the two for each glacier, estimating the parameters using least square adjustment. Our results show a large variation in time lag between the glaciers, ranging from 10.4 months at Jakobshavn Isbræ to 11 days at Helheim glacier.

In order to estimate dynamic ice loss from observed GNSS uplift we used the detrended uplift time series with the corresponding parameters to make a discharge reconstruction for each glacier. Because the relation was estimated after the time series had been detrended the reconstructed dynamic ice loss from GNSS is independent of any trends that may effect GNSS data. Once the relation is established it can be used to estimate dynamic ice loss within the time lag period. Estimating dynamic ice loss using the GNSS data covered by the time lag period does in principle allow us to predict near future dynamic ice loss.

2.2. Paper II

K. Hansen, W. Colgan, K. M. Larson, M. J. Willis, V. Helm, and S. A. Khan. Assessment of esa cryosat-2 radar altimetry data using gnss data at three sites on the greenland ice sheet, a. submitted to Journal of Geophysical Research: Earth Surface (Appendix B)

Satellite laser and radar altimetry have provided continuous estimates of ice volume loss from the GrIS through several satellite missions since the launch of the ERS satellite in June 1991. As radar tend to penetrate through the snow surface, validation of these products is extremely important. Several studies have evaluated satellite altimetry data using external data in several different ways (e.g., McMillan et al. (2018); Brunt et al. (2017); Stokholm et al. (2021); Nilsson et al. (2015)).

The aim of this paper was to use three long-term GNSS time series to assess SEC observed by CryoSat-2 radar altimetry data. The novelty of the study stems partly from the GNSS derived long and high resolution surface elevation time series and partly from the way we derived surface elevation from the GNSS data. The three GNSS stations used in this study were installed on the GrIS in 2011 by the Greenland Ice Sheet Monitoring Network (GLISN) project. The GNSS stations GLS1, GLS2 and GLS3 (GLS1-3) are located at DYE-2, Ice South Station and NEEM field camp respectively. At the time of writing this thesis all three stations can be considered to have been buried by snow, as it is no longer possible to download the newest data.

We obtain the ice surface elevation from the GNSS data by processing it with two different methods and combining the results. The first processing method, which can be considered the normal/traditional, estimates the GNSS antenna 3D position (see section 1.6.1). The second processing method estimates the RH using GNSS-IR (see section 1.6.2). By subtracting the RH from the z component of the 3D position, we get the closest possible estimate of the true surface elevation over the reference ellipsoid.

We estimate a CryoSat-2 surface elevation time series at a point either at the GNSS station or close to the GNSS station by projecting all available CryoSat-2 data points within a 750 m radius to that point. For GLS1 and GLS3 these points are located at a position where the GNSS stations have been during the GNSS time series. For GLS2 the point is located within 750 m of the GNSS station, but at a location with higher CryoSat-2 data density. All CryoSat-2 data points are corrected for surface topography in order to account for the variation accruing across the approximately 1.7 km^2 area where the CryoSat-2 data is scattered. Furthermore we correct the GNSS time series in the same way, because the GNSS stations move during the time period and because the CryoSat-2 time series near GLS2 is located west of the station.

We found the strength of assessing satellite radar altimetry against permanent GNSS stations was attributed to our ability to estimate the true surface elevation as a continuous daily time series that clearly captured both short and long-term changes. From these time series we could validate that CryoSat-2 indeed captures SEC. The performance was best at the northernmost GNSS site (GLS3) with a maximum difference of 12 cm. At the other GNSS sites the residual ranges were higher because of poorer data availability and local surface variations. The number of CryoSat-2 data points are roughly doubled from GLS1 and GLS2 to GLS3. Furthermore, GLS3 is located in a very flat area of the ice sheet and only moved 55 m during 2011-2020. In contrast, GLS1 moved 292 m in the same period.

From our estimate of the true surface elevation we calculated the yearly Surface Elevation Change $(\partial h/\partial t)$ for every available date pair at all three GNSS stations. $\partial h/\partial t$ showed

large variation throughout the year, with a general underestimation in November and December and a general over estimation in August at all three stations. Furthermore, $\partial h/\partial t$ showed that an April to April ice sheet wide ∂h/∂t campaign would represent the average ∂h/∂t from GNSS the best.

2.3. Paper III

K. Hansen, T. S. Dahl-Jensen, and L. Stenseng. Terrain corrected snow thickness from gnss-ir at station nord, b. draft intended for submission to the GEUS bulletin (Appendix C)

Due to the extensive length of the Greenland coastline many areas go unvisited for most of the year. Knowledge of snow build-up and melt in these areas is limited and often dependent on model output. However, in areas with significant snow build-up during winter, data from GNSS stations can be used to derive terrain corrected snow thickness when processed using GNSS-IR.

In this study we use GNSS-IR to derive the RH between 2018 and 2022 from the GNET station at Station Nord (NORD), where a significant difference in RH throughout the year made it possible to identify time periods with a bare soil surface. We used the RH from the bare surface periods to estimate a 360° summer surface topography profile around the station, which we then used as a reference for estimating snow thickness throughout winter.

When deriving the snow thickness time series it became apparent the snow primarily builds up through winter and maintains a high snow thickness until onset of melt. Comparing the derived summer surface with the snow surface, from a day with a high snow thickness, we see how the snow has built up to an approximately flat surface despite the topography beneath it, which shows the snow thickness can vary a lot in a relatively small area. This is further confirmed by the approximately 80 cm difference between the minimum and maximum snow thickness found on the 29th of May 2020.

Because of a distinct snow thickness pattern, where snow build up until a rapid decrease in snow thickness starts, the onset of melt is easily identified. From the time series we found the onset of melt to be on the 16th of June in 2020 and on the 15th of June in 2021. To validate our findings we compared the 2020 snow thickness time series with a temperature time series from a near by weather station and found our onset of melt date corresponded to the first longer time period where the daily average temperature was above 0°C.

CHAPTER 3

Work in progress

3.1. Introduction

In Paper III we presented a method for deriving terrain corrected snow thickness from GNSS data using GNSS-IR. As an extension of this study we are working on deriving snow thickness time series from all GNET stations. The aim of this extension is initially to investigate snow build-up variation along the Greenland coast line, with an emphasis on secluded areas where information of this is sparse. Furthermore, we intend for the method and results to become a foundation on which future monitoring of Greenland snow thickness in secluded areas can be build.

3.2. Preliminary Results

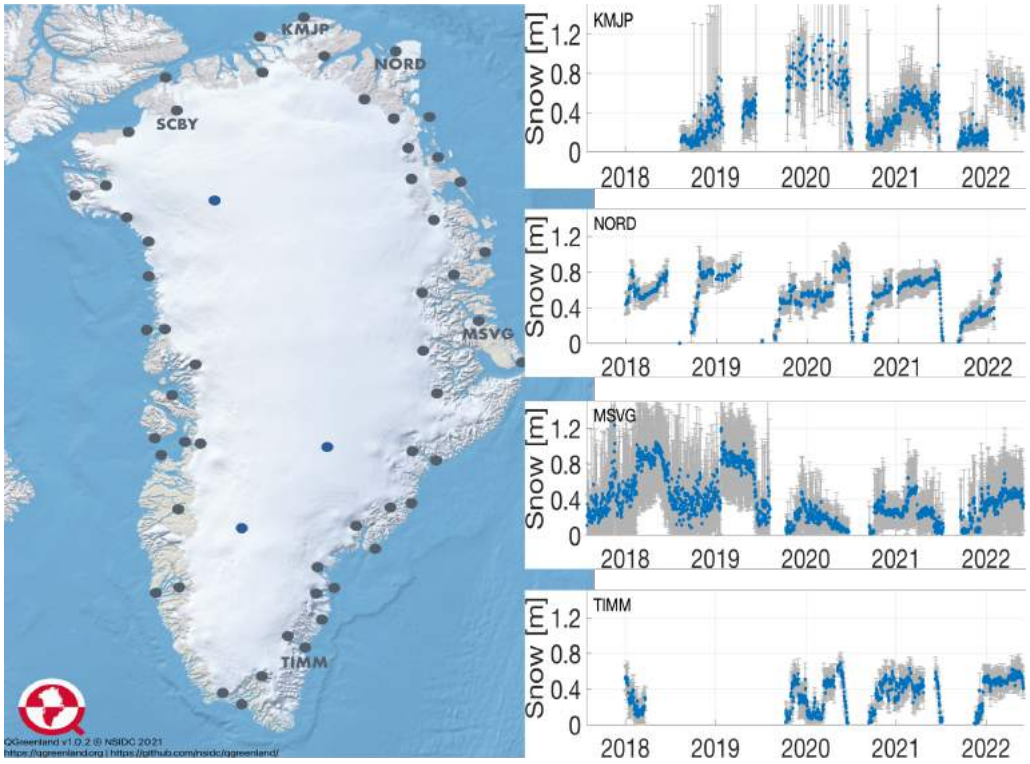

Figure 3.1: Map of Greenland from QGreenalnd (Moon et al., 2021). The Grey dots scattered along the Greenland coast line indicate positions of GNET stations and the blue dots in the interior of the GrIS indicate the position of the three GLISN stations. The stations from which data have been processed are marked by their name. The average terrain corrected snow thickness time series derived for KMJP, NORD, MSVG and TIMM are shown next to the map.

We have processed data from five of 59 GNET stations using GNSS-IR and used the method presented in Paper III to derive terrain corrected snow thickness time series from four of them (see fig. 3.1). The yearly maximum average snow thickness shows large yearly variation at MSVG and KMJP and small yearly variation at NORD and SCBY (table 3.2). Whether the variation is large or small at TIMM can not be determined, as the RH time series is broken during winter of 2019/2020 and 2020/2021 (see fig. 3.2).

Winter maximum average snow thickness						
GNET station	Latitude	Longitude	18/19 [m]	19/20 [m]	20/21 [m]	21/22 [m]
NORD	81.60014	-16.65545	∼0.91	∼0.94	∼0.83	NaN
TIMM	62.53554	-42.28615	NaN	>0.69	>0.69	∼0.60
MSVG	72.24082	-23.91286	∼1.05	∼0.48	∼0.55	∼0.50
KMJP	83.64323	-33.37707	∼0.76	∼1.19	∼0.67	NaN
SCBY	80.26013	-59.59361	∼0	∼0	∼0	NaN

3.3. Discussion

Our preliminary results are too small a sample size to comments on the general trends of the years our time series span.

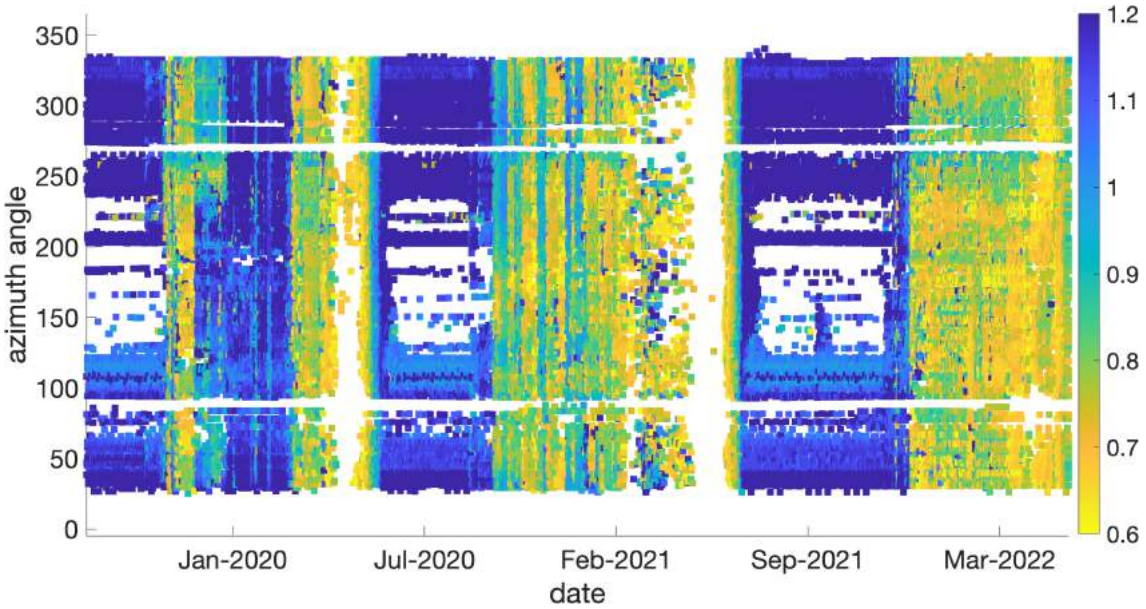

Figure 3.2: TIMM RH time series of every available azimuth angle.

The average snow thickness times series seen in figure 3.1 shows both NORD and TIMM generally have the distinct snow build-up pattern described in Paper III. However, an exception to this can be seen during the winter of 2019/2020 at TIMM where the snow thickness decrease significantly in two stages (fig. 3.2 and 3.1). At this time we have not investigated the cause of this decrease, but speculate it is caused by strong winds moving the snow elsewhere. We do not find it likely the decrease is caused by melt because of the decrease pattern, which is visibly different from the melt season decrease pattern of the periods both seen at NORD and TIMM (fig. 3.1). If results from additional GNET stations in proximity to TIMM show decrease in the same time period it could be both

interesting and necessary to compare with weather station data in the hopes of finding an explanation.

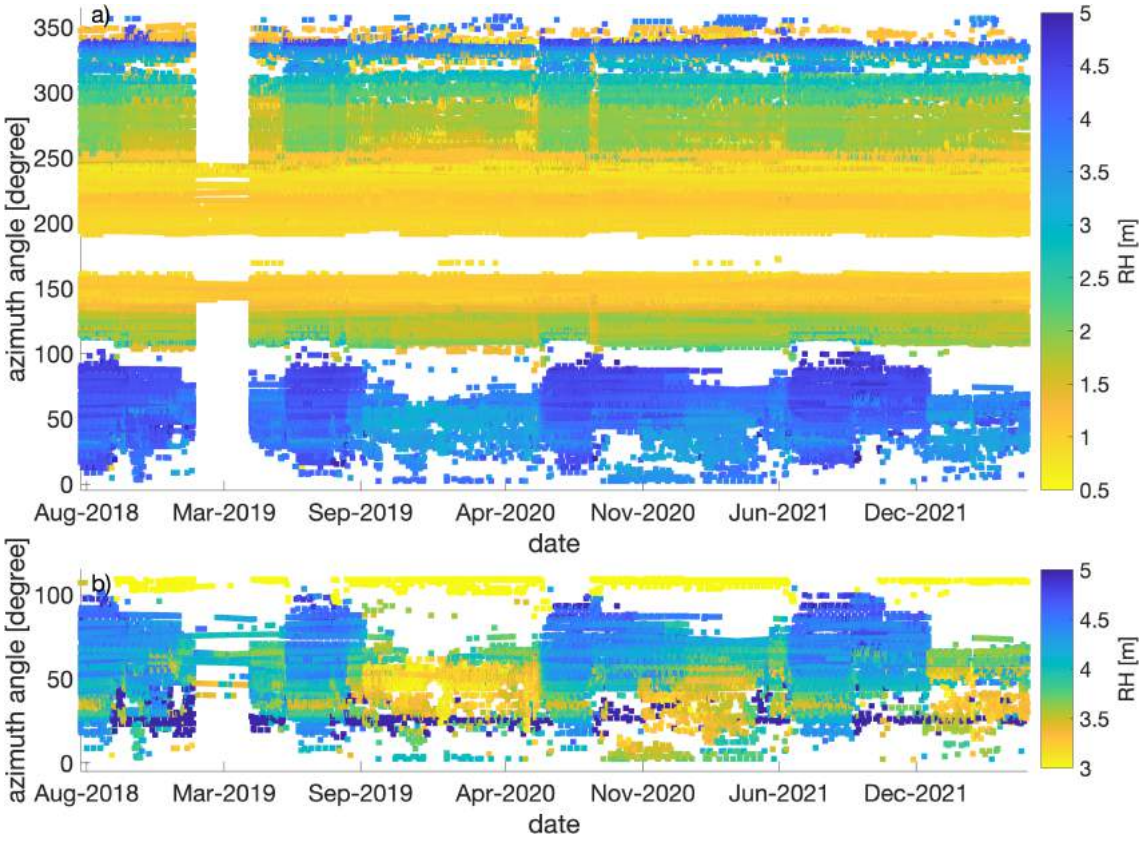

Figure 3.3: a) KMJP RH time series of every available azimuth angle. b) KMJP RH time series in azimuth degree interval [0 : 110].

As mentioned above is the pattern of snow thickness decrease during melt season very distinct at NORD and TIMM, as a relatively steep decrease occur from a high snow thickness to the summer surface (see fig. 3.1). Therefore, the snow thickness time series can be used to estimate the date for onset of melt. If a large enough sample of GNET stations show this behaviour the information could be used to determine when melt approximately starts in different areas of Greenland and over time be used to investigate whether yearly variations are local or extend to all of Greenland.

3.3.1. SCBY

Of the five processed GNET stations SCBY does not have detectable snow build-up during the GNSS-IR derived RH time series (see fig. 3.4). The lag of snow build-up is likely caused by either low precipitation rates or strong winds continually blowing snow of the bedrock before is can build to a visible change in RH. Due to examination of the area surrounding SCBY, using optical satellite imagery, we do not believe the constant RH is caused by a lag of precipitation altogether, as snow is some times visible in the area. Whether we are observing low precipitation rates or strong winds is difficult to quantify. We could compare to model outputs or the RH results from the GNET station at the other end of Petermann fjord (KMOR) but a better solution would be to install a time lapse camera for future validation.

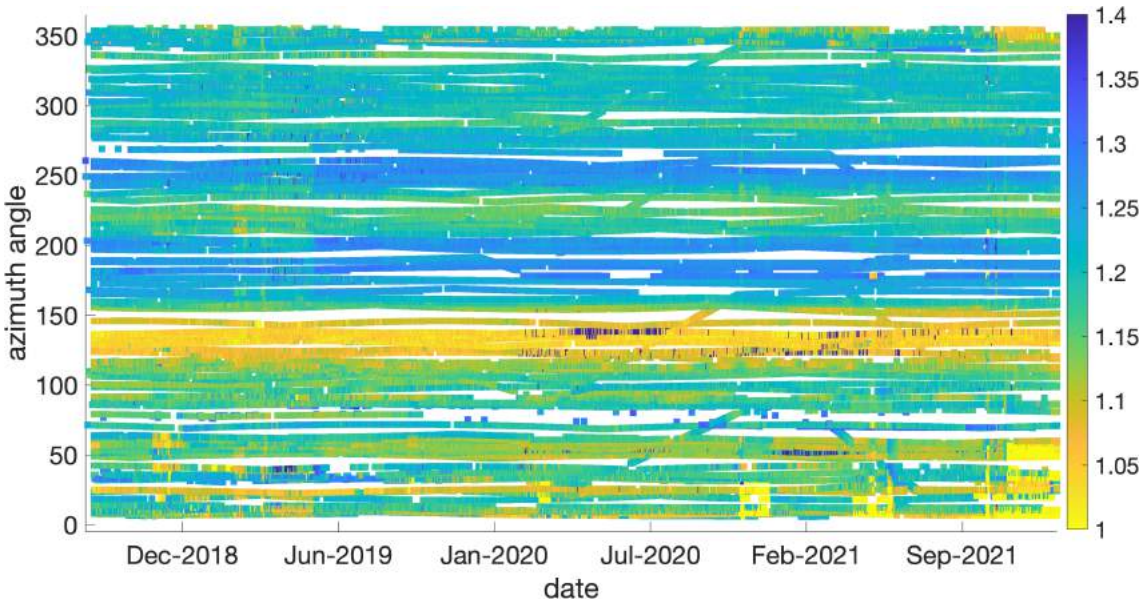

Figure 3.4: SCBY RH time series of every available azimuth angle.

CHAPTER 4

Discussion

As mentioned in the introduction, the overall aim of this PhD project was to use GNSS data to study different aspects of Greenland and the GrIS using new approaches. In order to cover several approaches the project was divided into three individual studies, each resulting in one of the appended papers. Although the discussion of each study can be found in the respective papers (Appendix A,B and C), there are elements of the studies discussed further in this section. In addition it is discussed whether the different approaches can be extended to other glaciers, data products or areas by processing additional data in the same way.

4.1. Estimating discharge of Greenlandic glaciers using local bedrock uplift

When developing the method used in the first study (Hansen et al., 2021), we focus on the three largest outlet glaciers in Greenland as they jointly account for 12% of drainage from the GrIS (Khan et al., 2020). We concluded the paper by suggesting the method should be used for other glaciers, as three glaciers are too small a sampling size to determine whether the tendencies suggested by the results are reproducible for other glaciers. However, we did not look into whether there are other glaciers along the Greenland coastline where the method could be applied.

There are three overall conditions, which need to be fulfilled before it makes sense to apply the method to a specific glacier. The first condition is that a GNET station should be located in proximity to the glacier, preferably right next to the grounding line. The second condition is that a flux gate from Mankoff et al. (2019, 2020) should lie across at the glacier. On the one hand, because the flux gates are automatically generated for glaciers with a velocity of at least 100 m/yr, insuring discharge happens at a noticeable magnitude. On the other hand, because it insures discharge data is freely available. The third condition is that the GNET station is not placed between two glaciers, as it is impossible to distinguish their contribution to elastic uplift from one another. There are 13 glaciers that fulfill the three conditions (see fig. 4.1), when excluding the three glaciers studied in Paper I.

Although the method ideally should be applied to all 13 glaciers, the likelihood for success is reduced for some of them. Making it possible to make a prioritised choice if only interested in studying some of the glaciers. Examining the individual glacier using satellite imagery and ice velocity maps it becomes clear 6 of the glaciers are less likely to succeed, for three different reasons (fig. 4.2a-h). Three of the glaciers (Døcker Smith, Fimbul and Upernavik fig. 4.2b,f) are part of a glacier system with several drainage basins, which might pose a problem if the drainage basins have different dynamic properties. As different dynamic properties could result in a difference in time lag between the drainage basins, which would be impossible to adjust for. The velocity of Waltershausen glacier is

Figure 4.1: Map of Greenland from QGreenalnd (Moon et al., 2021). The grey dots indicate positions of GNET stations, which might be suitable for the method presented in Paper I. The name next to the GNET station markers, are the names of the glaciers.

significantly slower than the rest of the glaciers, which might result in the discharge signal being too small for the method to be successful, as ice discharge is largely dependent on glacier velocity (fig. 4.2c). The last two glacier, with a reduced likelihood for success, are C.H. Ostenfeld and Humboldt (fig. 4.2d), where the GNSS stations are located $\sim$36 km and $\sim$70 km from the center of the flux gate, respectively. In Paper I we speculated a distance of $\sim$30 km would be the cut of point for success, which the distance at C.H. Ostenfeld slightly exceed, whereas the distance at Humboldt is more than double that distance. The large distances reduce the enticement to try the method at these glaciers. However, trying the method on these glaciers would be an easy way to either increase confidence in the suggested $\sim$30 km distance maximum or prove the suggested distance was set too conservatively.

Having recognised the smaller velocity of Waltershausen could turn out to be a problem, it is important to acknowledge that we did not look in to whether the method has lower boundaries for the magnitude of discharge and/or uplift. Having used the three largest Greenland outlet glaciers in the study we simply had no results to investigate. However, applying the method to the 13 glaciers suggested such investigations would be possible. Looking at the glacier examples in figure 4.1 it is clear that the magnitude of discharge is small compared to the discharge range of 30 and 50 Gt yr^{-1} seen at Jakobshavn Isbræ. Furthermore, we see a lower discharge at Humboldt (fig. 4.2p) than at 79Fjord (fig. 4.2m) even though the uplift measured by the GNSS stations are approximately the same (fig.

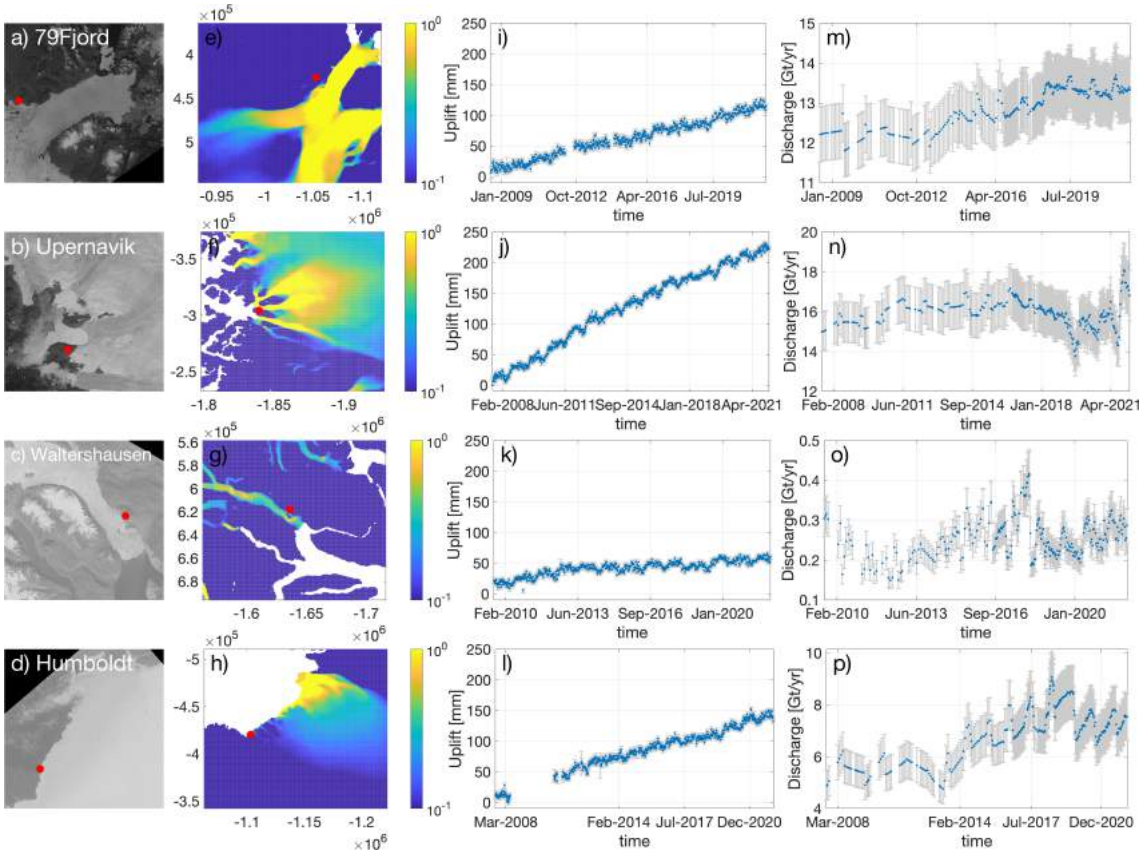

Figure 4.2: a) 79Fjord (Survey and Center, 2022) and the GNET station BLAS (red dot). b) Upernavik glacier (Survey and Center, 2022) and the GNET station SRMP (red dot). c) Waltershausen glacier (Survey and Center, 2022) and the GNET station WTHG (red dot). d) Humboldt glacier (Survey and Center, 2022) the GNET station KAGZ (red dot). The position of the GNET stations and the drainage basin velocity i meter per day at (Solgaard and Kusk, 2021) e) 79Fjord f) Upernavik g) Waltershausen and h) Humboldt. Time series of daily uplift solution at i) 79Fjord, j) Upernavik k) Waltershausen and l) Humboldt. Time series of solid ice discharge from m) 79Fjord o) Waltershausen and p) Humboldt. n) Time series of the combined solid ice discharge from the five Upernavik drainage basins with an ice velocity larger than 100 m/yr.

4.2l,i). Comparing the different uplift time series, their corresponding discharge and the changes in ratio between them, it is clear the data needs to be processed further for us to be able to make a qualified guess on whether applying the method to the glaciers shown here will be successful.

4.2. The difference in time lag between bedrock uplift and solid ice discharge

The time lag between bedrock uplift and an increase in ice discharge is what enabled us to predict near future discharge in Paper I. The time lag occurs when glacier thinning comes before a speedup. This happens because the change in ice thickness immediately results in bedrock motion due to the elastic response of the earth, whereas the forward motion of the ice takes longer to adjust to the changes, as ice is a viscoelastic material. Therefore the viscous response determines the length of the time lag, which can vary from days to

many months depending on the ice viscosity (Christmann et al., 2019; Rankl et al., 2017). This is clearly demonstrated in Paper I where the shortest time lag is 11 days and the longest 10.4 months. Due to the big variation in time lag, we can not refute some of the 13 glaciers suggested to increase the sample size might not have one or have one too short to measure, making it impossible to predict near future discharge at such sites.

Although uninteresting when trying to predict near future discharge, potential glaciers with a short to non-existing time lag still provide unique inside to variations in ice viscosity across the Greenland glaciers. Theoretically time lag information could be used to determine where one can expect mass loss estimates from the IOM and satellite altimetry to be equal on a short timescale and where the two mass loss estimates should be compared with caution. Furthermore, the information could in time be used when modeling glacier flow. As it would enable a modeleur to adjust the velocity response to thinning to align with the time lag found at individual glaciers.

The results from Paper I suggested the time lag increases linearly with the trend of the cumulative dynamic ice discharge. However it is also made clear further investigation using additional glaciers is needed before drawing any conclusions. Should further investigation confirm the relationship, the trend could be an efficient way to screen glaciers for likelihood of a long time lag, before readying the rest of the data needed, which would save time spent on glaciers where the method is unsuccessful. For a potential screening to be as effective as possible, it would be important to use the same SMB model when calculating the 1961-1990 mean SMB for each glacier, as different SMB models could give different results (Fettweis et al., 2020).

4.3. Assessment of ICESat-2 altimetry using GNSS-IR

After completing the data analysis for the second study (Hansen et al., a), it would seem natural to extend the study to include altimetry data from ICESat-2. However, there are several reasons this was not carried out. Firstly, the time overlap between the two time series is relatively short as ICESat-2 was launched in September 2018 and the RH became too small to resolve at the GLISN stations in 2020-2021. Secondly, the satellite flight tracks are not close enough to the station for surface correcting approach 1 from Paper II to work. Thirdly, ICESat-2 flight tracks does not pass directly above the GLISN stations. Fourth, ice sheet wide SEC products from ICESat-2 (e.g., Hansen et al. (c)) have a much larger footprint than a GNSS station and often provide only one elevation change estimate per year.

The time overlap alone would not be a problem if the other parameters were ideal, as ICESat-2 has a 91 day return cycle (Smith et al., 2019), which would result in approximately the same number of days with satellite altimetry measurements per station as seen in Paper II, just compressed together in a two year time span. A reduction in time overlap would reduce the confidence in the satellites ability to determine long-term elevation changes. However, it would be a better benchmark, when evaluating the satellites ability to capture extreme short-term elevation changes, which could prove just as important if the recent record high ice-sheet-wide losses in 2012 and 2019 are a preview of the what can be expected in the future (Nghiem et al., 2012; Sasgen et al., 2020).

In Paper II we applied a 750 m radius to select CryoSat-2 data and correct for surface topography. If applying the same radius for data selection there are only data available at GLS2 and GLS3. Furthermore is the data only available on one side of the station (see fig. 4.3), which would render the simple surface topography correction approach from Paper II inadequate. This issue could be solved by either using the existing DEM

or increasing the radius used for data selection to include ICESat-2 flight tracks on both sides of the GNSS station. In either case it is likely the residual range would increase as Paper II showed the simple correction approach was better than a DEM and a larger radius is likely to decrease precision.

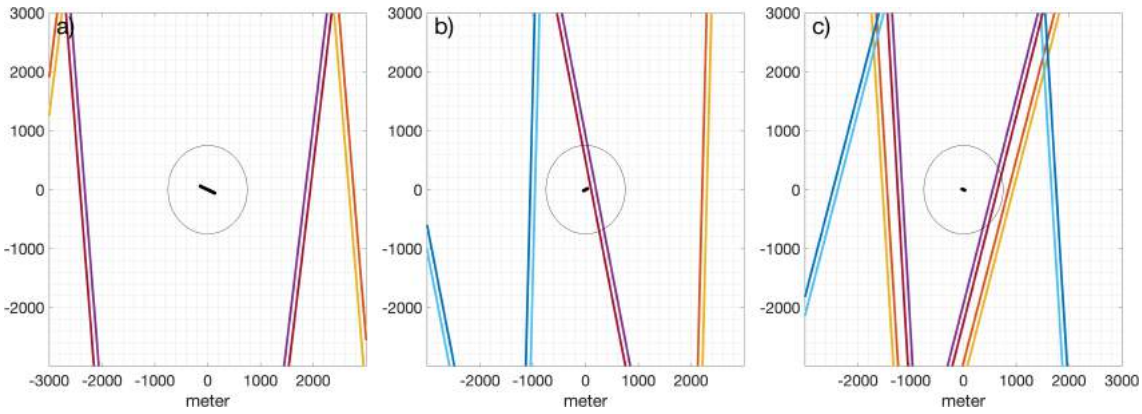

Figure 4.3: ICESat-2 flight tracks within 3000 m square of the GLISN stations GLS1, GLS2 and GLS3 (a, b and c, respectively). Laser 1 and 2 measure the orange and yellow tracks. Laser 3 and 4 measure the dark and light blue tracks. Laser 5 and 6 measure the purple and maroon tracks. The black dots show the movement of the GNSS stations throughout the time series and the black circles have a 750 m radius, indicating the data selection radius of Paper II.

The shortest distance between a ICESat-2 flight track and the GNSS station is approximately 50-100 m at GLS2 and 500-600 m at GLS3. The distance between GLS2 and the flight track might be short enough, for a direct comparison between their surface elevation results to be possible. Both, because the surface slope at GLS2 is relatively flat (see appendix B fig. 7). But also because the GLS2 moved less than 10 m yr^{-1}, rendering it less critical to correct the surface elevation measured by the GNSS station, for SEC caused by position change.

Making an assessment of ICESat-2 altimetry from SEC products such as Hansen et al. (c) comes with a different set of challenges. Because the product covers the entire GrIS the assessment can be made for all three GLISN stations. However, the product provides results in 5 km grid cells. The coarse spatial resolution introduces a big uncertainty at each station, but it also makes any effort to correct for movement of the GNSS stations redundant, as the fastest moving of the three has a velocity of approximately 30 m yr^{-1} (Hansen et al., a). Furthermore, the product has a yearly time resolution. Leaving us with one data point for comparison at GLS1 and GLS2 and two data points for comparison at GLS3. Although one or two measurements from ICESat-2 per station are a small sample size, the product and GLISN stations results are easily comparable as the dates used to calculate SEC from the GNSS time series can be selected to fit the satellite product.

4.4. Change in GNSS-IR footprint

Figure 1.7 clearly demonstrate the GNSS-IR footprint depends on two things: the RH and the elevation angle. When using GNSS-IR to measure changes in RH, as done in Paper II and Paper III, it is therefore important to note the GNSS-IR footprint gets smaller when the RH decreases. When using GNSS-IR to measure tide water, changes in footprint are taking into account by making a $\dot{\mathbf{h}}$ correction (Larson et al., 2013). However, when measuring snow accumulation the changes in GNSS-IR footprint are ignored because the

method relies on the surrounding surface to be flat. This criteria is met in Paper II where we measured changes in RH over the interior of the GrIS, which is generally considered flat a surface.

In Paper III we measured changes in snow thickness over bedrock, which in Greenland is generally not considered a flat surface. In spite of this we still disregard the changes in the GNSS-IR footprint based on two things. One, all GNET stations are installed on relatively short mounds, which means the GNSS-IR footprint is generally small, reducing the likelihood of extreme surface topography changes in the GNSS-IR footprint. Two, Paper III showed snow build up to a smooth surface making it less important whether a winter RH is derived from a reflection in the same horizontal distance to the antenna as the correspondent summer RH.

Nevertheless, it is important to be aware of how much the topography change with distance, as it might be necessary to restrict the elevation angle interval to exclude extreme topography features. An example of summer surface changes caused by a difference in distance to the GNSS station can be seen in figure 4.4, which shows the summer surface at TIMM derived from processing the same data with three different elevation angle intervals ([5:15], [15:25] and [5:25]). The first excludes multipath frequencies caused by signal reflections closest to the station. The second excluding multipath frequencies caused by signal reflections furthest from the station. The third includes both of the above mentioned footprints. Overall the three different surfaces show more or less the same shape. However, it is clear the surface derived from the elevation angle interval [5:15] have azimuth angles where the surface strongly disagree with the other surfaces and generally has a larger standard deviation.

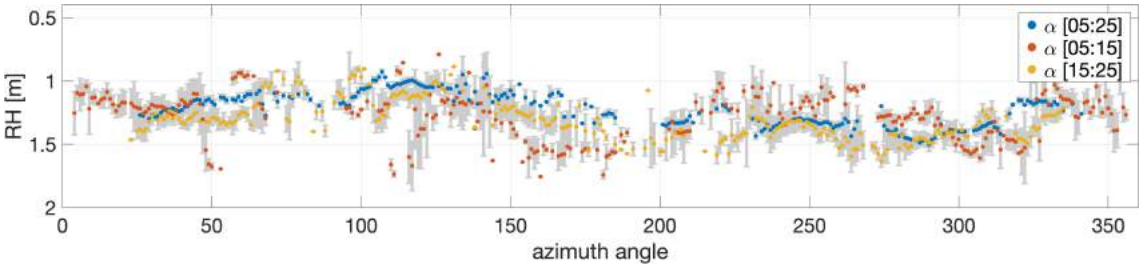

Figure 4.4: The derived summer surface at GNET station TIMM, found using the method presented in Paper III, allowing for signal reflections from three different elevation angle intervals: blue [5 : 25], red [5 : 15] and yellow [15 : 25].

4.5. Variations in date availability when using GNSS-IR

When using GNSS-IR to measure snow thickness on an uneven surface, such as bedrock, there are more obstacle to be aware of than just the GNSS-IR footprint, which is apparent when looking at the results in Chapter 3. At TIMM there are three things to be aware of, in addition to the GNSS-IR footprint. The first is a lag of summer surface signal reflections in azimuth angles between 125 and 230 degrees (see fig. 3.2). The sparse number of summer surface signal reflections highlights the importance of only deriving snow thickness from measurements with the same azimuth angle. Simply taking the daily average might skew the results because measurements from a relatively large part of the GNSS-IR footprint only contribute to the average part of the year. The second is the time periods without data. Because GNET stations are left alone for most of the year we can only speculate to the reason why the snow thickness time series is broken in the winters of 2019-2020 and 2020-2021 (fig. 3.2). Figure 4.5 shows the uplift time series does not

break at these points in time, which suggests the gaps caused by the RH getting to small to resolve. Unfortunately, there is no obvious solution to this problem besides raising the GNSS antenna to avoid it in the future. However, as GNET is primarily used for geodetic purposes that is out of the question, as it would beak the geodetic time series. The third is a tendency for ice build up on the GNSS antenna. In the RH time series this can be seen as a reduction in the number of derived RH, but as that could also be caused by other things, the only way to validate antenna ice build up is by discrepancies in the derived position (see fig. 4.5).

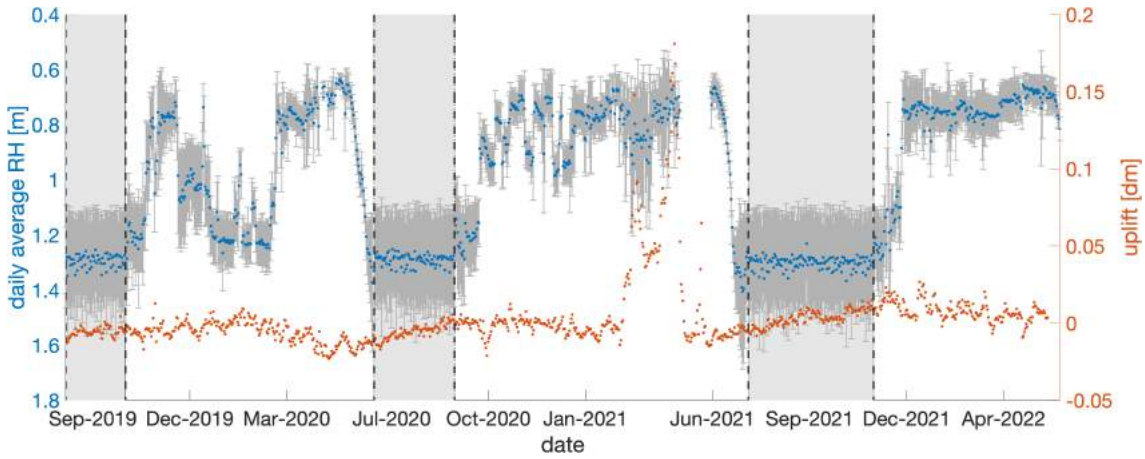

Figure 4.5: left yaxis) Daily average RH from the gnssrefl software with the y axis inverted, to provide a visual intuitive interpretation. The light grey boxes with black dashed side lines indicate the three bare soil time periods used to derive the summer surface. right yaxis) change in vertical land motion measured by TIMM.

At KMJP the snow thickness is calculated using only RH values derived in the azimuth interval [0:100]. When looking at the result from the every azimuth the RH seem more or less constant throughout the time series (see fig. 3.3). However, when zooming in on azimuth angle interval [0:100] it becomes clear snow is building and melting in this direction (fig. 3.3). Initially this might seem strange but when looking at the derived summer surface a possible explanation become clear (see fig. 4.6). Where the NORD summer surface primarily varies between a RH of 1 and 1.5 m, the KMJP summer surface varies between a RH of 1 and 4.5 m. The sloping of part of the surface could very well discourage snow build up and the data gab around azimuth angle 175 could be caused the surface being to tall for the RH to be resolved.

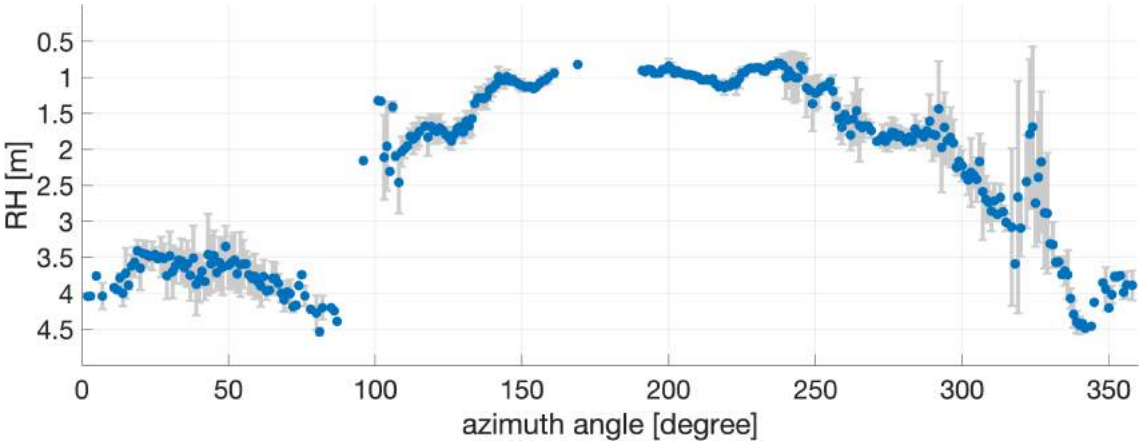

Figure 4.6: The derived summer surface at GNET station KMJP found using the method presented in Paper III.

4.6. Additional GNSS stations In Greenland

The three studies included in this thesis all show how valuable GNSS stations in Greenland, both on and off the ice sheet, can be when studying the on going effects of climate change. Recommendations for additional GNSS stations could be made based on all three. Although the current GNET stations are scattered fairly evenly along the Greenland coastline (see fig. 1.1) there are several locations where a new station could be useful. If a recommendation should be based on the results from Paper I, Zachariae Isstrøm would be an obvious suggestion. It would be both natural and informative to find and study the time lag between uplift and discharge at the largest outlet glaciers in Greenland. If using Andersen et al. (2019) or Mankoff et al. (2020) as a reference for which outlet glaciers are the largest, Zachariae Isstrøm is the only one of the eight largest outlet glaciers that does not have a GNSS station close to its grounding line.

If a recommendation should be based on the results from Paper III and Chapter 3, the suggestion would be quite different. As mentioned above it is not possible to raise the GNSS antenna on a GNET station. However, it is not unheard of to install a twin station next to an existing station to get overlapping time series. A twin station installed next to TIMM with a taller antenna mount would solve the problem of the RH getting to small to resolve during winter in the future.

If a recommendation should be based on the results from Paper II, a network of GNSS stations should be installed on the interior of the ice sheet, which is even more essential now that the three GLISN stations are buried by snow. Such a network should be located in the north as satellite data availability is higher on the northern part of the ice sheet, due to the satellite flight tracks being closer together, thus increasing the likelihood of the stations ability to validate future satellite missions. Currently the Programme for Monitoring of the Greenland Ice Sheet (PROMICE) are testing whether having a lower quality GNSS antenna on their weather stations are a possibility (Dahl-Jensen et al., 2022), but as the PROMICE stations does not cover the interior part of the ice sheet a separate network would be preferable.

4.7. Future work

Besides finishing the work started in Chaptor 3, it could be interesting to see if other parameters can be derived using GNSS-IR to process data from GNET stations. As mentioned in the introduction (section 1.6.2), GNSS-IR can be used to derive other products than the RH. Using GNSS-IR to derive soil moisture requires that the RH is constant, which figure 3.4 clearly shows is the case at SCBY. SCBY is thus an ideal test site for evaluation as to whether this can be done in Greenland. Should deriving soil moisture turn out to be possible at SCBY, the natural next step would be to investigate whether it is also possible in the bare soil intervals at other stations.

CHAPTER 5

Conclusion

The Global Navigation Satellite System was designed to measure very precisely the position and deformation of the Earth's crust and until recently, that was primarily what it was used for. However, within the last decade more use cases have been presented and new processing methods have been developed.

The overall objective of this PhD project was to develop new approaches for studying Greenland using GNSS data and contribute to knowledge of the ongoing effects of global climate change, both on and off the ice sheet. This objective was meet by dividing the project into three individual studies, each using GNSS data to investigate a different aspect of Greenland.

The objective of the first study was to explain GNSS observed uplift of bedrock near the three largest outlet glaciers in Greenland: Jakobshavn Isbræ, Kangerlussuaq and Helheim. By comparing the elastic component of vertical land motion with solid ice discharge we found a time lag between the two time series. Because the relationship between the two time series is linear, and the secular trend had been removed from both, we can reconstruct dynamic ice loss from GNSS uplift and, due to the time lag established, predict near future dynamic discharge. The length of the time lag, which is also the length of the prediction, varies from glacier to glacier. We found the longest time lag of 10.4 months at Jakobshavn Isbræ and the shortest of 11 days at Helheim, showing the ice viscosity of the three glacier are different from one another.

The objective of the second study was to assess the ability of CryoSat-2 altimetry to capture both long and short-term elevation changes to the interior of the GrIS and show the advantage of performing the assessment with permanent GNSS stations that measure throughout the year. The strength of the method was in our ability to derive a precise daily surface elevation time series from the GNSS stations by processing the data in two different way and combining the results. We found surface elevation change from CryoSat-2 altimetry was able to capture both short and long-term changes observed by the GNSS stations. However, the results were best at the northern most station, where a high density of CryoSat-2 data made it possible to efficiently correct for surface topography.

The objective of the third study was to show terrain corrected snow thickness on bedrock can be derived using data from GNET stations. The snow thickness results at Station Nord shows a distinct pattern with snow primarily building up through winter and maintaining a high snow thickness until the onset of melt, which is marked by a rapid decrease in snow thickness. Furthermore, our results snow the snow builds up to an approximately flat surface, despite variation in topography beneath it.

Bibliography

S. Adhikari, E. Ivins, and E. Larour. Mass transport waves amplified by intense greenland melt and detected in solid earth deformation. *Geophysical Research Letters*, 44(10): 4965–4975, 2017.

J. K. Andersen, R. S. Fausto, K. Hansen, J. E. Box, S. B. Andersen, A. P. Ahlstrøm, D. van As, M. Citterio, W. Colgan, N. B. Karlsson, et al. Update of annual calving front lines for 47 marine terminating outlet glaciers in greenland (1999–2018). *Geological Survey of Denmark and Greenland Bulletin*, 2019.

K. D. Anderson. Determination of water level and tides using interferometric observations of gps signals. *Journal of Atmospheric and Oceanic Technology*, 17(8):1118–1127, 2000.

A. Aschwanden, M. A. Fahnestock, M. Truffer, D. J. Brinkerhoff, R. Hock, C. Khroulev, R. Mottram, and S. A. Khan. Contribution of the greenland ice sheet to sea level over the next millennium. *Science advances*, 5(6):eaav9396, 2019.

P. Axelrad, K. Larson, and B. Jones. Use of the correct satellite repeat period to characterize and reduce site-specific multipath errors. In *Proceedings of the 18th International Technical Meeting of the Satellite Division of The Institute of Navigation (ION GNSS 2005)*, pages 2638–2648, 2005.

J. L. Bamber, J. A. Griggs, R. T. W. L. Hurkmans, J. A. Dowdeswell, S. P. Gogineni, I. Howat, J. Mouginot, J. Paden, S. Palmer, E. Rignot, and D. Steinhage. A new bed elevation dataset for greenland. *The Cryosphere*, 7(2):499–510, 2013. doi: 10.5194/tc-7-499-2013. URL https://tc.copernicus.org/articles/7/499/2013/.

V. R. Barletta, L. S. Sørensen, and R. Forsberg. Scatter of mass changes estimates at basin scale for greenland and antarctica. *Cryosphere*, 7(5), 2013.

J. Benedicto, S. Dinwiddy, G. Gatti, R. Lucas, and M. Lugert. Galileo: Satellite system design. In *European Space Agency*. Citeseer, 2000.

M. Bevis, J. Wahr, S. A. Khan, F. B. Madsen, A. Brown, M. Willis, E. Kendrick, P. Knudsen, J. E. Box, T. van Dam, et al. Bedrock displacements in greenland manifest ice mass variations, climate cycles and climate change. *Proceedings of the National Academy of Sciences*, 109(30):11944–11948, 2012.

K. M. Brunt, R. L. Hawley, E. R. Lutz, M. Studinger, J. G. Sonntag, M. A. Hofton, L. C. Andrews, and T. A. Neumann. Assessment of nasa airborne laser altimetry data using ground-based gps data near summit station, greenland. *The Cryosphere*, 11(2):681–692, 2017.

E. Cardellach, C. Ao, M. De la Torre Juárez, and G. Hajj. Carrier phase delay altimetry with gps-reflection/occultation interferometry from low earth orbiters. *Geophysical Research Letters*, 31(10), 2004.

J. Chen, C. Wilson, and B. Tapley. Satellite gravity measurements confirm accelerated melting of greenland ice sheet. *science*, 313(5795):1958–1960, 2006.

C. Chew, E. E. Small, and K. M. Larson. An algorithm for soil moisture estimation using gps-interferometric reflectometry for bare and vegetated soil. *GPS solutions*, 20(3): 525–537, 2016.

J. Christmann, R. Müller, and A. Humbert. On nonlinear strain theory for a viscoelastic material model and its implications for calving of ice shelves. *Journal of Glaciology*, 65 (250):212–224, 2019.

S. Chuang, Y. Wenting, S. Weiwei, L. Yidong, Z. Rui, et al. Glonass pseudorange inter-channel biases and their effects on combined gps/glonass precise point positioning. *GPS solutions*, 17(4):439–451, 2013.

T. S. Dahl-Jensen, M. Citterio, J. Jakobsen, A. P. Ahlstrøm, K. M. Larson, and S. A. Khan. Snow depth measurements by gnss-ir at an automatic weather station, nuk-k. *Remote Sensing*, 14(11):2563, 2022.

W. Dansgaard, S. J. Johnsen, H. B. Clausen, D. Dahl-Jensen, N. S. Gundestrup, C. U. Hammer, C. S. Hvidberg, J. P. Steffensen, A. Sveinbjörnsdottir, J. Jouzel, et al. Evidence for general instability of past climate from a 250-kyr ice-core record. *nature*, 364 (6434):218–220, 1993.

R. Detrick and K. Anderson. Arctic pi continuous - gls1-glisn 1 p.s., unavco, gps/gnss observations dataset, 2011a. URL https://www.unavco.org/data/gps-gnss/data-access-methods/dai1/select_data.php?code=GLS1&gid=3138&ds=2&parent_link=Permanent&pview=original&filter_data_availability=checked&from_date=2011-08-13&to_date=2021-06-30.

R. Detrick and K. Anderson. Arctic pi continuous - gls3-glisn 3 p.s., unavco, gps/gnss observations dataset, 2011b. URL https://www.unavco.org/data/gps-gnss/data-access-methods/dai1/select_data.php?code=GLS3&gid=2995&ds=13&parent_link=Permanent&pview=original&filter_data_availability=checked&from_date=2011-07-21&to_date=2022-05-18.

R. Detrick and K. Anderson. Arctic pi continuous - gls2-glisn 2 p.s., unavco, gps/gnss observations dataset, 2012. URL https://www.unavco.org/data/gps-gnss/data-access-methods/dai1/select_data.php?code=GLS2&gid=3138&ds=3&parent_link=Permanent&pview=original&filter_data_availability=checked&from_date=2011-06-07&to_date=2021-09-10.

X. Fettweis, S. Hofer, U. Krebs-Kanzow, C. Amory, T. Aoki, C. J. Berends, A. Born, J. E. Box, A. Delhasse, K. Fujita, et al. Grsmbmip: intercomparison of the modelled 1980–2012 surface mass balance over the greenland ice sheet. *The Cryosphere*, 14(11): 3935–3958, 2020.

Y. Georgiadou and A. Kleusberg. On carrier signal multipath effects in relative gps positioning. *Manuscripta geodaetica*, 13(3):172–179, 1988.

C. Han, Y. Yang, and Z. Cai. Beidou navigation satellite system and its time scales. *Metrologia*, 48(4):S213, 2011.

K. Hansen, W. Colgan, K. M. Larson, M. J. Willis, V. Helm, and S. A. Khan. Assessment of esa cryosat-2 radar altimetry data using gnss data at three sites on the greenland ice sheet, a. submitted to Journal of Geophysical Research: Earth Surface.

K. Hansen, T. S. Dahl-Jensen, and L. Stenseng. Terrain corrected snow thickness from gnss-ir at station nord, b. draft intended for submission to the GEUS bulletin.

K. Hansen, M. Truffer, A. Aschwanden, K. Mankoff, M. Bevis, A. Humbert, M. R. van den Broeke, B. Noël, A. Bjørk, W. Colgan, K. H. Kjær, S. Adhikari, V. Barletta, and S. A. Khan. Estimating ice discharge at greenland's three largest outlet glaciers using local bedrock uplift. *Geophysical Research Letters*, 48(14):e2021GL094252, 2021.

N. Hansen, L. S. Sørensen, G. Spada, D. Melini, R. Mottram, and S. B. Simonsen, c. in preparation.

V. Helm, A. Humbert, and H. Miller. Elevation and elevation change of greenland and antarctica derived from cryosat-2. *The Cryosphere*, 8(4):1539–1559, 2014.

. IPCC. Climate change 2007: The physical science basis. contribution of working group i to the fourth assessment report of the intergovernmental panel on climate change [solomon, s., d. qin, m. manning, z. chen, m. marquis, k.b. averyt, m. tignor and h.l. miller (eds.)]. cambridge university press, cambridge, united kingdom and new york, ny, usa, 996 pp., 2007.

M. Karaim, M. Elsheikh, A. Noureldin, and R. Rustamov. Gnss error sources. *Multifunctional Operation and Application of GPS*, pages 69–85, 2018.

N. B. Karlsson, A. M. Solgaard, K. D. Mankoff, F. Gillet-Chaulet, J. A. MacGregor, J. E. Box, M. Citterio, W. T. Colgan, S. H. Larsen, K. K. Kjeldsen, et al. A first constraint on basal melt-water production of the greenland ice sheet. *Nature Communications*, 12 (1):1–10, 2021.

S. A. Khan, J. Wahr, E. Leuliette, T. van Dam, K. M. Larson, and O. Francis. Geodetic measurements of postglacial adjustments in greenland. *Journal of Geophysical Research: Solid Earth*, 113(B2), 2008.

S. A. Khan, J. Wahr, M. Bevis, I. Velicogna, and E. Kendrick. Spread of ice mass loss into northwest greenland observed by grace and gps. *Geophysical Research Letters*, 37(6), 2010.

S. A. Khan, K. H. Kjær, M. Bevis, J. L. Bamber, J. Wahr, K. K. Kjeldsen, A. A. Bjørk, N. J. Korsgaard, L. A. Stearns, M. R. Van Den Broeke, et al. Sustained mass loss of the northeast greenland ice sheet triggered by regional warming. *Nature Climate Change*, 4(4):292–299, 2014a.

S. A. Khan, K. K. Kjeldsen, K. H. Kjær, S. Bevan, A. Luckman, A. Aschwanden, A. A. Bjørk, N. J. Korsgaard, J. E. Box, M. van den Broeke, et al. Glacier dynamics at helheim and kangerdlugssuaq glaciers, southeast greenland, since the little ice age. *The Cryosphere*, 8(4):1497–1507, 2014b.

S. A. Khan, A. A. Bjørk, J. L. Bamber, M. Morlighem, M. Bevis, K. H. Kjær, J. Mouginot, A. Løkkegaard, D. M. Holland, A. Aschwanden, et al. Centennial response of greenland's three largest outlet glaciers. *Nature communications*, 11(1):1–9, 2020.

A. Khazendar, I. G. Fenty, D. Carroll, A. Gardner, C. M. Lee, I. Fukumori, O. Wang, H. Zhang, H. Seroussi, D. Moller, et al. Interruption of two decades of jakobshavn isbrae acceleration and thinning as regional ocean cools. *Nature Geoscience*, 12(4): 277–283, 2019.

M. D. King, I. M. Howat, S. G. Candela, M. J. Noh, S. Jeong, B. P. Noël, M. R. van den Broeke, B. Wouters, and A. Negrete. Dynamic ice loss from the greenland ice sheet driven by sustained glacier retreat. *Communications Earth & Environment*, 1(1):1–7, 2020.

K. K. Kjeldsen, J. Mortensen, J. Bendtsen, D. Petersen, K. Lennert, and S. Rysgaard. Ice-dammed lake drainage cools and raises surface salinities in a tidewater outlet glacier fjord, west greenland. *Journal of Geophysical Research: Earth Surface*, 119(6):1310–1321, 2014.

K. K. Kjeldsen, N. J. Korsgaard, A. A. Bjørk, S. A. Khan, J. E. Box, S. Funder, N. K. Larsen, J. L. Bamber, W. Colgan, M. Van Den Broeke, et al. Spatial and temporal distribution of mass loss from the greenland ice sheet since ad 1900. *Nature*, 528(7582):396–400, 2015.

K. M. Larson. Gnss reflections code, 2021. URL https://github.com/kristinemlarson/gnssrefl.

K. M. Larson, E. E. Small, E. D. Gutmann, A. L. Bilich, J. J. Braun, and V. U. Zavorotny. Use of gps receivers as a soil moisture network for water cycle studies. *Geophysical Research Letters*, 35(24), 2008.

K. M. Larson, J. J. Braun, E. E. Small, V. U. Zavorotny, E. D. Gutmann, and A. L. Bilich. Gps multipath and its relation to near-surface soil moisture content. *IEEE Journal of Selected Topics in Applied Earth Observations and Remote Sensing*, 3(1):91–99, 2009.

K. M. Larson, R. D. Ray, F. G. Nievinski, and J. T. Freymueller. The accidental tide gauge: a gps reflection case study from kachemak bay, alaska. *IEEE Geoscience and Remote Sensing Letters*, 10(5):1200–1204, 2013.

K. M. Larson, J. Wahr, and P. K. Munneke. Constraints on snow accumulation and firn density in greenland using gps receivers. *Journal of Glaciology*, 61(225):101–114, 2015.

K. M. Larson, M. MacFerrin, and T. Nylen. Brief communication: Update on the gps reflection technique for measuring snow accumulation in greenland. *The Cryosphere*, 14(6):1985–1988, 2020.

T. Lenton, H. Held, E. Kriegler, J. Hall, W. Lucht, S. Rahmstorf, and H. Schellnhuber. Tipping elements in the earth's climate system, p. natl. acad. sci., 105, 1786–1793, 2008.

A. Levermann, T. Albrecht, R. Winkelmann, M. Martin, M. Haseloff, and I. Joughin. Parameterization for subgrid-scale motion of ice-shelf calving fronts. *The Cryosphere*, 6: 273–286, 2012.

L. E. Lisiecki and M. E. Raymo. A pliocene-pleistocene stack of 57 globally distributed benthic δ18o records. *Paleoceanography*, 20(1), 2005.

N. R. Lomb. Least-squares frequency analysis of unequally spaced data. *Astrophysics and space science*, 39(2):447–462, 1976.

X. Luo, S. Schaufler, M. Branzanti, and J. Chen. Assessing the benefits of galileo to high-precision gnss positioning–rtk, ppp and post-processing. *Advances in Space Research*, 68(12):4916–4931, 2021.

K. D. Mankoff, W. Colgan, A. Solgaard, N. B. Karlsson, A. P. Ahlstrøm, D. van As, J. E. Box, S. A. Khan, K. K. Kjeldsen, J. Mouginot, and R. S. Fausto. Greenland ice sheet solid ice discharge from 1986 through 2017. *Earth System Science Data*, 11(2):769–786, 2019. doi: 10.5194/essd-11-769-2019. URL https://essd.copernicus.org/articles/11/769/2019/.

K. D. Mankoff, A. Solgaard, W. Colgan, A. P. Ahlstrøm, S. A. Khan, and R. S. Fausto. Greenland ice sheet solid ice discharge from 1986 through march 2020. *Earth System Science Data*, 12(2):1367–1383, 2020.

M. McMillan, A. Shepherd, A. Muir, J. Gaudelli, A. E. Hogg, and R. Cullen. Assessment of cryosat-2 interferometric and non-interferometric sar altimetry over ice sheets. *Advances in Space Research*, 62(6):1281–1291, 2018.

J. G. McNeff. The global positioning system. *IEEE Transactions on Microwave theory and techniques*, 50(3):645–652, 2002.

M. Meredith, M. Sommerkorn, S. Cassotta, C. Derksen, A. Ekaykin, A. Hollowed, G. Kofinas, A. Mackintosh, J. Melbourne-Thomas, M. Muelbert, G. Ottersen, H. Pritchard, and E. Schuur. Polar regions. In: IPCC Special Report on the Oceans and Cryosphere in a Changing Climate. [Pörtner, H.-O., Roberts, D.C., Masson-Delmotte, V., Zhai, P., Tignor, M., Poloczanska, E., Mintenbeck, K., Alegría, A., Nicolai, M., Okem, A.,. Petzold, J., Rama, B. and Weyer, N.M. (eds.)]. In press. 2019.

T. Moon, M. Fisher, H. Simonoko, and T. Stafford. Qgreenland, Mar. 2021. URL https://doi.org/10.5281/zenodo.6369184.

T. A. Moon, M. L. Druckenmiller, and R. L. E. Thoman. Arctic Report Card 2021. https://doi.org/10.25923/5s0f-5163. 2021.

J. Mouginot, E. Rignot, A. A. Bjørk, M. Van den Broeke, R. Millan, M. Morlighem, B. Noël, B. Scheuchl, and M. Wood. Forty-six years of greenland ice sheet mass balance from 1972 to 2018. *Proceedings of the national academy of sciences*, 116(19):9239–9244, 2019.

S. Nghiem, D. Hall, T. Mote, M. Tedesco, M. Albert, K. Keegan, C. Shuman, N. DiGirolamo, and G. Neumann. The extreme melt across the greenland ice sheet in 2012. *Geophysical Research Letters*, 39(20), 2012.

F. G. Nievinski and K. M. Larson. Forward modeling of gps multipath for near-surface reflectometry and positioning applications. *GPS solutions*, 18(2):309–322, 2014.

J. Nilsson, P. Vallelonga, S. B. Simonsen, L. S. Sørensen, R. Forsberg, D. Dahl-Jensen, M. Hirabayashi, K. Goto-Azuma, C. S. Hvidberg, H. A. Kjær, et al. Greenland 2012 melt event effects on cryosat-2 radar altimetry. *Geophysical Research Letters*, 42(10): 3919–3926, 2015.

H. D. Pritchard, R. J. Arthern, D. G. Vaughan, and L. A. Edwards. Extensive dynamic thinning on the margins of the greenland and antarctic ice sheets. *Nature*, 461(7266): 971–975, 2009.

M. Rankl, J. J. Fürst, A. Humbert, and M. H. Braun. Dynamic changes on the wilkins ice shelf during the 2006–2009 retreat derived from satellite observations. *The Cryosphere*, 11(3):1199–1211, 2017.

S. Revnivykh, A. Bolkunov, A. Serdyukov, and O. Montenbruck. Glonass. In *Springer Handbook of Global Navigation Satellite Systems*, pages 219–245. Springer, 2017.

E. Rignot and P. Kanagaratnam. Changes in the velocity structure of the greenland ice sheet. *Science*, 311(5763):986–990, 2006.

C. Roesler and K. M. Larson. Software tools for gnss interferometric reflectometry (gnss-ir). *GPS solutions*, 22(3):1–10, 2018.

I. Sasgen, B. Wouters, A. S. Gardner, M. D. King, M. Tedesco, F. W. Landerer, C. Dahle, H. Save, and X. Fettweis. Return to rapid ice loss in greenland and record loss in 2019 detected by the grace-fo satellites. *Communications Earth & Environment*, 1(1):1–8, 2020.

T. Schenk, B. Csatho, C. van der Veen, and D. McCormick. Fusion of multi-sensor surface elevation data for improved characterization of rapidly changing outlet glaciers in greenland. *Remote sensing of environment*, 149:239–251, 2014.

A. Shepherd, E. Ivins, E. Rignot, B. Smith, M. van Den Broeke, I. Velicogna, P. Whitehouse, K. Briggs, I. Joughin, G. Krinner, et al. Mass balance of the greenland ice sheet from 1992 to 2018. *Nature*, 579(7798):233–239, 2020.

B. Smith, H. A. Fricker, N. Holschuh, A. S. Gardner, S. Adusumilli, K. M. Brunt, B. Csatho, K. Harbeck, A. Huth, T. Neumann, J. Nilsson, and M. R. Siegfried. Land ice height-retrieval algorithm for nasa's icesat-2 photon-counting laser altimeter. *Remote Sensing of Environment*, 233:111352, 2019. ISSN 0034-4257. doi: https://doi.org/10.1016/j.rse.2019.111352. URL https://www.sciencedirect.com/science/article/pii/S0034425719303712.

A. Solgaard and A. Kusk. Winter Ice Velocity Mosaics for the Greenland Ice Sheet from Sentinel-1 Edition 1, 2021. URL https://doi.org/10.22008/FK2/8BM1IZ.

A. Stokholm, S. M. Hvidegaard, R. Forsberg, and S. B. Simonsen. Validation of airborne and satellite altimetry data by arctic truck citizen science. *GEUS Bulletin*, 47, 2021.

U. G. Survey and E. D. Center, 2022. URL https://earthexplorer.usgs.gov.

M. R. Van den Broeke, E. M. Enderlin, I. M. Howat, P. Kuipers Munneke, B. P. Noël, W. J. Van De Berg, E. Van Meijgaard, and B. Wouters. On the recent contribution of the greenland ice sheet to sea level change. *The Cryosphere*, 10(5):1933–1946, 2016.

J. van Wessem, M. R. van den Broeke, and S. Lhermitte. Data set: Yearly racmo2.3p2 variables, Apr. 2022. URL https://doi.org/10.5281/zenodo.6602723.

K. van't Klooster. Ers-1, european remote-sensing satellite was launched 20 years ago. In *2011 21st International Crimean Conference" Microwave & Telecommunication Technology"*, pages 117–118. IEEE, 2011.

I. Velicogna. Increasing rates of ice mass loss from the greenland and antarctic ice sheets revealed by grace. *Geophysical Research Letters*, 36(19), 2009.

I. Velicogna and J. Wahr. Acceleration of greenland ice mass loss in spring 2004. *Nature*, 443(7109):329–331, 2006.

W. T. Vetterling, S. A. Teukolsky, W. H. Press, and B. P. Flannery. *Numerical recipes in Fortran*. Number BOOK. Cambridge University Press, 1992.

J. Wahr, S. A. Khan, T. van Dam, L. Liu, J. H. van Angelen, M. R. van den Broeke, and C. M. Meertens. The use of gps horizontals for loading studies, with applications to northern california and southeast greenland. *Journal of Geophysical Research: Solid Earth*, 118(4):1795–1806, 2013.

W. Wan, K. M. Larson, E. E. Small, C. C. Chew, and J. J. Braun. Using geodetic gps receivers to measure vegetation water content. *Gps Solutions*, 19(2):237–248, 2015.

H. Wang, L. Xiang, L. Jia, L. Jiang, Z. Wang, B. Hu, and P. Gao. Load love numbers and green's functions for elastic earth models prem, iasp91, ak135, and modified models

with refined crustal structure from crust 2.0. *Computers & Geosciences*, 49:190–199, 2012.

Appendix A

Paper I

AGU ADVANCING EARTH AND SPACE SCIENCE

Geophysical Research Letters

RESEARCH LETTER
10.1029/2021GL094252

Estimating Ice Discharge at Greenland's Three Largest Outlet Glaciers Using Local Bedrock Uplift

Karina Hansen[1], Martin Truffer[2], Andy Aschwanden[2,3], Kenneth Mankoff[3], Michael Bevis[4], Angelika Humbert[5], Michiel R. van den Broeke[6], Brice Noël[6], Anders Bjørk[7], William Colgan[3], Kurt H. Kjær[8], Surendra Adhikari[9], Valentina Barletta[1], and Shfaqat A. Khan[1]

[1]DTU Space, Technical University of Denmark, Kongens Lyngby, Denmark, [2]Geophysical Institute, University of Alaska Fairbanks, Fairbanks, AK, USA, [3]Department of Glaciology and Climate, Geological Survey of Denmark and Greenland, Copenhagen, Denmark, [4]School of Earth Sciences, Ohio State University, Colombus, OH, USA, [5]Alfred-Wegener-Institut Helmholtz Zentrum für Polar- und Meeresforschung, Germany and University of Bremen, Bremerhaven, Germany, [6]Institute for Marine and Atmospheric Research Utrecht, Utrecht University, Utrecht, The Netherlands, [7]Department of Geosciences and Natural Resources, University of Copenhagen, Copenhagen, Denmark, [8]Centre for GeoGenetics, Globe Institute, University of Copenhagen, Copenhagen, Denmark, [9]Jet Propulsion Laboratory, California Institute of Technology, Pasadena, CA, USA

Key Points:

- A novel method to estimate dynamic ice loss of Greenland's three largest outlet glaciers, Jakobshavn, Kangerlussuaq, and Helheim glacier
- Dynamic thinning/thickening occurs 0.87 ± 0.07 years before speedup/slowdown at Jakobshavn Isbræ
- A similar time lag between change in uplift rate and flow speed change allows us to predict future ice discharge from past uplift

Supporting Information:

Supporting Information may be found in the online version of this article.

Correspondence to:

S. A. Khan,
abbas@space.dtu.dk

Citation:

Hansen, K., Truffer, M., Aschwanden, A., Mankoff, K., Bevis, M., Humbert, A., et al. (2021). Estimating ice discharge at Greenland's three largest outlet glaciers using local bedrock uplift. *Geophysical Research Letters*, *48*, e2021GL094252. https://doi.org/10.1029/2021GL094252

Received 11 MAY 2021
Accepted 29 JUN 2021

Abstract We present a novel method to estimate dynamic ice loss of Greenland's three largest outlet glaciers: Jakobshavn Isbræ, Kangerlussuaq Glacier, and Helheim Glacier. We use Global Navigation Satellite System (GNSS) stations attached to bedrock to measure elastic displacements of the solid Earth caused by dynamic thinning near the glacier terminus. When we compare our results with discharge, we find a time lag between glacier speedup/slowdown and onset of dynamic thinning/thickening. Our results show that dynamic thinning/thickening on Jakobshavn Isbræ occurs 0.87 ± 0.07 years before speedup/slowdown. This implies that using GNSS time series we are able to predict speedup/slowdown of Jakobshavn Isbræ by up to 10.4 months. For Kangerlussuaq Glacier the lag between thinning/thickening and speedup/slowdown is 0.37 ± 0.17 years (4.4 months). Our methodology and results could be important for studies that attempt to model and understand mechanisms controlling short-term dynamic fluctuations of outlet glaciers in Greenland.

Plain Language Summary A wide range of sensors and methods have been used to study the changes of the Greenland Ice Sheet, including satellite gravimetry, altimetry, and the input-output method. Here, we present a novel fourth method to estimate dynamic ice loss of Greenland's three largest outlet glaciers: Jakobshavn Isbræ, Kangerlussuaq Glacier, and Helheim Glacier. We use Global Navigation Satellite System (GNSS) stations attached to bedrock to measure rise of land masses caused by ongoing ice mass loss near the glacier terminus. When we compare our results with ice discharge, we find a time lag between glacier speedup/slowdown and onset of dynamic induced thinning/thickening. Our results show that dynamic thinning/thickening on Jakobshavn Isbræ occurs 0.87 ± 0.07 years before speedup/slowdown. This implies that using GNSS uplift time series we are able to predict ice flow speedup/slowdown of Jakobshavn Isbræ by up to 10 months. For Kangerlussuaq Glacier and Helheim Glacier the lag between thinning/thickening and speedup/slowdown is 0.37 ± 0.17 years (4.4 months) and 0.03 ± 0.16 years, respectively. Our methodology and results could be important for studies that attempt to model and understand mechanisms controlling short-term dynamic fluctuations of outlet glaciers in Greenland.

1. Introduction

The mass loss of the Greenland Ice Sheet (GrIS) has been accelerating during the last quarter of a century (Bamber et al., 2018; Mouginot et al., 2019; Shepherd et al., 2020) with rapid and record-high ice-sheet-wide losses in 2012 and 2019 (Nghiem et al., 2012; Sasgen et al., 2020). A wide range of sensors and methods has been used to study the changes of the GrIS, including satellite gravimetry, altimetry, and the input-output method (IOM). Satellite gravity measurements from the Gravity Recovery and Climate Experiment (GRACE/-FO) can be converted into mass change (Chen et al., 2006; Sasgen et al., 2020; Velicogna &

Wahr, 2006). Airborne and satellite altimetry directly measure changes in ice surface heights and provide ice volume changes (Helm et al., 2014; Khan, Kjær et al., 2014; Pritchard et al., 2009). The IOM method depends on the discharge of ice through a flux gate (Rignot & Kanagaratnam, 2006) and surface mass balance (van den Broeke et al., 2016). Each of these methods has strengths and weaknesses. GRACE/-FO provides solutions at high temporal (monthly) but limited spatial resolution, and is thus not suitable to study individual glaciers (Barletta et al., 2013). Satellite and airborne altimetry provide high spatial resolution but limited temporal sampling (monthly to annual) (Khan, Kjeldsen et al., 2014; Schenk et al., 2014). IOM has the advantage that it identifies the physical processes responsible for the mass changes; it provides weekly solutions but is available only since 2016 (King et al., 2020; Mankoff et al., 2020) while yearly solutions are available since 1972 (Mouginot et al., 2019). However, while GRACE provides direct estimates of mass changes, both altimetry and IOM methods need several models and/or a priori knowledge to derive the ice mass changes, resulting in relatively high uncertainties in ice mass loss estimates.

Here, we present a novel method to estimate dynamic ice loss from direct observations of uplift of the elastic lithosphere using Global Navigation Satellite System (GNSS) stations attached to bedrock. GNSS stations are uplifting due to a combination of Glacial Isostatic Adjustment (GIA, caused by past ice-ocean mass exchange) and Earth's near instantaneous elastic response to present-day ice mass changes (Bevis et al., 2012). The Earth's elastic response can be isolated by applying a GIA correction. The magnitude of the elastic response to ice loss decreases with increasing distance from the ice loss center (Adhikari et al., 2017; Wahr et al., 2013), which means GNSS stations located near the center of ice loss will experience more uplift than GNSS stations further away. The Earth's elastic response is due to a combination of dynamic thinning of glaciers and surface mass balance (SMB) processes. However, these two contributors to surface elevation changes have different spatial patterns. Dynamic thinning is typically largest near the glacier terminus and along the main flowline and declines rapidly inland (Khan et al., 2020; Khazendar et al., 2019), while SMB-induced thinning has a much larger wavelength as SMB anomalies typically have a larger footprint. Earth's elastic response due to dynamic thinning can be isolated by applying a correction for SMB-induced elastic uplift. Therefore, a GNSS station located near a glacier front can sense and reveal the dynamic mass changes of that particular glacier. Here, we take advantage of GNSS stations located next to a major outlet glacier undergoing dynamic changes.

The major advantage of using GNSS data is the very high temporal resolution (daily) of elastic uplift estimates, caused by daily mass loss variability of the nearby glacier. In general, GNSS data may reveal short-term fluctuation of mass and significantly improve our understanding of glacier dynamics at daily timescales (Adhikari et al., 2017; Khan et al., 2010). Here, we focus on GNSS data from stations near Greenland's three largest outlet glaciers, Jakobshavn Isbræ (Sermeq Kujalleq, JI), Kangerlussuaq Glacier (KG), and Helheim Glacier (HG). We develop a relation between GNSS uplift and accumulated ice discharge for each glacier to examine recent ice variability.

2. Data and Methods

2.1. GNSS Data

To estimate GNSS site coordinates, we use the Gipsy X software package version GipsyX-1.3 developed at the Jet Propulsion Laboratory (JPL) and released in December 2019 (Bertiger et al., 2020). We use JPL final orbit products which include satellite orbits, satellite clock parameters, and Earth orientation parameters. The orbit products take the satellite antenna phase center offsets into account. The atmospheric delay parameters are modeled using the Vienna Mapping Function 1 (VMF1) with VMF1grid nominals (Boehm et al., 2006). Corrections are applied to remove the solid Earth tide and ocean tidal loading. The amplitudes and phases of the main ocean tidal loading terms are calculated using the Automatic Loading Provider (http://holt.oso.chalmers.se/loading/) applied to the FES2014b (Carrère et al., 2016) ocean tide model, including correction for center of mass motion of the Earth due to the ocean tides. The site coordinates are computed in the IGS14 frame (Altamimi et al., 2016).

Here, we use GNSS data from three sites located on bedrock near the margin of JI, KG, and HG. Figures 1a–1c shows the locations of the GNSS sites (red dots). KAGA is located near JI, KUAQ near KG, and HEL2 near HG. The blue curves in Figure 2 (left panels) show weekly solutions of bedrock uplift at KAGA,

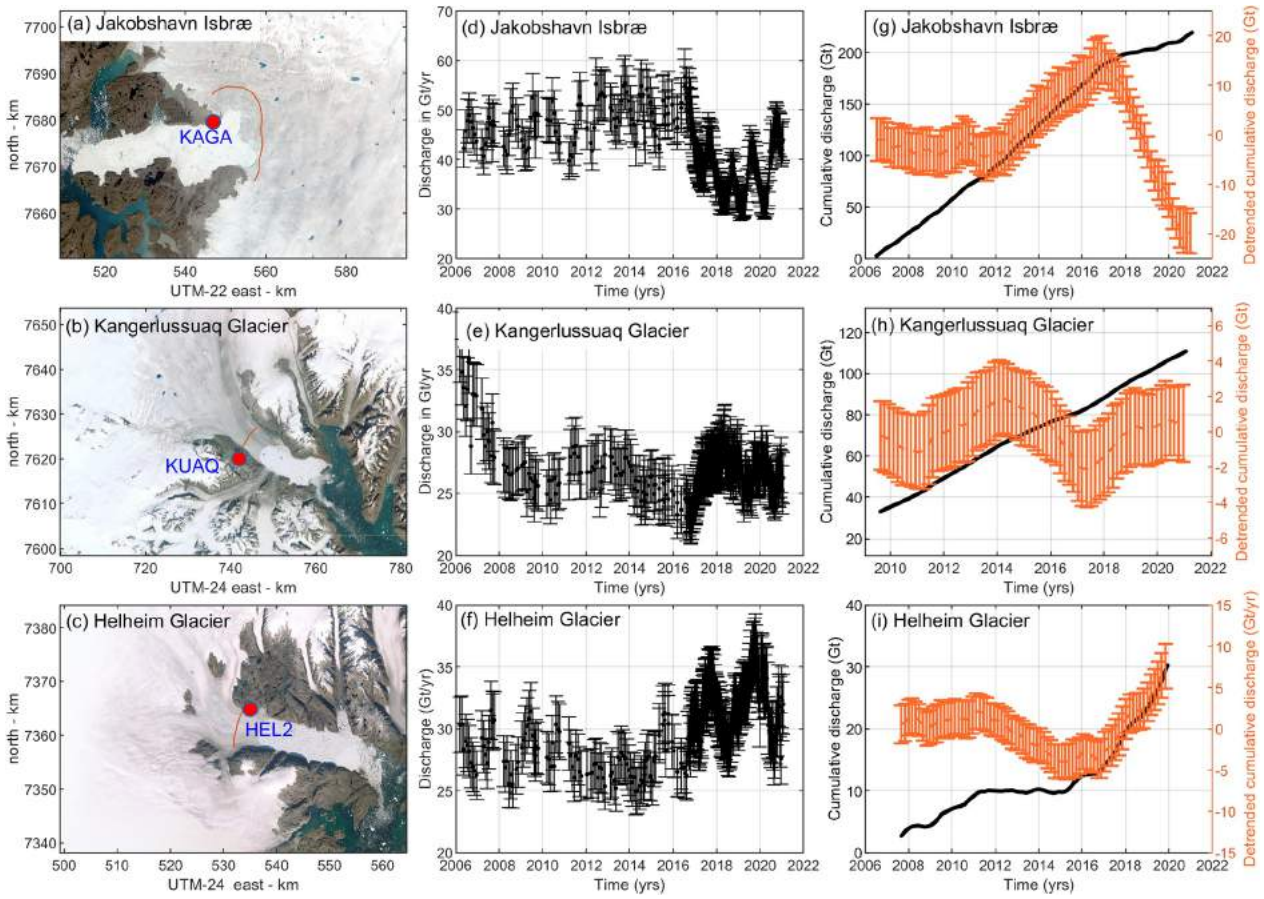

Figure 1. (a) Jakobshavn Isbræ and the location of flux gate (red curve) and GNSS station KAGA (red dot). (b) Kangerlussuaq Glacier and location of flux gate (red curve) and GNSS station KUAQ (red dot). (c) Helheim Glacier and location of flux gate (red curve) and GNSS station HEL2 (red dot). Time series of ice discharge from (d) JI, (e) KG, and (f) HG. Black curve denotes time series of cumulative ice discharge (left axis) from (g) JI, (h) KG, and (j) HG. Orange curve denotes time series of detrended cumulative ice discharge (right axis) from (g) JI, (h) KG, and (i) HG.

KUAQ, and HEL2, respectively. To isolate the uplift associated with ice dynamic processes, we must account for the uplift associated with SMB processes. The red curves in Figure 2 (left panels) denote estimated elastic uplift caused by SMB anomalies. This SMB correction is described in the following section.

2.1.1. Surface Mass Balance Correction

We use surface mass balance output products from the Regional Atmospheric Climate Model (RACMO2.3p2) at 5.5 km horizontal resolution statistically downscaled to 1 km resolution (Noël et al., 2018, 2019). SMB uncertainty has been previously estimated using the bias between modeled and observed SMB. We use an accumulation zone uncertainty of 17 mm w.e./yr and an ablation zone uncertainty of 70 mm w.e./yr (Noël et al., 2019).

To estimate "elastic uplift due to SMB," we integrate this SMB product over the drainage catchment of each glacier, and then remove the mean 1961–1990 to obtain SMB mass anomalies. Next, we convolve SMB mass anomalies with the Green's functions derived by Wang et al. (2012) for elastic Earth model iasp91 with refined crustal structure from Crust 2.0. The blue curves in Figure 2 (left panels) denote GNSS observed uplift corrected for "elastic uplift due to SMB," which we for simplicity denote as "elastic uplift due to ice dynamics." In Figure 2 (right panel), we detrend the "elastic uplift due to ice dynamics" weekly solutions by fitting and removing a linear term and yearly term, allowing us to ignore, for example, glacial isostatic adjustment correction.

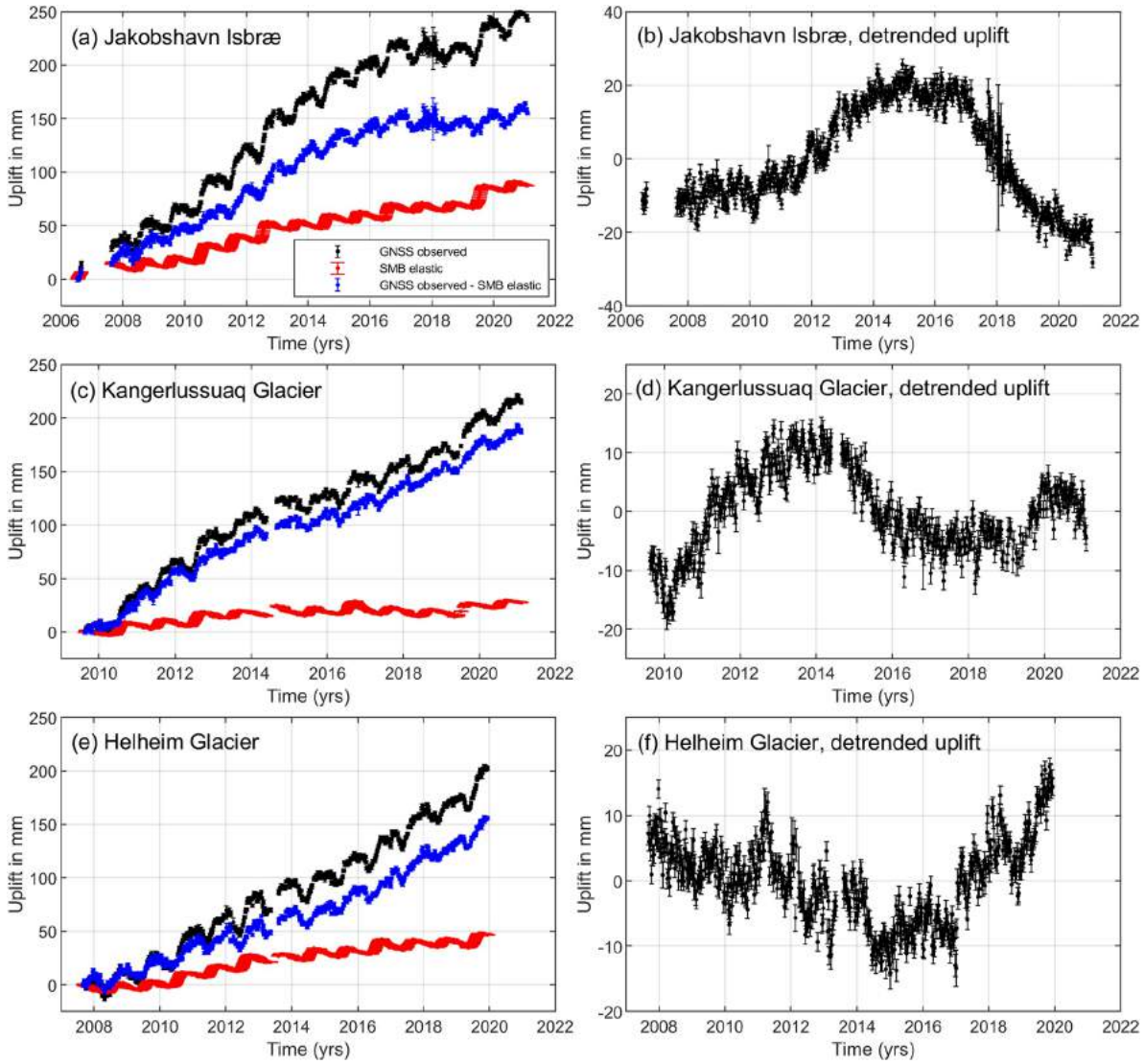

Figure 2. (a) Time series of weekly uplift solution at KAGA (black curve). Time series of elastic uplift due to SMB anomalies at KAGA (red curve). Observed uplift subtracted elastic uplift due to SMB (blue curve). (c) Same as (a) but for KUAQ. (f) Same as (a) but for HEL2. (b) Detrended observed uplift subtracted elastic uplift due to SMB at KAGA. (d) Detrended observed uplift subtracted elastic uplift due to SMB at KUAQ. (f) Detrended observed uplift subtracted elastic uplift due to SMB at HEL2.

2.1.2. Uncertainties of the Elastic Uplift Due to Ice Dynamics

We construct weekly averages of the daily vertical solutions shown to take the temporally correlated (non-Gaussian) noise into account. We use the root mean square (rms) of those averages to represent their uncertainties that we denote σ_{up_GPS}. To estimate uncertainties of the elastic uplift due to SMB, we convolve SMB uncertainty with the Green's functions and denote these uncertainties as σ_{up_SMB}. The total uncertainties of the "elastic uplift due to ice dynamics" (blue curves in Figures 2a, 2c and 2e) are $\sigma_{elas} = \sqrt{\sigma^2_{up\_GPS} + \sigma^2_{up\_SMB}}$.

The resulting uncertainty σ_{elas} is dominated by the GNSS data uncertainty which is typically1.5–2.0 mm, while the magnitude of σ_{up_SMB} is about 0.4 mm.

Table 1
Parameter k, t_0, and Trend for JI, KG, and HG

Glacier	k [Gt/mm]	t_0 [years]	Trend of dynamic ice loss [Gt/yr]
JI	0.67 ± 0.01	0.87 ± 0.07	16.2
KG	0.13 ± 0.01	0.37 ± 0.17	6.7
HG	0.46 ± 0.01	0.03 ± 0.16	1.6

2.2. Ice Discharge and Uncertainties

We use JI, KG, and HG solid ice discharge from December 2006 to 2020. Discharge is calculated across flux gates, from ice thickness (Morlighem et al., 2017) updated to account for surface elevation change (Khan et al., 2016), ice surface velocity (Solgaard et al., 2021), and an assumed ice density of 917 kg/m^3 (Mankoff et al., 2020). Gates are placed ∼5 km upstream from the terminus and limited to ice flowing >100 m/yr, based on the average 2015, 2016, and 2017 winter velocity as provided by MEaSUREs (Joughin et al., 2018). The largest uncertainties in estimated ice discharge are associated with ice thickness uncertainties (Morlighem et al., 2017), and ice density uncertainty due to crevasses.

Figures 1a–1c shows the location of flux gates for each glacier and Figures 1d–1f shows the ice discharge rate in Gt/yr. To estimate dynamic ice loss, we estimate cumulative discharge of each glacier and remove the associated basin-wide mean 1961–1990 SMB, which is typically assumed to characterize a near-equilibrium period (King et al., 2020). We estimate a 1961–1990 basin-wide mean SMB using RACMO2.3p2 of 29.9 Gt/yr for JI, 19.5 Gt/yr for KG, and 26.5 Gt/yr for HG. Figures 1g–1i shows the dynamic ice loss (black curve) and the detrended dynamic ice loss (orange curve). To detrend the dynamic ice loss, we fit and remove a linear term and yearly term.

2.3. Airborne and Satellite Laser Altimetry

To assess elevation changes of the ice surface over JI, we use repeat laser altimetry surveys from NASA's Airborne Topographic Mapper (ATM) flights during 2006–2019 (Studinger, 2014). The airborne altimetry measurements over the ice were conducted from March to May during annual campaigns as part of NASA's Operation IceBridge. NASA ended its Operation IceBridge measurement over Greenland in spring 2019. To assess ice surface elevation changes during 2019–2020, we use Land Ice Along-Track Height Product (ATL06) from ICESat-2 (Ice, Cloud, and land Elevation Satellite 2) launched on September 15, 2018, as part of NASA's Earth Observing System (Smith et al., 2020). To estimate elevation changes from 2019 to 2020, we use surface elevations from January to mid-May for 2019 and difference with surface elevations from January to mid-May for 2020.

3. Dynamic Ice Loss From GNSS Uplift

The time series of detrended dynamic ice loss from flow speed (Figure 1 right panels) represent dynamic changes of JI, KG, and HG, respectively. We denote the time series of detrended dynamic ice loss from flow speed as $D(t)$, where t is time. However, the time series of detrended elastic uplift (Figure 2 right panels) represent changes in uplift due to ice dynamics at JI, KG, and HG. We denote $U(t)$ as time series of detrended elastic uplift due to dynamic ice loss. For both detrended time series, positive anomalies reflect periods of higher than normal ice dynamic mass loss. We detrend the dynamic ice loss and uplift time series over a common time period at each glacier, so the anomalies in each record are equivalent. Estimated trends removed from dynamic ice loss time series are listed in Table 1.

$U(t)$ is the detrended elastic uplift due to dynamic ice loss and depends on the distance between the GNSS site and the center of the area undergoing dynamic thinning. Here, we assume that this distance is constant over the time period of comparison. $D(t)$ is the detrended discharge at the flux gate and depends on the flux gate location (see Text S1), ice flow speed and ice thickness at the flux gate. For a glacier that thins and speeds up simultaneously, we can assume a simple linear relation between $U(t)$ and $D(t)$. However, if the speed-up lags the thinning as a consequence of the thinning, we have to introduce a time lag between $U(t)$ and $D(t)$. Based on our timeseries we assume a simple linear relation between $U(t)$ and $D(t)$ with a time lag between the two time-series,

$$D\left(t\right) = k * U\left(t - t_0\right) \quad (1)$$

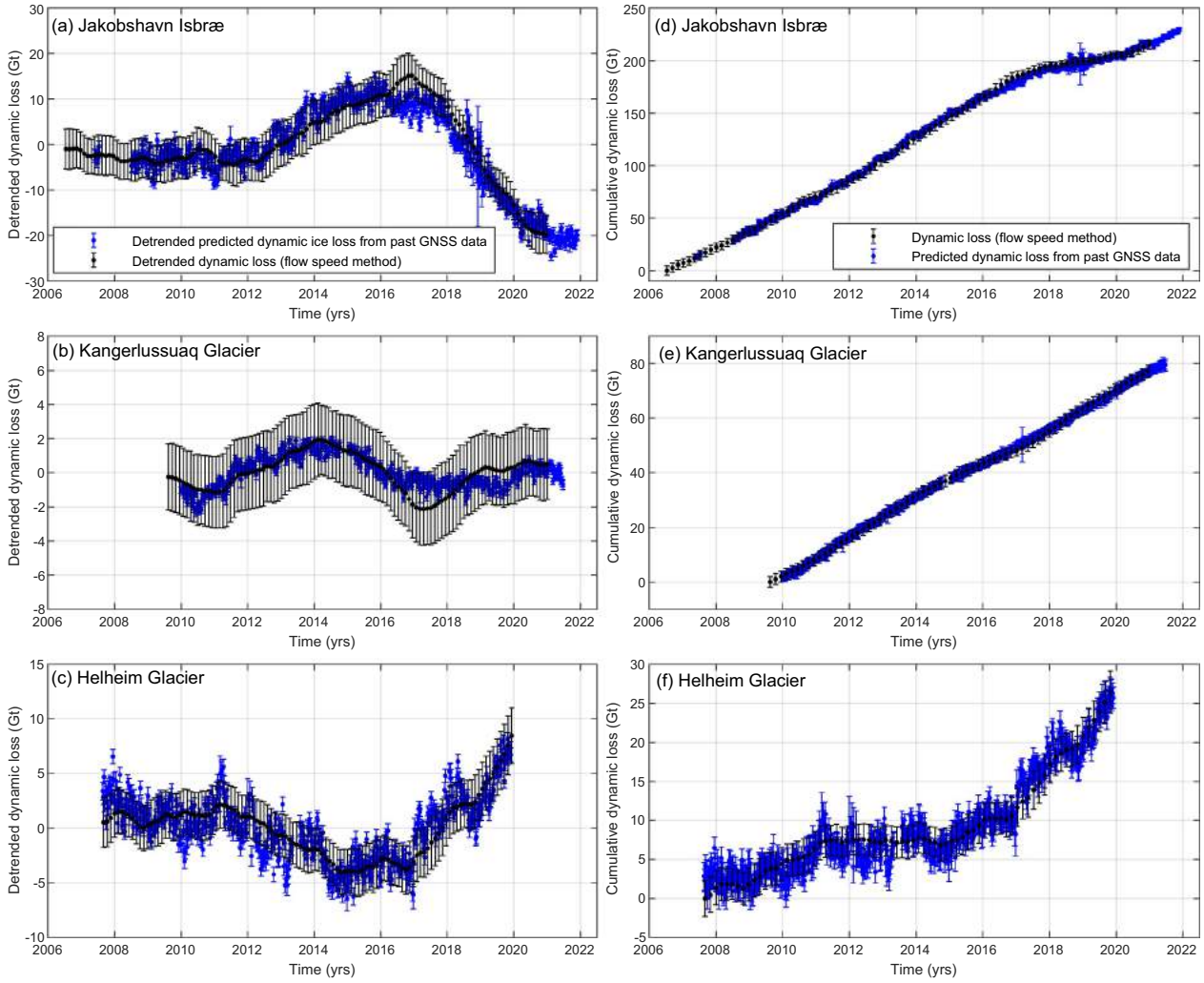

Figure 3. (a) Predicted detrended dynamic ice loss from past GNSS data at JI (blue curve) and ice flow method (black curve). (b) Same as (a) but for KG. (c) Same as (a) but for HG. (d) Cumulative dynamic ice loss from past GNSS data at JI (blue curve) and ice flow speed method (black curve). (e) Same as (d) but for KG. (f) Same as (d) but for HG.

where k is a constant that depends local geology and glaciohydrology and the distance between the GNSS site and the section of the glacier losing mass and has units of Gt/mm. t_0 is a constant time lag with units of years between detrended cumulative ice discharge $D(t)$ (Gt) and detrended cumulative bedrock uplift $U(t)$ (mm).

For each glacier, we estimate k and t_0 using least square adjustment. Figures 3a–3c shows time series of detrended dynamic ice loss from flow speed and detrended dynamic ice loss from GNSS using Equation 1. Table 1 shows our estimates of k and t_0 for JI, KG, and HG and their uncertainties (see Text S1).

Next, we use the detrended uplift time series $U(t)$ with associated parameters in Table 1 to reconstruct dynamic ice loss for JI, KG, and HG, respectively. Figures 3d–3f shows our reconstructed "dynamic ice loss from GNSS data" and "dynamic ice loss from ice flow speed." To reconstruct dynamic ice loss from GNSS uplift, we add the dynamic ice loss trend (see Table 1) that was removed when detrending dynamic ice loss time series in Figure 1 (right panels). Our method of estimating the relation between $U(t)$ and $D(t)$ and reconstruction of the dynamic ice loss from GNSS is independent of any secular trends that may affect GNSS data, for example, secular uplift due to glacial isostatic adjustment. Once a relation between uplift and dynamic ice loss has been established, we can use it to estimate dynamic ice loss from observed uplift

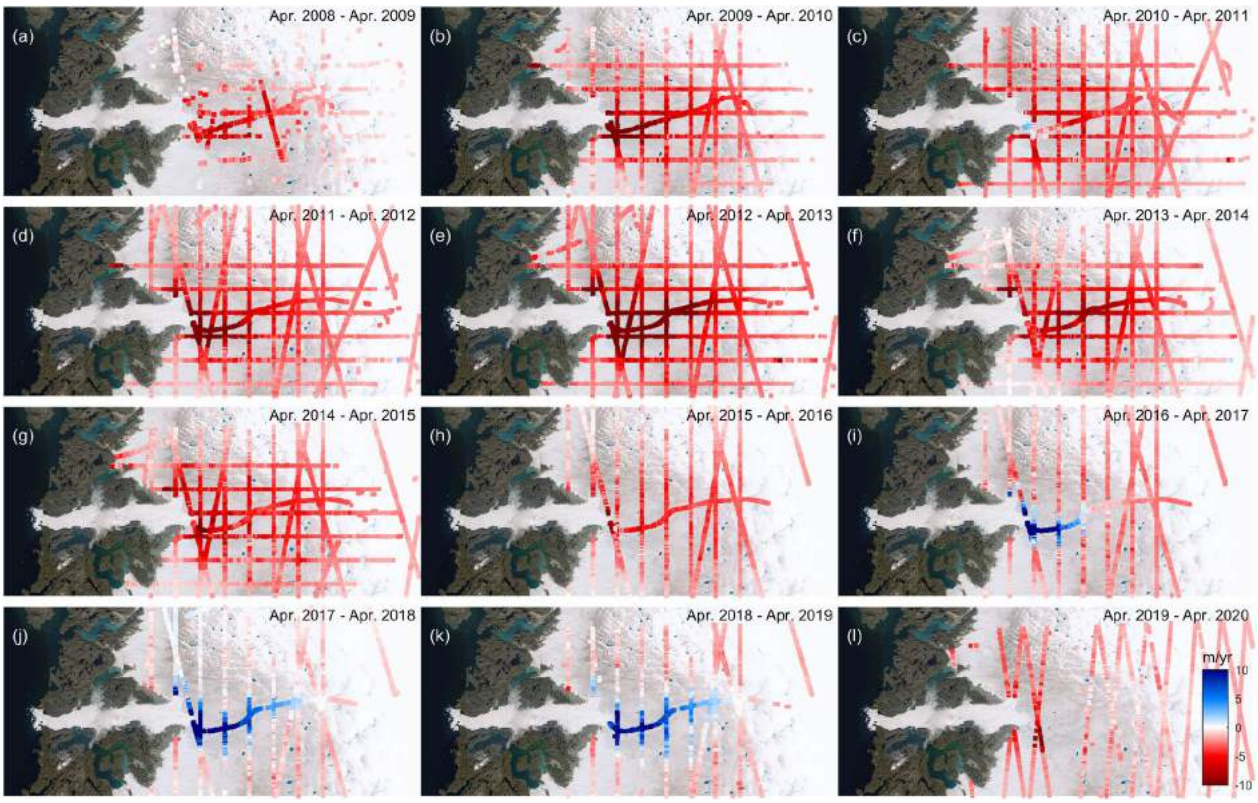

Figure 4. Elevation changes of Jakobshavn Isbræ in meters during (a) April 2008–April 2009, (b) April 2009–April 2010, (c) April 2010–April 2011, (d) April 2011–April 2012, (e) April 2012–April 2013, (f) April 2013–April 2014, (g) April 2014–April 2015, (h) April 2015–April 2016, (i) April 2016–April 2017, (j) April 2017–April 2018, (k) April 2018–April 2019, and (i) April 2019–April 2020. Background show Landsat image of JI from 2012.

from GNSS. In principle, the method can be used for any glacier that has a GNSS station located near the glacier terminus.

4. Results

The observed uplift at GNSS sites is an elastic response to mass changes due to a combination of complex patterns of SMB and dynamic induced response of JI, KG, and HG. By removing the SMB induced mass anomalies, we can isolate the dynamically-induced thinning. For each glacier, we find the relation between dynamic ice loss and uplift. Our results for HG (Figure 3f) show increased dynamic ice loss starting in 2017. HG lost a total of 10 ± 2 Gt during 2007.6–2017.0 (over a 9.4-year period) and 15 ± 2 Gt during 2017.0–2020.0 (over a 3-year period). Both methods, dynamic ice loss from flow speed and dynamic ice loss using GNSS, show acceleration in dynamic loss. The two methods provide consistent results for JI, KG, and HG, and the pairs of time-series (Figure 3) lie within their error bars. However, it should be noted that fluctuations in detrended dynamic ice loss are small for KG (from −2 to +2 Gt) (see Figure 3b), whereas JI fluctuations vary between −20 Gt and +10 Gt, and HG between −5 and +10 Gt.

In principle the time lag t_0 allows us to predict future dynamic loss from GNSS uplift. For JI we find a time lag of 0.87 ± 0.07 years between uplift and dynamic ice loss from flow speed, and thus we can predict dynamic ice loss until November 2021 (Figures 3a and 3d). The time lags for KG (0.37 ± 0.17 years, Figures 3b and 3e) and HG (0.03 ± 0.16 years, Figures 3c and 3f) are much shorter. To investigate and understand this time lag, we create time series of elevation changes for JI based on airborne and satellite laser altimetry data. Figure 4 shows annual elevation changes (April to April) from airborne and satellite altimetry between April 2008 and April 2020. The thinning is dominated by ice dynamics (Khazendar et al., 2019).

Airborne and satellite altimetry suggest thickening of JI from April 2016 to April 2017 (Figure 4i), in line with recent studies, for example, (Khazendar et al., 2019). However, discharge from flow speed shows a large decline in discharge in summer 2017 (Figure 1d) and was consistently lower the following years. This suggests a time lag between the onset of glacier speedup/slowdown and the onset of dynamic thinning/thickening, where dynamic thinning/thickening occurs before speedup/slowdown.

Our method of using GNSS uplift time series to estimate dynamic ice loss has its limitations. A GNSS station located between two glaciers will not be able to sense which glacier is speeding up and undergoing dynamic thinning/thickening. Elastic uplift depends on the distance between the GNSS site and the glacier losing mass. However, usage of horizontal displacements could be a potential solution, as horizontal displacements depend on the distance and direction between a GNSS site and the area losing mass (Adhikari et al., 2017; Wahr et al., 2013). The optimal location to install a GNSS station to monitor dynamic changes is close to the grounding line or close to the source that is, undergoing dynamic charges. A shorter distance between GNSS site and the source gives a larger elastic response.

5. Discussion and Conclusions

The Greenland GPS Network (GNET) was built to observe and monitor the Earth's instantaneous elastic adjustment to contemporary ice loss, and its delayed viscoelastic response to long past changes in ice mass (Bevis et al., 2012). Constant velocity displacements are hard to interpret, because both elastic and viscoelastic adjustments are capable of producing steady crustal velocities, so any attempt to separate them is largely an exercise in modeling. But accelerating and transient displacements are driven by accelerating or transient changes in ice mass, and thus manifest the combined effects of shifting SMB and dynamic mass change (Bevis et al., 2019). Changes in dynamic ice loss at major outlet glaciers produce large elastic signals at nearby GNSS stations, but these signals decay in space much more rapidly than do the signals produced by major shifts in SMB. Thus, displacement transients seen at GNET stations close to major outlet glaciers, which are not found in the time series of more distant GNET stations, have a local origin.

Here, we present a novel method to estimate dynamic ice loss of JI, KG, and HG that uses uplift from GNSS data. Our method provides weekly estimates of dynamic ice loss from 2007 to 2020 for JI and HG and 2009 to 2020 for KG (Figure 3). Our results show that uplift inferred from the GNSS data is a direct consequence of mass change with no time lag. The fact that the measured discharge at the flux gates lags the elastic response indicates that the ice flow at the flux gates reacts to dynamic thinning that has already occurred. This lag between glacier thinning/thickening and speedup/slowdown allows us to use uplift from GNSS data to predict discharge at the flux gates, by up to 10.4 months for JI and 4.5 months for KG.

One mechanism that we suggest leading to the lag is the delay of the viscous response to a change in load of a glacier. With ice being a viscoelastic material, a change in load is initially leading to an elastic response, while the viscous response is taking a month to years to fully develop, depending on the viscosity (Christmann et al., 2019; Rankl et al., 2017). Calving front motion induces softening of the ice that subsequently leads to acceleration (Bondzio et al., 2017). This implies that, locally, there might be a time lag between mass loss from the satellite altimetry method and the mass loss from the IOM method. Thus, on short timescales, the two mass loss methods should be compared with caution. We further note that the time lag between thinning/thickening and speedup/slowdown depends on the overall trend of the dynamic ice loss of the considered glacier. Table 1 suggests the time lag (column 3) increases linearly with the trend of dynamic ice loss (column 4). However, further investigation using more glaciers is needed to draw any conclusions. The method presented here may be used for other glaciers, for example, in Alaska or Antarctica that have a GNSS site located reasonably close (up to ~30 km) to their center of dynamic mass loss.

Data Availability Statement

Glacier front position and discharge data is available at the following data repository: https://dataverse01.geus.dk/dataset.xhtml?persistentId=doi:10.22008/promice/data/ice_discharge/d/v02.GNSS uplift data and Ice surface elevation changes is available at the following data repository: https://datadryad.org/stash/share/CTZfCRbKv3t3vEXloNHVdVycpFXza_yuBK38Lo6syDc.

Acknowledgments
The authors thank Jeffrey T. Freymueller and an anonymous reviewer for their constructive comments. S. A. Khan acknowledges support from the INTAROS GA No. 727890 funded by European Union's Horizon 2020 Research and Innovation Programme. B. Noël was funded by the NWO VENI grant VI.Veni.192.019. A. Bjørk was funded by the Carlsberg Foundation (Grant CF17-0529). K. D. Mankoff was funded by PROMICE. M. R. van den Broeke acknowledges support from the Netherlands Earth System Science Centre (NESSC). W. Colgan acknowledges support from the Independent Research Fund Denmark (8049-00003B). A. Aschwanden was funded by NSF grant PLR-1603799.

References

Adhikari, S., Ivins, E. R., & Larour, E. (2017). Mass transport waves amplified by intense Greenland melt and detected in solid Earth deformation. *Geophysical Research Letters*, *44*(10), 4965–4975. https://doi.org/10.1002/2017gl073478

Altamimi, Z., Rebischung, P., Métivier, L., & Collilieux, X. (2016). ITRF2014: A new release of the International Terrestrial Reference Frame modeling nonlinear station motions. *Journal of Geophysical Research: Solid Earth*, *121*(8), 6109–6131. https://doi.org/10.1002/2016jb013098

Bamber, J. L., Westaway, R. M., Marzeion, B., & Wouters, B. (2018). The land ice contribution to sea level during the satellite era. *Environmental Research Letters*, *13*(6), 063008. https://doi.org/10.1088/1748-9326/aac2f0

Barletta, V. R., Sørensen, L. S., & Forsberg, R. (2013). Scatter of mass changes estimates at basin scale for Greenland and Antarctica. *The Cryosphere*, *7*(5), 1411–1432. https://doi.org/10.5194/tc-7-1411-2013

Bertiger, W., Bar-Sever, Y., Dorsey, A., Haines, B., Harvey, N., Hemberger, D., et al. (2020). GipsyX/RTGx, a new tool set for space geodetic operations and research. *Advances in Space Research*, *66*(3), 469–489. https://doi.org/10.1016/j.asr.2020.04.015

Bevis, M., Harig, C., Khan, S. A., Brown, A., Simons, F. J., Willis, M., et al. (2019). Accelerating changes in ice mass within Greenland, and the ice sheet's sensitivity to atmospheric forcing. *Proceedings of the National Academy of Sciences*, *116*(6), 1934–1939. https://doi.org/10.1073/pnas.1806562116

Bevis, M., Wahr, J., Khan, S. A., Madsen, F. B., Brown, A., Willis, M., et al. (2012). Bedrock displacements in Greenland manifest ice mass variations, climate cycles and climate change. *Proceedings of the National Academy of Sciences*, *109*(30), 1944–11948. https://doi.org/10.1073/pnas.1204664109

Boehm, J., Werl, B., & Schuh, H. (2006). Troposphere mapping functions for GPS and very long baseline interferometry from European Center for Medium-Range Weather Forecasts operational analysis data. *Journal of Geophysical Research: Solid Earth*, *111*(B2). B02406. https://doi.org/10.1029/2005jb003629

Bondzio, J. H., Morlighem, M., Seroussi, H., Kleiner, T., Rückamp, M., Mouginot, J., et al. (2017). The mechanisms behind Jakobshavn Isbræ's acceleration and mass loss: A 3-D thermomechanical model study. *Geophysical Research Letters*, *44*, 6252–6260. https://doi.org/10.1002/2017GL073309

Carrère, L., Lyard, F., Cancet, M., Guillot, A., & Picot, N. (2016). FES 2014, a new tidal model—Validation results and perspectives for improvements. In *Proceedings of the ESA living planet symposium* (pp. 9–13).

Chen, J. L., Wilson, C. R., & Tapley, B. D. (2006). Satellite gravity measurements confirm accelerated melting of Greenland ice sheet. *Science*, *313*(5795), 1958–1960. https://doi.org/10.1126/science.1129007

Christmann, J., Müller, R., & Humbert, A. (2019). On nonlinear strain theory for a viscoelastic material model and its implications for calving of ice shelves. *Journal of Glaciology*, *65*, 1–224. https://doi.org/10.1017/jog.2018.107

Helm, V., Humbert, A., & Miller, H. (2014). Elevation and elevation change of Greenland and Antarctica derived from CryoSat-2. *The Cryosphere*, *8*(4), 1539–1559. https://doi.org/10.5194/tc-8-1539-2014

Joughin, I., Smith, B. E., & Howat, I. M. (2018). A complete map of Greenland ice velocity derived from satellite data collected over 20 years. *Journal of Glaciology*, *64*(243), 1–11. https://doi.org/10.1017/jog.2017.73

Khan, S. A., Bjørk, A. A., Bamber, J. L., Morlighem, M., Bevis, M., Kjær, K. H., et al. (2020). Centennial response of Greenland's three largest outlet glaciers. *Nature Communications*, *11*, 5718. https://doi.org/10.1038/s41467-020-19580-5

Khan, S. A., Kjær, K. H., Bevis, M., Bamber, J. L., Wahr, J., Kjeldsen, K. K., et al. (2014). Sustained mass loss of the northeast Greenland ice sheet triggered by regional warming. *Nature Climate Change*, *4*(4), 292–299. https://doi.org/10.1038/nclimate2161

Khan, S. A., Kjeldsen, K. K., Kjær, K. H., Bevan, S., Luckman, A., Aschwanden, A., et al. (2014). Glacier dynamics at Helheim and Kangerdlugssuaq glaciers, southeast Greenland, since the Little Ice Age. *The Cryosphere*, *8*, 1497–1507. https://doi.org/10.5194/tc-8-1497-2014

Khan, S. A., Liu, L., Wahr, J., Howat, I., Joughin, I., van Dam, T., & Fleming, K. (2010). GPS measurements of crustal uplift near Jakobshavn Isbræ due to glacial ice mass loss. *Journal of Geophysical Research*, *115*, B09405. https://doi.org/10.1029/2010jb007490

Khan, S. A., Sasgen, I., Bevis, M., van Dam, T., Bamber, J. L., Wahr, J., et al. (2016). Geodetic measurements reveal similarities between post-Last Glacial Maximum and present-day mass loss from the Greenland ice sheet. *Science Advances*, *2*, e1600931. https://doi.org/10.1126/sciadv.1600931

Khazendar, A., Fenty, I. G., Carroll, D., Gardner, A., Lee, C. M., Fukumori, I., et al. (2019). Interruption of two decades of Jakobshavn Isbrae acceleration and thinning as regional ocean cools. *Nature Geoscience*, *12*(4), 277–283. https://doi.org/10.1038/s41561-019-0329-3

King, M. D., Howat, I. M., Candela, S. G., Noh, M. J., Jeong, S., Noël, B. P. Y., et al. (2020). Dynamic ice loss from the Greenland Ice Sheet driven by sustained glacier retreat. *Communications Earth & Environment*, *1*, 1. https://doi.org/10.1038/s43247-020-0001-2

Mankoff, K. D., Solgaard, A., Colgan, W., Ahlstrøm, A. P., Khan, S. A., & Fausto, R. S. (2020). Greenland Ice Sheet solid ice discharge from 1986 through March 2020. *Earth System Science Data*, *12*(2), 1367–1383. https://doi.org/10.5194/essd-12-1367-2020

Morlighem, M., Williams, C. N., Rignot, E., An, L., Arndt, J. E., Bamber, J. L., et al. (2017). BedMachine v3: Complete bed topography and ocean bathymetry mapping of Greenland from multi-beam echo sounding combined with mass conservation. *Geophysical Research Letters*, *44*, 11051–11061. https://doi.org/10.1002/2017gl074954

Mouginot, J., Rignot, E., Bjørk, A. A., Van den Broeke, M., Millan, R., Morlighem, M., et al. (2019). Forty-six years of Greenland Ice Sheet mass balance from 1972 to 2018. *Proceedings of the National Academy of Sciences*, *116*(19), 9239–9244. https://doi.org/10.1073/pnas.1904242116

Nghiem, S. V., Hall, D. K., Mote, T. L., Tedesco, M., Albert, M. R., Keegan, K., et al. (2012). The extreme melt across the Greenland ice sheet in 2012. *Geophysical Research Letters*, *39*(20). L20502. https://doi.org/10.1029/2012gl053611

Noël, B., van de Berg, W. J., Lhermitte, S., & van den Broeke, M. R. (2019). Rapid ablation zone expansion amplifies north Greenland mass loss. *Science Advances*, *5*(9), eaaw0123. https://doi.org/10.1126/sciadv.aaw0123

Noël, B., van de Berg, W. J., van Wessem, J. M., van Meijgaard, E., van As, D., Lenaerts, J. T. M., et al. (2018). Modeling the climate and surface mass balance of polar ice sheets using RACMO2-Part 1: Greenland (1958–2016). *The Cryosphere*, *12*, 811–831. https://doi.org/10.5194/tc-12-811-2018

Pritchard, H. D., Arthern, R. J., Vaughan, D. G., & Edwards, L. A. (2009). Extensive dynamic thinning on the margins of the Greenland and Antarctic ice sheets. *Nature*, *461*(7266), 971–975. https://doi.org/10.1038/nature08471

Rankl, M., Fürst, J. J., Humbert, A., & Braun, M. H. (2017). Dynamic changes on the Wilkins ice shelf during the 2006–2009 retreat derived from satellite observations. *The Cryosphere*, *11*, 1199–1211. https://doi.org/10.5194/tc-11-1199-2017

Rignot, E., & Kanagaratnam, P. (2006). Changes in the velocity structure of the Greenland Ice Sheet. *Science*, *311*(5763), 986–990. https://doi.org/10.1126/science.1121381

Sasgen, I., Wouters, B., Gardner, A. S., King, M. D., Tedesco, M., Landerer, F. W., et al. (2020). Return to rapid ice loss in Greenland and record loss in 2019 detected by the GRACE-FO satellites. *Communications Earth & Environment*, *1*(1), 1–8. https://doi.org/10.1038/s43247-020-0010-1

Schenk, T., Csatho, B., Van Der Veen, C., & McCormick, D. (2014). Fusion of multi-sensor surface elevation data for improved characterization of rapidly changing outlet glaciers in Greenland. *Remote Sensing of Environment*, *149*, 239–251. https://doi.org/10.1016/j.rse.2014.04.005

Shepherd, A., Ivins, E., Rignot, E., Smith, B., van Den Broeke, M., Velicogna, I., et al. (2020). Mass balance of the Greenland ice sheet from 1992 to 2018. *Nature*, *579*(7798), 233–239. https://doi.org/10.1038/s41586-019-1855-2

Smith, B., Fricker, H. A., Gardner, A., Siegfried, M. R., Adusumilli, S.,Csathó, B. M., et al. (2020). *ATLAS/ICESat-2 L3A land ice height, version 3. [2018–2020]*. NASA National Snow and Ice Data Center Distributed Active Archive Center. https://doi.org/10.5067/ATLAS/ATL06.003

Solgaard, A., Kusk, A., Boncori, J. P. M., Dall, J., Mankoff, K. D., Ahlstrøm, A. P., et al. (2021). Greenland ice velocity maps from the PROMICE project. *Earth System Science Data Discussions*, 1–29.

Studinger, M. (2014). *IceBridge ATM L2 Icessn elevation, slope, and roughness, version 2. [2011–2019]*. NASA National Snow and Ice Data Center Distributed Active Archive Center. Updated 2020. https://doi.org/10.5067/CPRXXK3F39RV

van den Broeke, M. R., Enderlin, E. M., Howat, I. M., Kuipers Munneke, P., Noël, B. P. Y., van de Berg, W. J., et al. (2016). On the recent contribution of the Greenland ice sheet to sea level change. *The Cryosphere*, *10*, 1933–1946. https://doi.org/10.5194/tc-10-1933-2016

Velicogna, I., & Wahr, J. (2006). Measurements of time-variable gravity show mass loss in Antarctica. *Science*, *311*(5768), 1754–1756. https://doi.org/10.1126/science.1123785

Wahr, J., Khan, S. A., van Dam, T., Liu, L., van Angelen, J. H., van den Broeke, M. R., & Meertens, C. M. (2013). The use of GPS horizontals for loading studies, with applications to northern California and southeast Greenland. *Journal of Geophysical Research: Solid Earth*, *118*, 1795–1806. https://doi.org/10.1002/jgrb.50104

Wang, H., Xiang, L., Jia, L., Jiang, L., Wang, Z., Hu, B., & Gao, P. (2012). Load Love numbers and Green's functions for elastic Earth models PREM, iasp91, ak135, and modified models with refined crustal structure from crust 2.0. *Computers & Geosciences*, *49*, 190–199. https://doi.org/10.1016/j.cageo.2012.06.022

[Geophysical Research Letters]

Supporting Information for

[Estimating ice discharge at Greenland's three largest outlet glaciers using local bedrock uplift]

[Karina Hansen[1], Martin Truffer[2], Andy Aschwanden[2,3], Kenneth Mankoff[3], Michael Bevis[4], Angelika Humbert[5], Michiel R. van den Broeke[6], Brice Noël[6], Anders Bjørk[7], William Colgan[3], Kurt H Kjær[8], Surendra Adhikari[9], Valentina Barletta[1], and Shfaqat A Khan[1*]]

[[1]DTU Space, Technical University of Denmark, Kgs. Lyngby, 2400, Denmark

[2]Geophysical Institute, University of Alaska Fairbanks, Fairbanks, AK, USA

[3]Department of Glaciology and Climate, Geological Survey of Denmark and Greenland, Denmark

[4]School of Earth Sciences, Ohio State University, USA

[5]Alfred-Wegener-Institut Helmholtz Zentrum für Polar- und Meeresforschung, Bremerhaven, Germany and University of Bremen, Germany

[6]Institute for Marine and Atmospheric research Utrecht, Utrecht University, Utrecht,

the Netherlands.

[7]Department of Geosciences and Natural Resources, University of Copenhagen, Denmark

[8]Centre for GeoGenetics, Globe Institute, University of Copenhagen, 1350 Copenhagen K, Denmark.

[9]Jet Propulsion Laboratory, California Institute of Technology, Pasadena, CA 91109, USA]

Contents of this file

Introduction

We test the sensitivity of the parameters, t_0 and *k,* to the location of flux gates. We estimate t_0 and *k* using discharge data through flux gates a and b (see figure S1). For JI and KG, the flux gate b is located approximately 5 km upstream relative to flux gate a. For HG, the flux gate b is located approximately 3 km downstream relative to flux gate a.

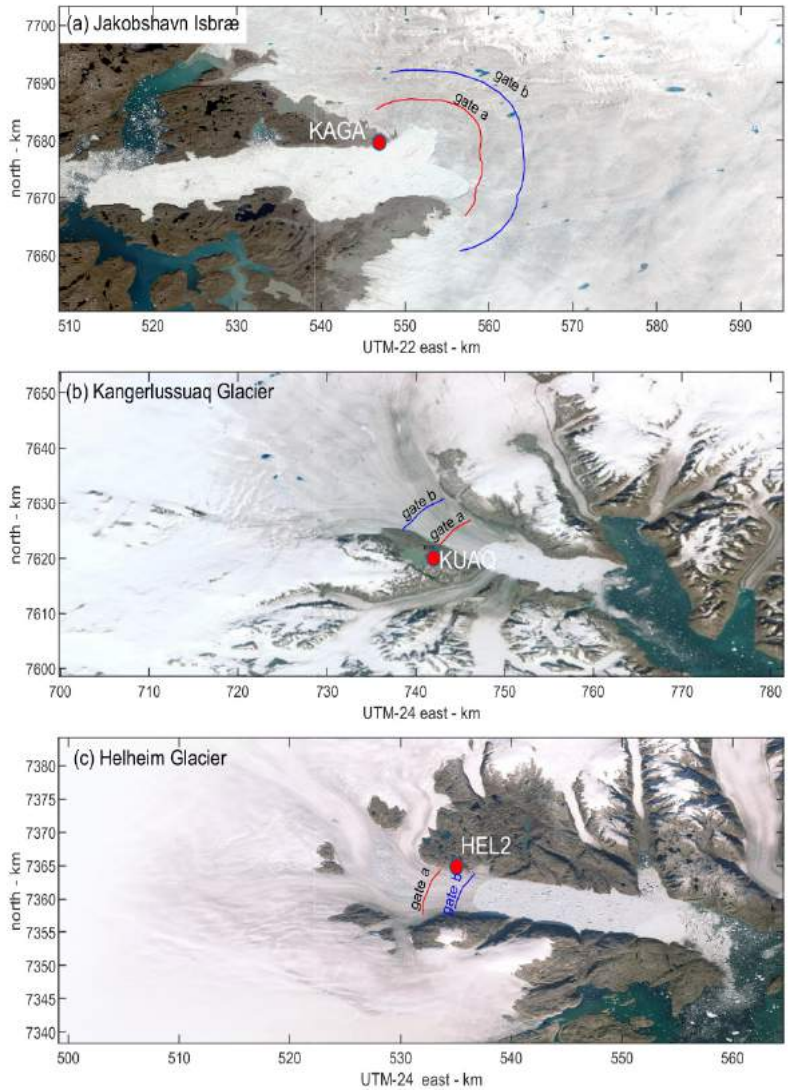

Figure S1. Location of flux gates on JI (a), KG (b) and HG (c).

For each flux gate, we estimate the associated parameters, t_0 and *k,* shown in table S1. The parameter *k* depends on e.g. ice thickness uncertainty in BedMachine, but also on the location of the flux gate. For example, a flux gate located 10 km inland from the grounding line will not capture dynamic changes that occur between the grounding line and the fluxgate. This affects *k,* since *k* depends on the cumulative discharge through the selected flux gate

The parameter *t* is the time lag between the glacier elevation change and flow speed change. For JI, KG, and HG, we use the difference in time lags estimated through gate a and b, as an expression of time lag uncertainty. However, moving the HG flux gate 5 km upstream gives large discharge errors as the ice stream splits into several ice streams. Therefore, we move the 3 km downstream, close to the glacier terminus.

Glacier	*k [Gt/mm]*	t_0 [years]
JI-gate a	0.67 ± 0.01	0.87 ± 0.02
JI-gate b	0.68 ± 0.01	0.80 ± 0.02
KG-gate a	0.13 ± 0.01	0.37 ± 0.03
KG-gate b	0.19 ± 0.01	0.54 ± 0.03
HG – gate a	0.46 ± 0.01	0.03 ± 0.05
HG – gate b	0.38 ± 0.01	0.19 ± 0.05

Table S1: Parameter *k*, $\boldsymbol{t_0}$ and trend for JI, KG and HG

We assign the time lag t_0 an uncertainty of 0.87-0.80=0.07 years for JI and uncertainty of 0.54-0.37=0.17 years for KG. For HG, we assign the time lag of HG an uncertainty of 0.19-0.03=0.16 years.

Appendix B

Paper II

Assessment of ESA CryoSat-2 radar altimetry data using GNSS data at three sites on the Greenland Ice Sheet

K. Hansen[1], W. Colgan[2], K. M. Larson[3], M. J. Willis[4], V. Helm[5], and S. A. Khan[1]

[1]DTU Space, Technical University of Denmark, Kongens Lyngby, 2800, Denmark
[2]Glaciology and climate, Geological Survey of Denmark and Greenland (GEUS), Denmark
[3]Department of Aerospace Engineering Sciences, University of Colorado, Boulder, CO 80309, USA
[4]CIRES and Department of Geological Sciences, University of Colorado, Boulder, CO 80309, USA
[5]Glaciology Section, Alfred Wegener Institute, Germany

Key Points:

- Surface elevation derived from Cryosat-2 radar altimetry capture both long- and extreme short-term change
- The magnitude and sign of yearly surface elevation change derived from GNSS varies significantly throughout the year
- April is the best month for an ice sheet wide yearly elevation change campaign

Corresponding author: Shfaqat Abbas Khan, abbas@space.dtu.dk

Abstract

Ten-year records of ice surface elevation changes derived from three GNSS stations (GLS1, GLS2 and GLS3) placed in the interior of the Greenland ice sheet are used to assess the ability of CryoSat-2 radar altimetry to capture surface elevation changes during 2010-2021. We use GNSS interferometric reflectometry (GNSS-IR) to derive time series of continuous daily surface elevations. We compare GNSS derived surface elevations with CryoSat-2 derived surface elevations and find CryoSat-2 performs best at the northernmost GNSS site (GLS3) with a maximum difference of 12cm. The other GNSS sites have a higher residual range because of poorer data availability and local surface variations. The number of CryoSat-2 data points are roughly doubled from GLS1 and GLS2 to GLS3. GLS3 Is located in a very flat area of the ice sheet and only moved 55m during 2011-2020. In contrast, GLS1 moved 292m in the same period. The strength of assessing satellite radar altimetry against permanent GNSS stations lie in the GNSS-IR methods ability to provide a continuous daily time series that clearly capture both long-term and extreme short-term changes. As extreme short-term changes in satellite radar altimetry time series may be perceived as an error or outlier on its own. The yearly surface elevation change ($\partial h/\partial t$) for every available date pair is calculated for all three GNSS derived surface elevation time series. $\partial h/\partial t$ have a big variation throughout the year and show April is the best month for an ice sheet wide yearly elevation change campaign. Whereas other months will give misleading results.

Plain Language Summary

Satellite radar altimetry data is used to calculate ice sheet wide surface elevation change in order to estimate mass changes to the Greenland ice sheet. One of the satellites used for this is called CryoSat-2. Here, we use data from three Global Navigation Satellite System (GNSS) stations to asses the ability of CryoSat-2 to capture short- and long-term elevation changes to the interior of the ice sheet from 2011 to 2021. The surface elevation change derived from CryoSat-2 has a low time resolution and big spatial footprint. whereas, the surface elevation changes derived from a GNSS station give a daily and very precise result, which is only true for a small area around the station. We find CryoSat-2 performs best at the northernmost GNSS station with a maximum difference of 12cm between the surface elevation change measurements. CryoSat-2 does not perform as well at the other locations because of poorer data availability and a steeper surface slope. The advantage of assessing CryoSat-2 data against continuous GNSS data is GNSS stations clearly capture extreme short-term changes, that may be perceived as an error in the satellite data. The GNSS derived surface elevation change also show how big variability there can be in a yearly surface elevation change measurement depending on what month the measurement is carried out. Combining the data from all the GNSS stations show April is the best month for a yearly elevation change measurement that represent the entire ice sheet.

1 Introduction

Satellite altimetry is an efficient technique for mapping changes in ice sheet and glacier surface elevation at high spatial resolution. Since the launch of the European Remote Sensing satellite (ERS) in June 1991, satellite radar and laser altimetry have provided continuous estimates of ice volume loss through several satellite missions (ERS1/2, ICESat, ICESat-2, and CryoSat-2). These satellite missions, which employ both laser and radar altimeters, have had differing spatial and temporal resolutions. Unlike laser pulses, radar pulses tend to penetrate through the surface snow. This makes the detection of potential biases in ice surface elevation time series especially important in radar altimetry applications.

Several previous studies have evaluated biases satellite altimetry data using external data. McMillan et al. (2018) assessed CryoSat-2 non-interferometric and interferimetric synthetic aperture rader (SAR and InSAR) altimetry over the Antarctic ice sheet by comparing the elevation change derived from both radar datasets to each other, as well as to independent elevations derived from Operation IceBridge laser altimetry. In comparison to the Operation IceBridge elevations, they found the average bias was smaller in the SAR data, but a statistical analysis showed a better agreement of elevation trends with the InSAR data. Overall, they found InSAR had improved precision, accuracy and coverage compared to SAR. The relative root-mean-square-difference (RMSD) between InSAR and Operation IceBridge derived elevation trends was ∼30%. Brunt et al. (2017) assessed the surface elevation bias and measurement precision of three airborne laser altimeters using data from ground-based global positioning system (GPS) surveys of an 11 km long track near Summit station in Greenland, from 2007 to 2016. This was done using both a nearest-neighbor analysis and a zone analysis approach. They found the surface elevation bias over the flat interior of the Greenland Ice Sheet (GrIS) was less than 12 cm for the three airborne altimeters used in the study. Stokholm et al. (2021) validated both airborne and satellite altimetry elevation change using GPS data collected during a traverse over the GrIS in 2018. First, they evaluated Operation IceBridge elevation change with the GPS data and found the average difference between the two to be 10.7 ±11.7 cm. Second, they evaluated CryoSat-2 elevation change with the GPS data and found an average bias of 92.3 ±65.7 cm between the two records. This substantial bias highlights the challenge of implementing systematic corrections for substantial depth penetration in radar altimetry. Nilsson et al. (2015) investigated the change in CryoSat-2 waveforms and elevation estimates over the 2012 melt event and interpreted their findings by comparison with in-situ surface elevation data and snow pit observations from the North Greenland Eemian (NEEM) ice drilling site. To derive more robust statistics, the analysis was performed on both a local and regional area around the NEEM camp. Their analysis suggested that the formation of a refrozen melt layer, which increased the reflective surface elevation, was responsible for an elevation increase of 56±26 cm observed in the CryoSat-2 data.

In this study, we assess the surface elevation change observed in CryoSat-2 radar altimetry data using three Global Navigation Satellite System (GNSS) time series with a duration of about 10 years and a daily time resolution. To avoid the issue of surface and volume scattering we only assess the ability to capture changes to the surface elevation, not the surface elevation it self. This is done under the assumption of a constant penetration depth over time. The strengths of this evaluation method are twofold. Firstly, we use the longest high resolution time series available to assess CryoSat-2 elevations changes. Secondly, we process the GNSS data in two different methods and combine the results to obtain the highest possible precision ice surface elevation change series.

2 Data description

2.1 GNSS data

For more than 10 years ground based GNSS stations have been monitoring the GrIS (Detrick & Anderson, 2011a, 2012, 2011b). The three GNSS stations GLS1, GLS2 and GLS3 were installed by the Greenland Ice Sheet Monitoring Network (GLISN) project in 2011 with the aim of precisely measuring the 3D movement of the GrIS (Clinton et al. (2014), fig. 1). The GNSS stations are located at DYE-2, Ice South Station and NEEM field camp (GLS1, GLS2 and GLS3 respectively) and will remain operational until buried by snow. Over the years the GNSS antennas have been raised to prevent this. GLS3 was moved to a new monument in June 2012 (Larson et al., 2020) shifting the station location approximately 2 meters.

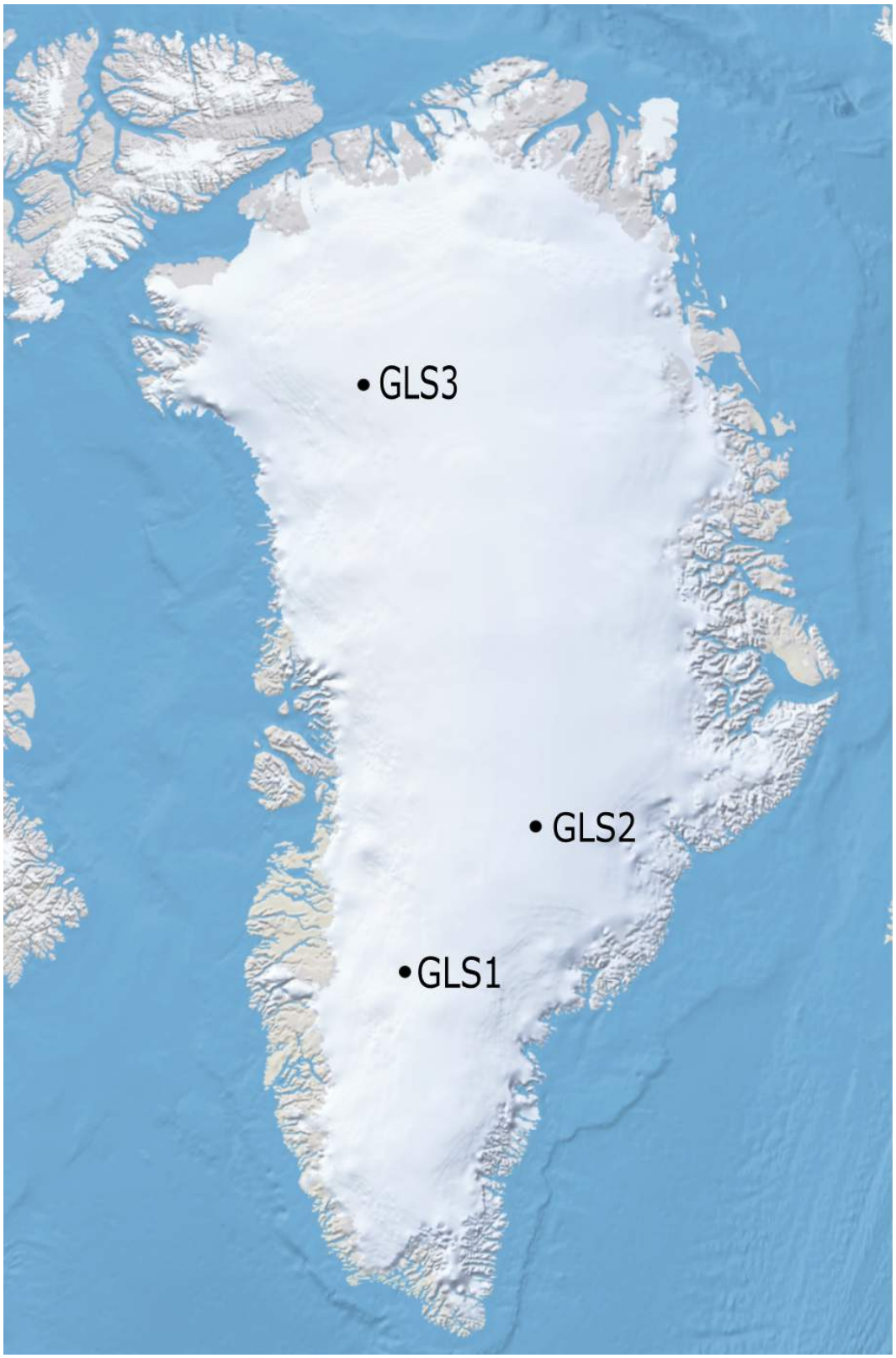

Figure 1. GNSS stations GLS1, GLS2 and GLS3 location on the Greenland ice sheet. Precise locations can be seen in table 1. The background map is provided by QGreenland (Moon et al., 2021) the blue area represent water, the grey bedrock and the white snow and ice.

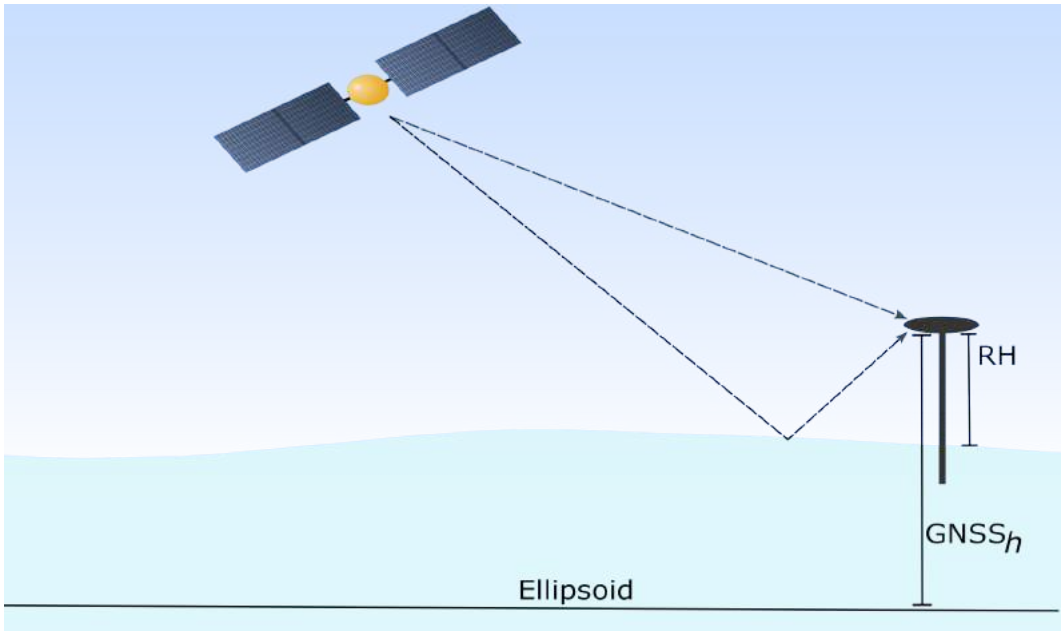

Figure 2. Ice surface elevation measurement using GNSS data. The GNSS antenna in constellation with the satellite illustrate how both the antenna 3D position and the RH is measured at a GNSS site. The direct signal from the satellite to the antenna is traditionally used to compute the 3D antenna position. The reflected signal bouncing of the ice surface interfere with the direct signal at the antenna. This interference pattern is used to compute the RH.

In this study the GNSS antenna and receiver constellation at the three stations only allow for data from the Global Positioning System (GPS) satellite constellation. In practise this means only GPS data is used, however we will keep referring to the stations and their data as GNSS. the GNSS data is processed in two ways to retrieve both the 3D antenna position referenced to the World Geodetic System 1984 (WGS84) geoid and the distance between the antenna and the ice surface. The signal received at the GNSS antenna is a combination of direct satellite signals and satellite signals that are reflected on the surrounding surface before reaching the antenna (see fig. 2). Studies show the noise the reflected signal add to the direct signal can be used to estimate the vertical distance between the GNSS antenna and the surface beneath it, also known as the reflector height (RH) (Larson et al., 2015; Roesler & Larson, 2018; Larson et al., 2020)).

The GNSS stations used in this study log a measurement every 15 seconds containing the information it receives from the multiple satellites it is constantly in contact with. This means it is possible to compute the ice surface elevation at the GNSS sites with a sub-daily time resolution needed. However, the daily time resolution we compute in this study is sufficient as it is significantly better than the time resolution of a satellite. Cryosat-2 has a return period of 369 days, which means the time resolution of a square kilometer ice surface varies between once a year and every 2-3 months depending on how far north you look.

2.2 CryoSat-2 data

We use CryoSat-2 level_1B Baseline_D radar altimetry data from 2010 to 2021. The radar waveforms are processed using the approach of Helm et al. (2014). This includes applying a Threshold First Maximum Retracker Algorithm (TFMRA) with a low thresh-

Table 1. Locations and elevation over the ellipsoid for each GNSS station.

Station name	Latitude [Decimal degrees]	Longitude [Decimal degrees]	Elevation [m]
GLS1	66.47939	-46.31015	2148.64
GLS2	69.09209	-39.64698	2914.22
GLS3	77.43169	-51.10805	2480.24

old (0.25) for Low Resolution Mode (LRM) CryoSat-2 data. This also includes applying a relocation slope correction to estimate the Point-Of-Closest-Approach (POCA). Description of data processing and potential bias due to penetration of radar signals is discussed in Khan et al. (2022).

3 Method

3.1 Ice surface elevation from GNSS data

We process the GNSS data using two different methods and combine the outputs to get the ice surface elevation over the ellipsoid, hereinafter referred to as ice surface elevation. The ice surface elevation is calculated by subtracting the RH from the elevation of the 3D antenna position (see fig. 2 and eq. 1)

$$surface = \mathrm{GNSS}_h - \mathrm{RH} \tag{1}$$

Where surface is the ice surface elevation at the GNSS station, GNSS_h is the elevation of the antenna given by the 3D position (solution from processing method one, see section 3.1.1) converted using the 1980 Geodetic Reference System (GRS80) map coordinate standards and RH is the distance between the ice surface and the antenna (solution from processing method two, see section 3.1.2). Both GNSS_h and RH jump when the GNSS station pole is reset during maintenance visits. These increases are naturally removed from the ice surface elevation time series when the output from the two GNSS processing methods are combined. The corresponding error is calculated using propagation of uncertainties for independent random errors (Taylor, 1996).

3.1.1 Processing method one: GNSS ellipsoidal positions

To estimate the GNSS antenna 3D position, we use the Gipsy X software package version GipsyX-1.7 developed at the Jet Propulsion Laboratory (JPL) and released in December 2019 (Bertiger et al., 2020). We use JPL final orbit products, which include satellite orbits, satellite clock parameters, and Earth orientation parameters. The orbit products take the satellite antenna phase center offsets into account. The atmospheric delay parameters are modeled using the Vienna Mapping Function 1 (VMF1) with VMF1grid nominals (Boehm et al., 2006). Corrections are applied to remove the solid Earth tide and ocean tidal loading. The amplitudes and phases of the main ocean tidal loading terms are calculated using the Automatic Loading Provider (Scherneck, 1999) applied to the FES2014b (Carrere et al., 2016) ocean tide model, including correction for center of mass motion of the Earth due to the ocean tides. The site coordinates are computed in the IGS14 frame (Altamimi et al., 2016). The site coordinates represent GNSS antenna reference point.

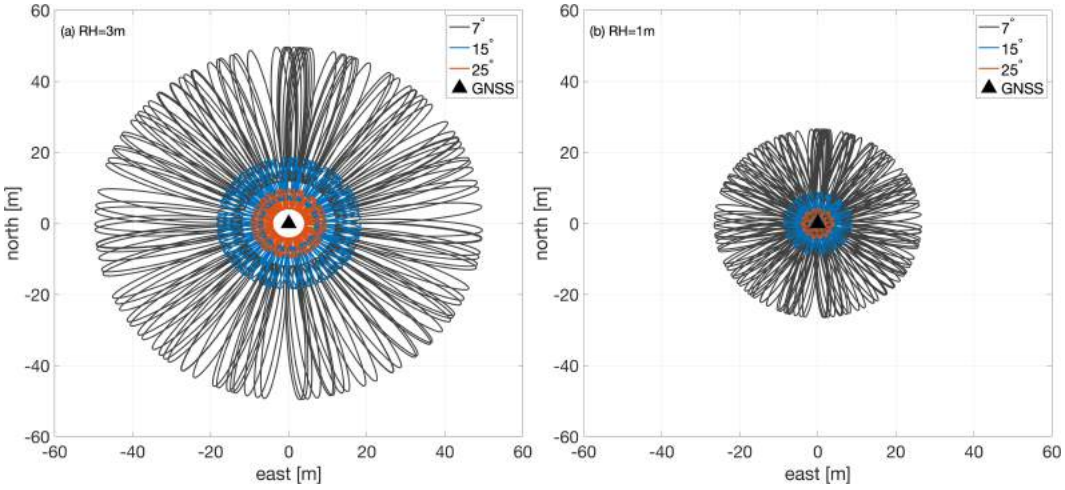

Figure 3. (a) The black triangle indicates a GNSS antenna 3 meter above the surface. The grey, blue and orange lines indicate the GNSS-IR surface footprint with an elevation angle of 7°, 15°and 25°respectively. (b) same as (a) but with a GNSS antenna 1 meter above the surface.

3.1.2 Processing method two: GNSS Reflector height

To estimate RH we use GNSS interferometric reflectometry (GNSS-IR). This technique is driven by geometry and dielectric characteristics of the surface surrounding the GNSS antenna (Roesler & Larson, 2018).

The GNSS-IR software we use is freely available at GitHub (Larson, 2021). We apply the principles described in Roesler and Larson (2018) and Larson et al. (2020) to customise the parameters of our quality control (QC) metrics to make sure only good estimates for the RH are saved. The value of the QC parameters depend on our GNSS data and the station surroundings. Because the GLISN stations are all quite isolated on the ice sheet, we allow isotropic reflectance from all azimuths. The initial a priori range for reflector height is set to be between 0.5 and 8 meters. The elevation angles accepted for processing are set to be between 7°and 25°, giving a surface footprint of up to 50 meter radius when the height of the GNSS antenna above the ice surface is 3 meters (see fig. 3). The peak to noise value, which is the periodogram peak divided by the periodogram noise ratio, is set to 2.7 and the required periodogram amplitude is set for 6 volts at GLS1 and 8 volts for GLS2 and GLS3.

3.2 Satellite elevation time series

We estimate the CryoSat-2 surface elevation time series at a point we call $C(x_0, y_0)$, where x_0, y_0 are east and north coordinates, selecting all available CryoSat-2 data with a maximum distance of 750 m from C and calling them $P(x, y)$. Figure 4 shows CryoSat-2 points (grey points) near GLS1, GLS2, and GLS3. The blue dots denote selected points, P, that are within 750 m of the C (yellow triangle). In order to create a time series at point C, using data at points P, we correct for surface topography. Additionally, all 3 GNSS stations have moved with ice flow during 2011-2020, by up to 292 meters. Consequently, some of the observed changes in elevation are due to stations moving downhill. To correct for surface topography, we use two different approaches. In approach 1, we estimate the surface topography using CryoSat-2 data. In approach 2, we use an existing high-resolution DEM to corrected for surface topography. Approach 1 is similar to Khan et al. (2022) and Csatho et al. (2014). Here, we assume that the surface topog-

Table 2. mean difference between the GNSS and CryoSat-2 surface elevation (surface adjustment), the corresponding standard deviation (STD) and the root-mean-square-difference (RMSD) of the residual between the GNSS and cryosat-2 surface for each GNSS station, using both methods for surface topography correction.

station - method	surface adjustment [m]	STD [m]	RMSD [m]
GLS1 - 1	-3.61	0.41	0.41
GLS1 - 2	-4.60	0.72	0.69
GLS2 - 1	-0.41	0.10	0.11
GLS2 - 2	-0.26	0.17	0.17
GLS3 - 1	0.04	0.08	0.08
GLS3 - 2	0.19	0.12	0.12

raphy does not change during 2011-2020. We use all available CryoSat-2 data within 750 m from C to simultaneously estimate changes in elevation and shape of the surface. We use a 3rd-order polynomial to describe changes in elevation and a 2nd-order polynomial to describe the shape of the surface. In addition, we fit a seasonal term to account for the annual surface changes.

In the vicinity of the GLS1, the most southern GNSS antenna, there are very few CryoSat-2 data (see figure 4a). In addition, the GNSS station moved 292 m during 2011-2020. Both GNSS and CryoSat-2 observations need to be corrected for topography in order to estimate a surface elevation time series at the point C. However, there are almost no CryoSat-2 data close to C, which challenges correction approach 1 of using CryoSat-2 data to estimate a surface topography model. At GLS2, we likewise have very few CryoSat-2 data points. However, the ice velocity is much lower at GLS2. GLS2 moved 80 m during 2011-2020 (see red displacement path in figure 4b). We can therefore horizontally translate C at GLS2 to a nearby position where the CryoSat-2 data coverage is more dense. The true GLS2 position is still within 750 m from the center point the horizontally translated C. GLS3 moved in total 55 m during 2011-2020 and the path is located beneath the center point C (figure 4c). GLS3 is the northernmost station with abundant CryoSat-2 orbits available at the site.

4 Results

4.1 Surface correction approach 1: estimating topography from Cryosat-2 data

Figure 5a,b,c shows the ice surface elevation at GLS1, GLS2 and GLS3, respectively, computed from the GNSS data. The surface elevation computed from CryoSat-2 data is adjusted with the mean difference between the two time series (see table 2) to align them.

The validation of CryoSat-2 surface elevation using correction approach 1 (fig. 5) shows that the satellite captures the ice surface change well. GLS1 (5a,d) has the biggest difference between the GNSS and CryoSat-2 surface, with a residual range between -0.57m and 0.74m. GLS2 (5b,e) has a residual range of -0.21m and 0.18m. GLS3 (5c,f) has the smallest difference between the GNSS and CryoSat-2 surface, with a residual range of -0.12m and 0.11m.

Unfortunately, in part because of the pandemic, the pole has not been extended at any of the GLISN sites since 2018. This means the results from GLS1 and GLS2 can-

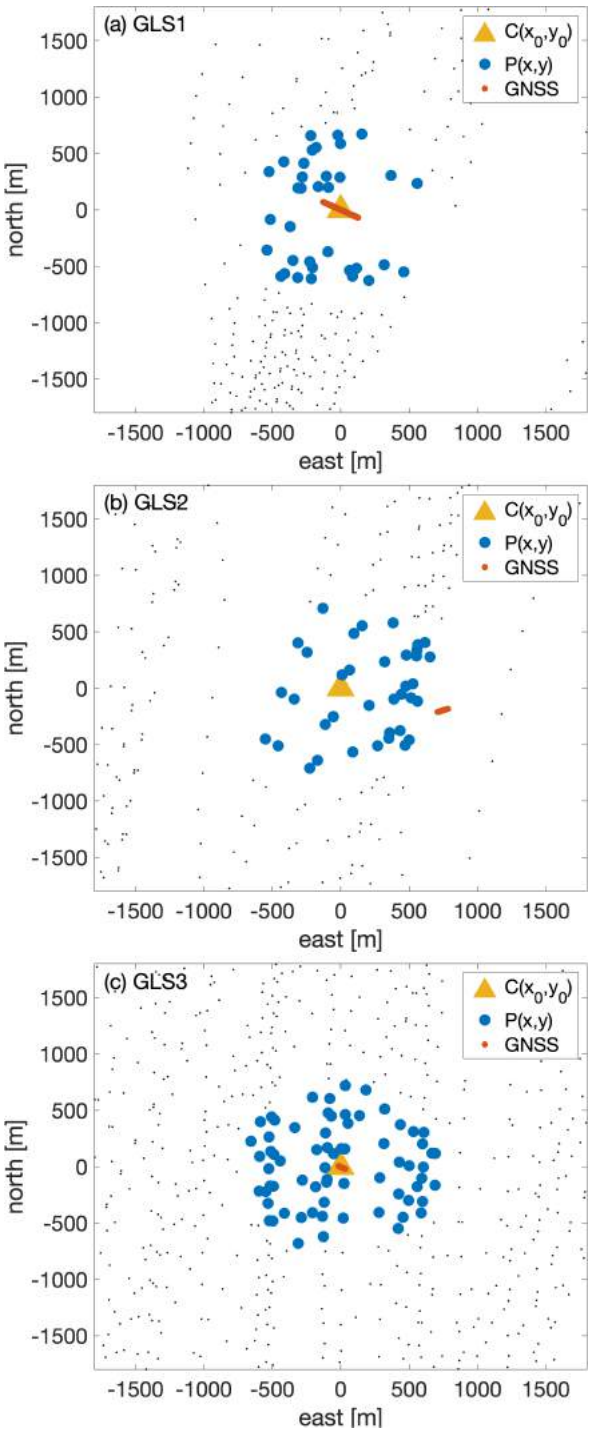

Figure 4. (a) The grey points indicate CryoSat-2 data points near GLS1. The blue dots denote CryoSat-2 points within 750 m from the center point ($C(x_0, y_0)$, yellow triangle). The red points denote the displacement path of the GNSS antenna during the observation period. (b) same as (a) but for GLS2. (c) same as (a) but for GLS3.

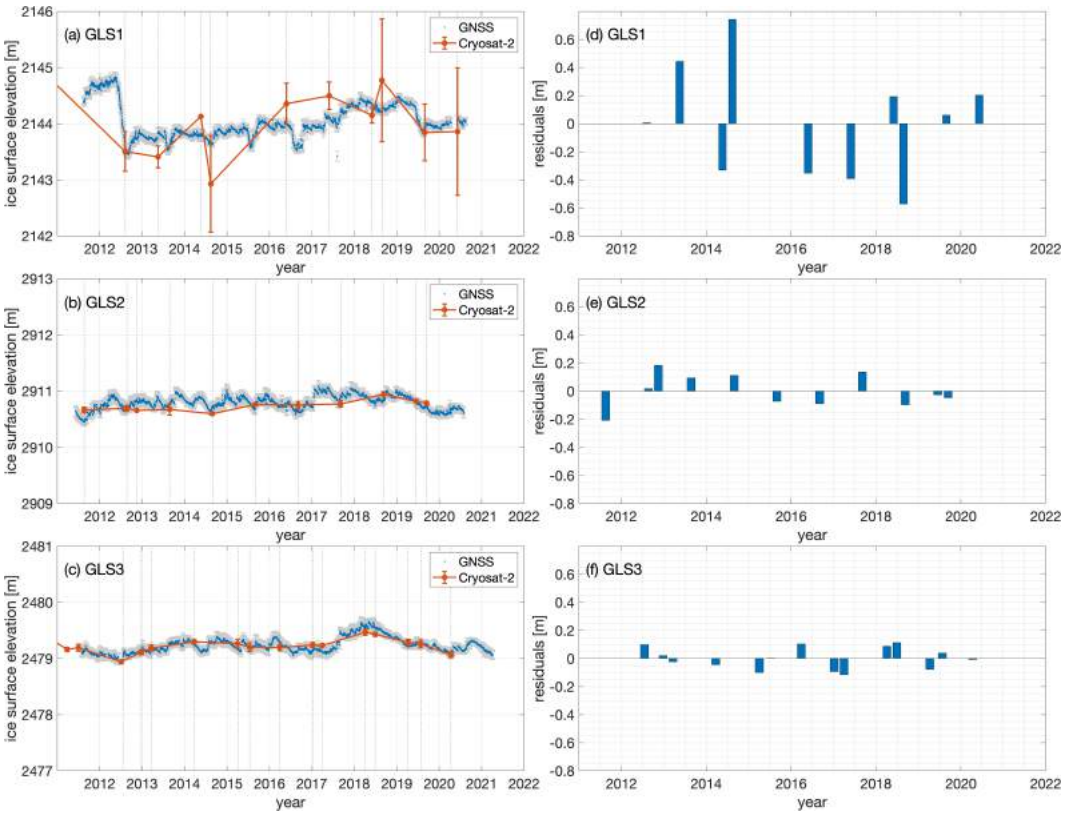

Figure 5. **(a)** Ice surface elevation computed from GNSS and CryoSat-2 data at GLS1 using correction approach 1. The vertical dotted lines indicate the dates with a result from both GNSS and Cryosat-2. **(b)** same as **(a)** for GLS2. **(c)** same as **(a)** for GLS3. **(d)** residuals between GNSS ice surface elevation change and CryoSat-2 surface elevation change at GLS1. **(e)** same as **(d)** for GLS2. **(f)** same as **(d)** for GLS3.

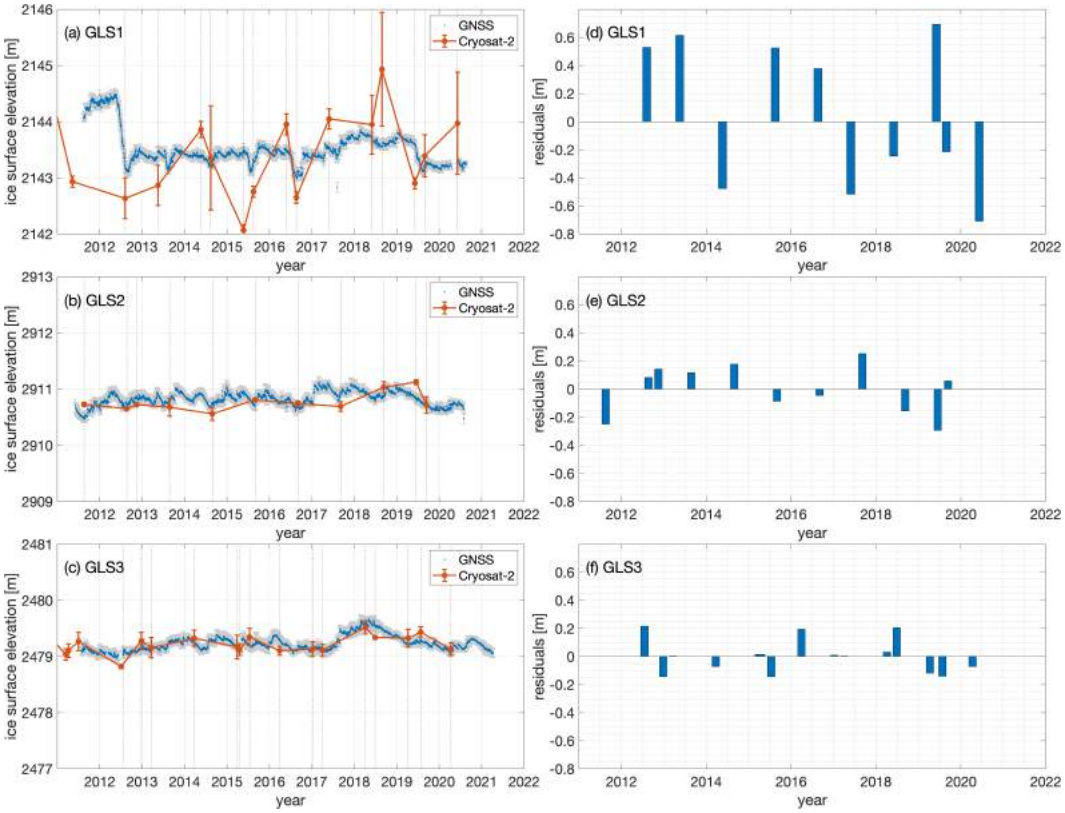

Figure 6. **(a)** Ice surface elevation computed from GNSS and CryoSat-2 data at GLS1 using correction approach 2. The vertical dotted lines indicate the dates with a result from both GNSS and Cryosat-2. **(b)** same as **(a)** for GLS2. **(c)** same as **(a)** for GLS3. **(d)** residuals between GNSS ice surface elevation change and CryoSat-2 surface elevation change at GLS1. **(e)** same as **(d)** for GLS2. **(f)** same as **(d)** for GLS3.

not be used after summer 2020, as the GNSS-IR method is not able to resolve reflector heights below approximately 0.5m ((Larson, 2021), README.md).

4.2 Surface correction approach 2: topography from existing DEM

Figure 6 is identical to figure 5 except the surface is corrected using approach 2. In comparison to the correction approach where the surface topography is estimated from cryosat-2 data, the correction approach where the surface topography is from an existing DEM increases the residual range at all three GNSS sites. The performance rank, however, remains the same with the surface elevation change derived from CryoSat-2 radar altimetry performing the best at GLS3 and worst at GLS1. GLS1 (fig. 6a,d) has a residual range of -0.71m and 0.69m. GLS2 (fig. 6b,e) has a residual range of -0.29m and 0.25m. GLS3 (fig. 6c,f) has a residual range of -0.14m and 0.21m.

5 Discussion

When visually comparing correction approach 1 (fig. 5) and correction approach 2 (fig. 6), it is apparent the surface elevation change derived from CryoSat-2 radar altimetry data performs fairly well when it comes to capturing surface changes over a longer period of time, independent of the surface correction approach used. However, looking

at the surface residual range and the corresponding RMSD (table 2) it is clear the correction approach where topography is estimated outperforms the correction approach where a DEM is used for topography, as the residual ranges and the RMSD are smaller at all three GNSS sites. We acknowledge this is only the case because the GNSS site areas are relatively small, making the simple topography estimation valid, and because DEMs are associated with high uncertainty on the interior of the GrIS, due to the large distances to the nearest ground control points. Were we, however, to go to the three sites and make local high resolution DEMs of each area using a similar set-up to Brunt et al. (2017) the correction approach where a DEM is used for topography would be expected to outperform the simple topography estimation.

Making a comparison between residual range of the three GNSS sites (fig. 5d,e,f) clearly shows the surface elevation change derived from CryoSat-2 radar altimetry data does not perform equally over the GrIS, as both residual range and RMSD values change between sites. At GLS3 (fig. 5c,f) the Cryosat-2 derived surface change perform significantly better than at GLS1 (fig. 5a,d) and slightly better than at GLS2 (fig. 5b,e). Larson et al. (2020) validated the RH from GLS1 against two independent in situ snow accumulation sensors, confirming the reason for the difference in performance does not originate from GNSS error. The reason for the performance variations can be attributed to differences in local conditions and Cryosat-2 data availability from site to site. The amount of CryoSat-2 data points are roughly doubled from GLS1 and GLS2 to GLS3, and there are an uneven spread of data points at GLS1 and GLS2, where at least 2/3 of the CryoSat-2 data points are located at one side of the station (fig. 4). Furthermore, the local slope of the GrIS varies significantly from GLS1 to GLS2 and GLS3 (see fig. 7), which is also reflected in the variation in distance each station move. The GNSS station moving the shortest distance during 2011-2020 and the station on the flattest slope is GLS3, which only moved 55m. In comparison, GLS1 stands on a steeper slope and moved more than 5 times that distance in the same amount of time. Because GLS2 shares characteristics with both GLS1 and GLS3 and has a residual range between the two it helps us understand the relative importance between data availability and the local conditions. The residual range of GLS2 is closer to the residual range of GLS3 than GLS1, indicating the characteristic they share is more important for the performance of the surface elevation change derived from CryoSat-2 than the characteristic GLS2 share with GLS1. GLS2 moves less than 3m yr^{-1} more than GLS3 and their surface slope is roughly the same, therefore we can assume the precision of the surface correction to point C is more important for the performance than data availability. Had the surface correction been precise, such as it would be if local high resolution DEMs were made, as suggested above, the performance at GLS1 would roughly be the same as the performance at GLS2, as the data would be better corrected for the steepness of the slope when using the DEM topography correction approach. However, GLS3 would still perform better than the other sites due to Cryosat-2 data availability.

One of the big advantages when assessing satellite altimetry data with permanent GNSS stations is the continuous data series with a daily time resolution. The GNSS surface elevation time series (fig. 5a,b,c) clearly show an extreme drop in surface elevation at GLS1 in the summer of 2012, which is not as profound at they other stations. Likewise, are there a raise in surface elevation at GLS3 through the wither of 2017-2018, which keep raising after the surface elevation start lowering again at the other stations. Other studies makes assessments based on data that only capture part of the changes to the GrIS as they either have a short data series with a high time resolution (e.g., Stokholm et al., 2021), a long data series composed of repeated short data series with a high time resolution (e.g., Brunt et al., 2017) or a longer data series where the time resolution depends on the frequency of Operation IceBridge overflights (e.g., McMillan et al., 2018). The studies mentioned above are great for evaluating the performance at a specific moment in time or for validating the capture of long-term changes to the GrIS. However, as our GNSS derived ice surface elevation time series (fig. 5a,b,c) show, extreme short-

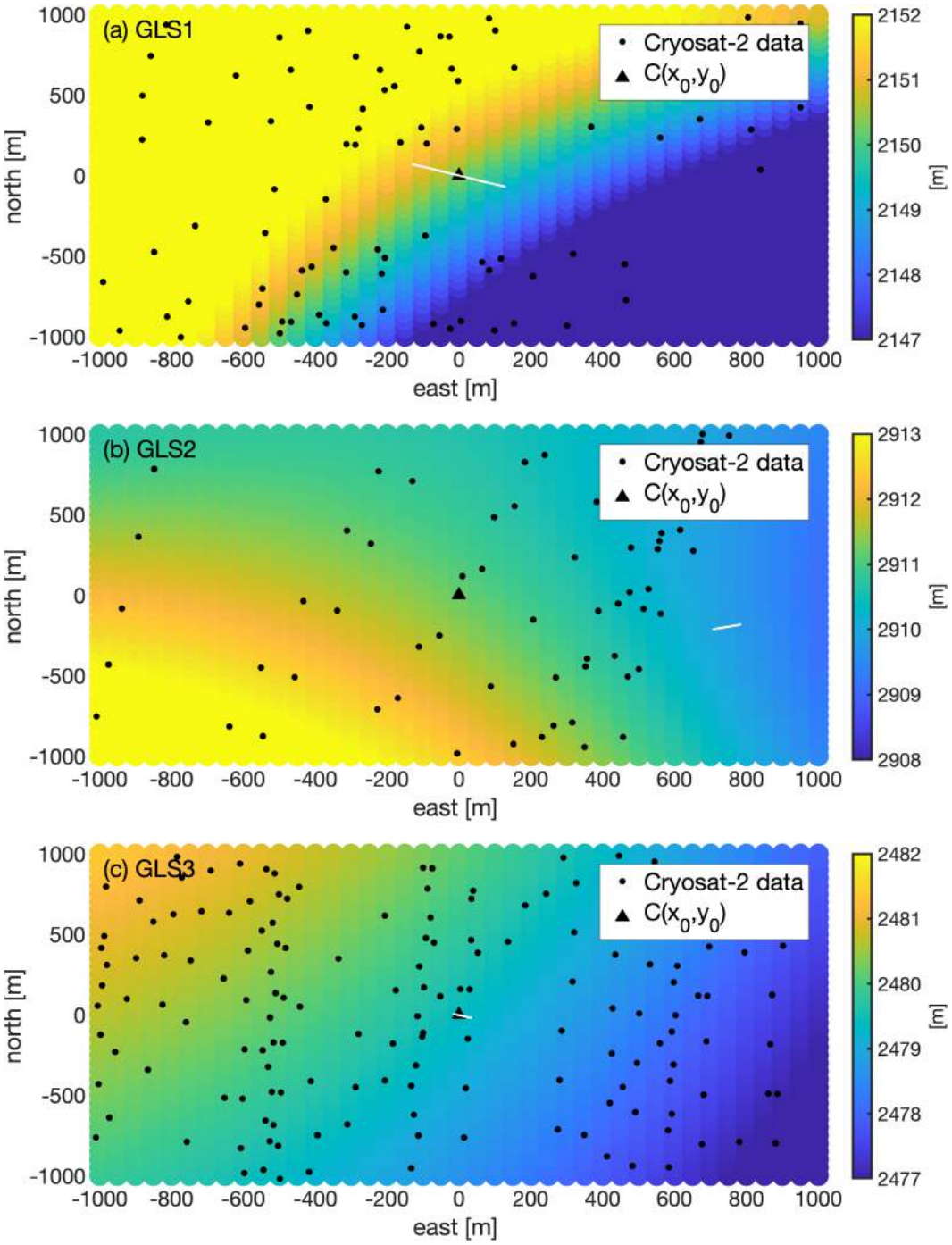

Figure 7. (a) Estimated ice surface topography using CryoSat-2 data (referred to as approach 1 in section 3.2). The black triangle indicates the point $C(x_0, y_0)$, the white points indicate the displacement path of the GNSS antenna during the observation period and The black dots indicate data points from cryosat-2. (b) same as (a) for GLS2. (c) same as (a) for GLS3.

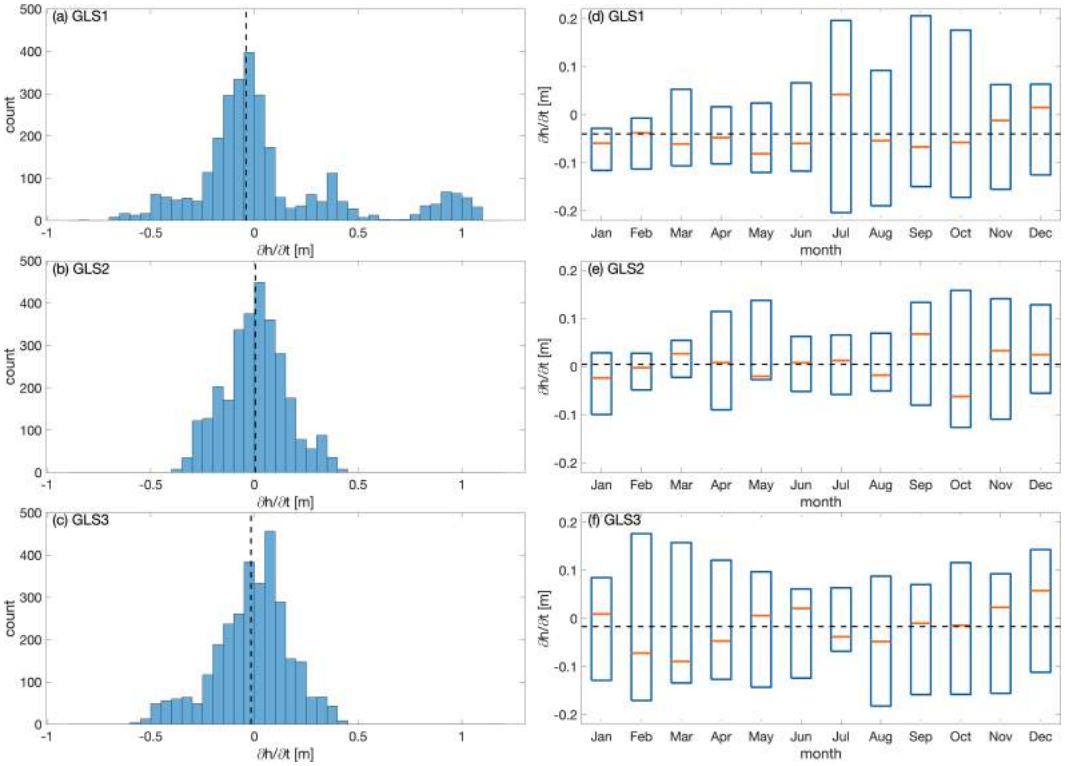

Figure 8. **(a)** histogram of all yearly elevation change measurements calculated from the GLS1 ice surface elevation time series. **(b)** same as **(a)** for GLS2. **(c)** same as **(a)** for GLS3. **(d)** The boxplot is made from the monthly average of the yearly ice GLS1 surface elevation change from 01-01-2012 to 31-12-2019. The central mark (orange) indicates the median. The bottom and top edges of the box indicate the 25th and 75th percentiles. The whiskers and outliers are not plotted. **(e)** same as **(d)** for GLS2. **(f)** same as **(d)** for GLS3. **(a-f)** the dashed black line indicate the mean of the monthly median.

term changes occur and it is therefore important to assess the satellite data against a data series that also captures these changes as they otherwise might be perceived as errors or outliers in the satellite data. Another big advantage to this assessment method is the cost efficiency compared to other methods. If a GNSS station is installed with respect to the local conditions, eg. accumulation rate, it is only necessary to visit the station for maintenance once every 2-4 years, keeping the maintenance cost low after the initial installation as it saves labor-hours and other travel expenses. The initial Installation will, however, be expensive, especially if a local DEM is made, as suggested above, but this will quickly equal out when compared to the cost of yearly airplane charter or traverse expeditions.

Calculating the yearly elevation change (∂H/∂t) for every possible date pair in the GNSS ice surface elevation time series (fig. 8a,b,c) clearly shows a big variation in ∂H/∂t. Figure 8(d,e,f) shows the monthly ∂H/∂t changes a lot for all three GNSS stations throughout the year, making it clear that yearly elevation change products from airborne and satellite altimetry might not be an accurate representation of changes to the surface elevation as the absolute value and sign of elevation change varies from month to month. For all three GNSS stations we see a median lower than the yearly average in August and higher than the yearly average in November and December, which indicate a yearly elevation change campaign performed from August to August would give a misleading

high elevation change whereas the same campaign in November or December would give a misleading low elevation change. Evaluating the proximity of the monthly median and the yearly average for all three GNSS stations suggests April would be the best month to conduct an ice sheet wide yearly elevation change campaign.

6 Conclusions

We have presented a comparison between CryoSat-2 radar altimetry and three continuous GNSS data series at different locations on the interior of the GrIS to assess how well CryoSat-2 radar altimetry captures both short- and long-term changes in ice sheet elevation. Results show a variation in performance based on local conditions and satellite data availability, with the best performance at the location with the flattest surface and the highest data density. However, the other sites provide valuable information to the relative importance of local conditions and data availability, which gives us inside into what initial local surveys should be made and where future stations should be placed to get the optimal results. This suggests that a network of on ice GNSS stations should be established, preferably across the interior of the GrIS but especially on the northern part of the ice sheet where the density of satellite data is higher. Such a network would provide the best opportunity for validation of future airborne altimetry data, a highly precise reference for combining different airborne altimetry data sets and present opportunity for ice sheet ground control points, which could be used for DEM construction and reduce the high uncertainty they are associated with far from the edges. Over time it would be much more cost efficient to maintain permanent GNSS stations than having yearly survey campaigns. Furthermore, we have used the continues ice surface elevation derived from GNSS data to calculate the yearly elevation change throughout the year and found big monthly variation suggesting April is the best month to do an ice sheet wide yearly elevation change campaign.

Data Availability Statement

GNSS data from GLS1, GLS2 and GLS3

The GNSS data used in this study for both GNSS processing methods are Rinex2 data files downloaded form UNAVCO.org. The datasets are found under GPS/GNSS Obersvations Dataset. The three stations have individual DOIs GLS1: https://doi.org/10.7283/T5WS8RDB, GLS2: https://doi.org/10.7283/T5S46Q3N and GLS3: https://doi.org/10.7283/T5NC5ZCX. The data is freely available with no registration requirements. To facilitate data citation UNAVCO provide Digitial Object Identifier (DOI) assignments for all suitably-archived, publishable datasets (including GPS/GNSS, TLS, and SAR data and products). Furtheremore, UNAVCO writes "a citation using a dataset's DOI in a publication's reference list provides appropriate attribution".

GNSS-IR

The GNSS-IR python software used in this study was developed by Kristine Marie Larson and is freely available at github (https://github.com/kristinemlarson/gnssrefl/tree/1.0.10) The current github version is 1.1.3 and the version used for this study is 0.0.59. The DOI applicable to all versions is 10.5281/zenodo.5601495. Besides for the DOI nothing is mentioned about how the software should be cited.

Cryosat-2 data

CryoSat data is freely and openly available to everyone. Access is provided to all CryoSat systematic data acquired according to the current geographical mode mask. The DOI for the European Space Agency, 2019, L1b LRM Precise Orbit, Baseline D is https://doi.org/10.5270/CR2-

cbow23i. The access and use of CryoSat products are regulated by the ESA's Data Policy and subject to the acceptance of the specific Terms & Conditions Users accessing CryoSat products are intrinsically acknowledging and accepting the terms and conditions.

Acknowledgments

S A Khan acknowledge support from the Independent Research Fund Denmark- Natural Sciences Grant No. 1026-00085B and Villum Fonden (Villum Experiment Programme) Project No. 40718. We acknowledge the National Snow and Ice Data Center QGreenland package. We thank the European Space Agency for providing the CryoSat-2 data.

References

Altamimi, Z., Rebischung, P., Métivier, L., & Collilieux, X. (2016). Itrf2014: A new release of the international terrestrial reference frame modeling nonlinear station motions. *Journal of Geophysical Research: Solid Earth*, *121*(8), 6109–6131.

Bertiger, W., Bar-Sever, Y., Dorsey, A., Haines, B., Harvey, N., Hemberger, D., ... others (2020). Gipsyx/rtgx, a new tool set for space geodetic operations and research [software]. *arXiv preprint arXiv:2004.13124*.

Boehm, J., Werl, B., & Schuh, H. (2006). Troposphere mapping functions for gps and very long baseline interferometry from european centre for medium-range weather forecasts operational analysis data. *Journal of geophysical research: solid earth*, *111*(B2).

Brunt, K. M., Hawley, R. L., Lutz, E. R., Studinger, M., Sonntag, J. G., Hofton, M. A., ... Neumann, T. A. (2017). Assessment of nasa airborne laser altimetry data using ground-based gps data near summit station, greenland. *The Cryosphere*, *11*(2), 681–692.

Carrere, L., Lyard, F., Cancet, M., Guillot, A., Picot, N., et al. (2016). Fes 2014, a new tidal model—validation results and perspectives for improvements. In *Proceedings of the esa living planet symposium* (pp. 9–13).

Clinton, J. F., Nettles, M., Walter, F., Anderson, K., Dahl-Jensen, T., Giardini, D., ... others (2014). Seismic network in greenland monitors earth and ice system. *Eos, Transactions American Geophysical Union*, *95*(2), 13–14.

Csatho, B. M., Schenk, A. F., van der Veen, C. J., Babonis, G., Duncan, K., Rezvanbehbahani, S., ... Van Angelen, J. H. (2014). Laser altimetry reveals complex pattern of greenland ice sheet dynamics. *Proceedings of the National Academy of Sciences*, *111*(52), 18478–18483.

Detrick, R., & Anderson, K. (2011a). *Arctic pi continuous - gls1-glisn 1 p.s., unavco, gps/gnss observations dataset* [dataset]. UNAVCO, Inc. Retrieved from `https://www.unavco.org/data/gps-gnss/data-access-methods/dai1/select_data.php?code=GLS1&gid=3138&ds=2&parent_link=Permanent&pview=original&filter_data_availability=checked&from_date=2011-08-13&to_date=2021-06-30` doi: https://doi.org/10.7283/T5WS8RDB

Detrick, R., & Anderson, K. (2011b). *Arctic pi continuous - gls3-glisn 3 p.s., unavco, gps/gnss observations dataset* [dataset]. UNAVCO, Inc. Retrieved from `https://www.unavco.org/data/gps-gnss/data-access-methods/dai1/select_data.php?code=GLS3&gid=2995&ds=13&parent_link=Permanent&pview=original&filter_data_availability=checked&from_date=2011-07-21&to_date=2022-05-18` doi: https://doi.org/10.7283/T5NC5ZCX

Detrick, R., & Anderson, K. (2012). *Arctic pi continuous - gls2-glisn 2 p.s., unavco, gps/gnss observations dataset* [dataset]. UNAVCO, Inc. Retrieved from `https://www.unavco.org/data/gps-gnss/data-access-methods/dai1/select_data.php?code=GLS2&gid=3138&ds=3&parent_link=Permanent&pview=original&filter_data_availability=checked&from_date=2011-06-07&to_date=2021-09-10` doi: https://doi.org/10.7283/T5S46Q3N

Helm, V., Humbert, A., & Miller, H. (2014). Elevation and elevation change of greenland and antarctica derived from cryosat-2. *The Cryosphere*, *8*(4), 1539–1559.

Khan, S. A., Bamber, J. L., Rignot, E., Helm, V., Aschwanden, A., Holland, D. M., ... others (2022). Greenland mass trends from airborne and satellite altimetry during 2011-2020. *Journal of Geophysical Research: Earth Surface*, e2021JF006505.

Larson, K. M. (2021). *Gnss reflections code* [software]. Retrieved 2021-02-30,

from `https://github.com/kristinemlarson/gnssrefl` doi: 10.5281/zenodo.5601495

Larson, K. M., MacFerrin, M., & Nylen, T. (2020). Brief communication: Update on the gps reflection technique for measuring snow accumulation in greenland. *The Cryosphere*, *14*(6), 1985–1988.

Larson, K. M., Wahr, J., & Munneke, P. K. (2015). Constraints on snow accumulation and firn density in greenland using gps receivers. *Journal of Glaciology*, *61*(225), 101–114.

McMillan, M., Shepherd, A., Muir, A., Gaudelli, J., Hogg, A. E., & Cullen, R. (2018). Assessment of cryosat-2 interferometric and non-interferometric sar altimetry over ice sheets. *Advances in Space Research*, *62*(6), 1281–1291.

Moon, T., Fisher, M., Simonoko, H., & Stafford, T. (2021, March). *Qgreenland* [software]. Zenodo. Retrieved from `https://doi.org/10.5281/zenodo.6369184` (If you use this software, please cite it as below.) doi: 10.5281/zenodo.6369184

Nilsson, J., Vallelonga, P., Simonsen, S. B., Sørensen, L. S., Forsberg, R., Dahl-Jensen, D., ... others (2015). Greenland 2012 melt event effects on cryosat-2 radar altimetry. *Geophysical Research Letters*, *42*(10), 3919–3926.

Roesler, C., & Larson, K. M. (2018). Software tools for gnss interferometric reflectometry (gnss-ir). *GPS solutions*, *22*(3), 1–10.

Scherneck, H.-G. (1999). *Welcome to the free ocean tide loading provider* [dataset]. Retrieved 2021-06-30, from `http://holt.oso.chalmers.se/loading/`

Stokholm, A., Hvidegaard, S. M., Forsberg, R., & Simonsen, S. B. (2021). Validation of airborne and satellite altimetry data by arctic truck citizen science. *GEUS Bulletin*, *47*.

Taylor, J. R. (1996). *An introduction to error analysis: The study of uncertainties in physical measurements* (2Sub ed.). University Science Books.

Appendix C

Paper III

Terrain corrected snow thickness from GNSS-IR at Station Nord

Karina Hansen[1], Trine S. Dahl-Jensen[1], and Lars Stenseng[1]

[1]DTU Space, Technical University of Denmark, Kongens Lyngby, 2800, Denmark

August 31, 2022

Abstract

we used data from the GNET station NORD to demonstrate GNSS-IR can be used to derive terrain corrected snow thickness on Greenland bedrock. We identified snow free time periods and used the GNSS-IR results to estimate a 360° summer surface topography profile, which we then used as a reference for estimating snow thickness. We found the snow thickness generally increased throughout winter, where the snow surface builds up to an approximately flat surface despite bedrock topography, which results in big differences in snow thickness. Furthermore, we found the distinct pattern of the average snow thickness time series can be used to identify the onset of melt, which was validated by by a nearby weather station, that showed the date for onset of melt found using GNSS-IR correspond to the first long time period with an average temperature above 0°C.

1 Introduction

Due to the extensive length of the Greenland coastline many areas goes unvisited for most of the year and the knowledge of snow build-up and melt in these areas are limited and often dependent on model output. There are several types of remote sensing instruments installed along the coastline, one of which is a network of Global Navigation Satellite System (GNSS) stations, also known as the Greenland GNSS Network (GNET, see fig. 1a). GNET stations are both placed in towns and secluded, making them ideal for providing information on secluses areas. For many years the only information derived from GNSS data was position, But within the last decade a new processing method, called GNSS interferometric reflectometry (GNSS-IR), has been developed. GNSS-IR derives the vertical distance between a GNSS antenna and the surrounding surface, often referred to as the Reflector Height (RH, 1b). Until now GNSS-IR

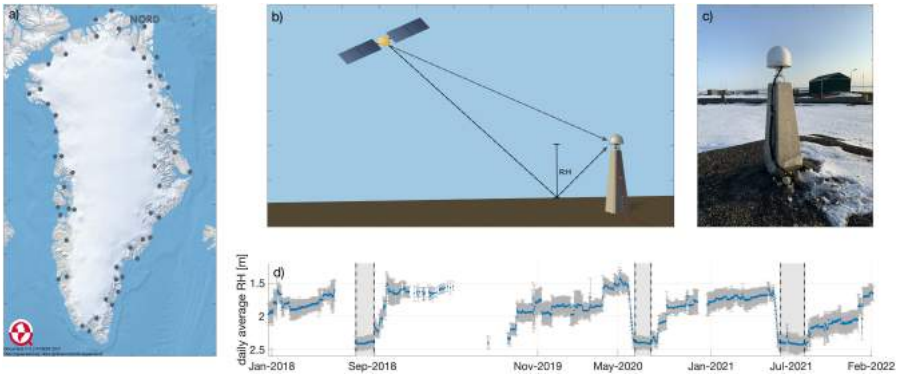

Figure 1: a) Overview of GNET station positions on a background map from Qgreenland (Moon et al., 2021). b) Illustration of the GNSS-IR observation method. c) picture of the GNET station NORD on the 22^{nd} of August 2019. d) Daily average RH from the gnssrefl software where the light grey boxes with black dashed sides lines indicate the three summer time periods used to derive the summer surface. Note that the y axis has been inverted to provide a visual intuitive interpretation.

has been used to study changes in RH of smooth surfaces eg. fields, ice caps and water (Roesler and Larson, 2018; Larson et al., 2020), because smooth surfaces increase the precision of the result. In this study we show the method can also be applied to surfaces with more topography, making it possible to derive snow thickness and melt season at GNET stations.

2 data

The majority of the GNET GPS station infrastructure was established during the fourth International Polar Year 2007-2008, and the infrastructure has since been extended and upgraded. Today the GNET is capable of observing not only GPS but all the GNSS constellations, and selected stations further support real-time streaming of observations. In this study we use data from the GNET station installed at Station Nord (NORD, see fig. 1a,c). Although data from NORD is available since 2006, we focus on the years from 2018 and onward, as an upgrade to multiple GNSS constellations, in the summer of 2017, improved the RH results significantly.

3 Method

3.1 GNSS interferometric reflectometry

In contrast to the normal GNSS processing methods, the observable in GNSS-IR is not the pseudorange but rather interference patterns on the signal from a given GNSS satellite. The RH is derived from variations in multipath, which are a result of the interference between a direct satellite signal and a satellite reflected of the earth surface (see fig. 1b). When the GNSS satellite moves across the sky, the relative path length between the direct and the reflected signal changes in a periodical way which causes an oscillation between constructive and destructive interference in the received multipath signal. The GNSS-IR software used in this study (gnssrefl, Larson (2021)) use Signal-to-noise ratio (SNR) data to estimate the RH based on the theoretical knowledge of what a multipath frequency should be provided by Georgiadou and Kleusberg (1988) and a change in variables concept proposed by Axelrad et al. (2005), which yields one multipath frequency per rising or setting satellite arc, with a simple $f = 2\mathbf{RH}/\lambda$ relationship between the multipath frequency (f) and the RH (Roesler and Larson, 2018; Larson et al., 2020).

3.2 Snow thickness referenced to the summer surface

The local topography of the bedrock surrounding the GNET stations is variable and height changes observed at different azimuths can therefore not be averaged without additional processing. The daily average from the gnssrefl software might create false snow thickness tendencies, as a snow surface might create reflections from azimuth angles, where there are normally no reflected satellite signal. To prevent this we calculate the daily snow thickness with respect to the summer surface for each azimuth angle and average the results. The summer surface is derived from a three step process: The first step is to identify the time periods where the surface surrounding the GNSS station is bare. At NORD the difference between the summer and winter surface is significant, thus making it possible to identify bare surface periods from the daily average provided by gnssrefl. Figure 1d shows the gnssrefl daily average RH from NORD, where the contrast between the thick snow layers (low RH) and the bare surface (large RH) is significant. The melt season is identified as the time period where RH increase rapidly over a course of a couple of weeks. The following time period, where the changes to the average RH are very small, is the bare surface period, from which the data can be used to create a summer surface. The second step is to combine all the available data points from bare surface results and remove outliers. Gross outliers are removed from boundaries chosen by visible evaluation of the all bare surface RH results (see fig. 2a). Here we set the lower cut off point at 1.88 m and the upper cut off point at 2.77 m. The remaining outliers are removed by fitting a third order polynomial to the data and removing all data points more than 3 standard deviation from the fitted line (see fig. 2b). The third order polynomial is chosen to accommodate variations in surface elevation around the

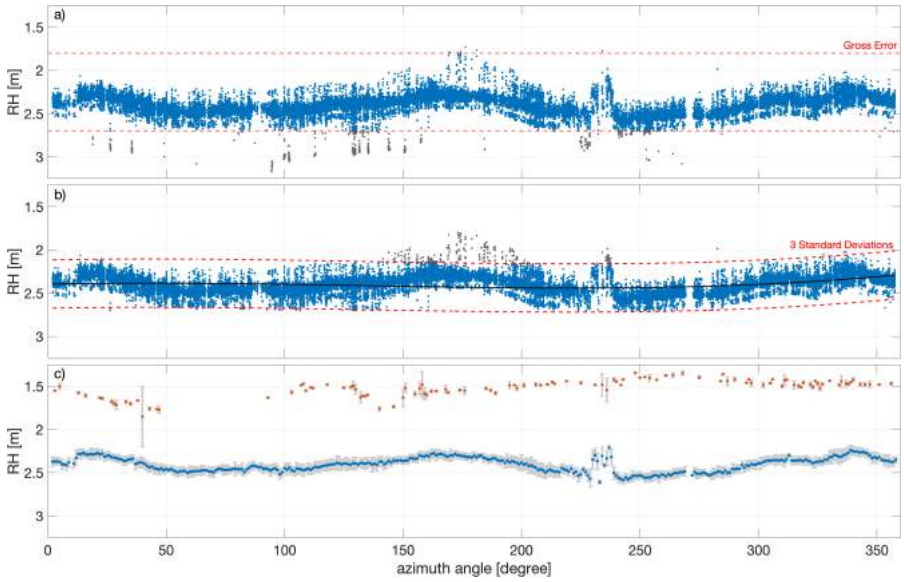

Figure 2: a) Gross outlier removal from all RH data points collected during the three summer time periods marked on fig. 1d. The grey dots mark the data points exceeding the gross error boundaries (red dashed lines) and the blue dots mark the data used in next step. b) Outlier removal 3 standard deviations from a third order polynomial fit to the remaining data points. The grey dots mark the data points exceeding the 3 standard deviations (red dashed lines) and the blue dots mark the data points who fall within the boundaries. c) The blue dots show summer surface derived from remaining data points after the two rounds of outlier removal and the orange dots are the RH result from the 16^{th} of June 2020.

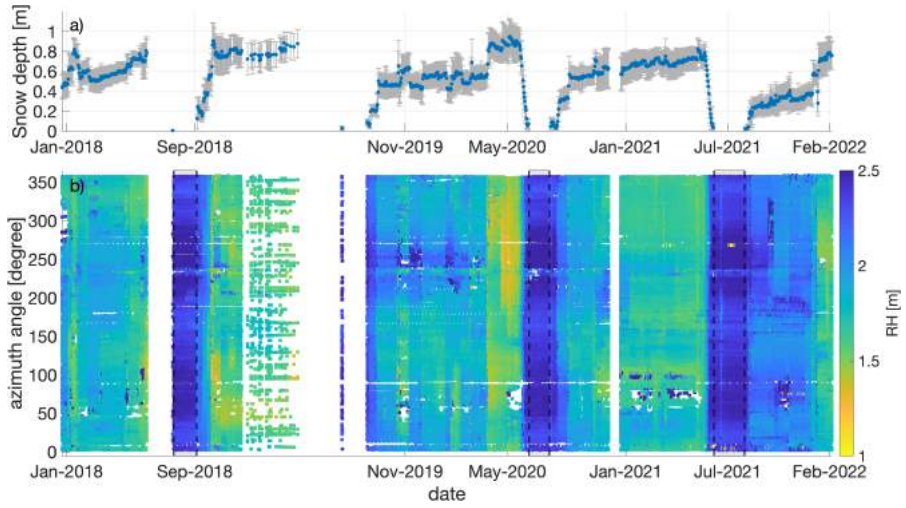

Figure 3: a) Time series of the daily average snow thickness with respect to the summer surface seen in figure 2c. b) Time series of the RH of every available azimuth angle.

GNSS station without the risk of overfitting. The third and final step is to find the mean RH for each azimuth angle and the corresponding standard deviation (see fig. 2c).

4 Results and Discussions

4.1 Snow thickness

The maximum average snow thickness between 2018 and 2022 is found on the 29^{th} of May 2020 where the average snow thickness was 0.95 $\pm$0.17 m. On the same day the minimum snow thickness was 0.47 m and maximum 1.29 m, which is a difference of approximately 80 cm on the same day within a relatively small area, explaining the relatively high uncertainty seen in figure 3a. Figure 2c shows the derived summer surface and the RH of the snow surface on the 16^{th} June 2020. Comparing the surface shapes of the two it becomes apparent the snow build-up is not uniform over the surface, as the snow thickness increases. This is specially visible between azimuth 150 and 360, where the summer surface shows topographic variation and the snow surface smooth out the variations. Although a large snow thickness generally means the snow has build-up to a smooth surface there are still variations in RH. An example of this can be seen in spring of 2020 where the April maximum snow thickness is found in the azimuth interval [50:100] and the May maximum snow interval is found in the azimuth interval [200:300] (fig. 3b). Looking at the changes in snow thickness over time it is clear the snow layer generally gets thicker throughout winter, as

expected, often sustaining close to the yearly maximum until the unset of melt (see fig. 3a).

4.2 Unset of melt

As mentioned in the method section, it is easy to identify the unset of melt at NORD, because of the abrupt and significant change in average RH between winter and summer. This is further enhanced by the difference between the snow build and melt season patterns. Although the snow thickness generally increase throughout wither, there are also plenty examples of small decrease both visible as jumps and a steady decrease (fig. 3a). In contrast to the smaller winter decreases in snow thickness, the unset of melt introduce a rapid decrease, which is simply to extreme to be a storm blowing snow away or the snow compacting under its own weight. In 2020 the unset of melt is on the 16^{th} of June and in 2021 it is on the 15^{th} of June. The unset of melt at NORD can not be determined in 2018 and 2019 due to missing data.

5 Validation

Figure 4a shows that snowfall in Greenland is often accommodated by strong winds, which often make snow thickness approximations from precipitation data incorrect, as strong winds are just as likely to blow snow away from the surface as to deposit it. Weather data can however be used to indicate whether GNSS-IR snow thickness measurements can be trusted and if we identified the unset of melt correctly. Looking at figure 4 there are three things that indicate the GNSS-IR derived snow thickness can be trusted. The first, snow build-up only happens when the temperature is below 0°C. The second, strong winds and/or precipitation is present every time the snow thickness increase. The third, during shorter periods with stable calm weather the snow thickness remain the same. Validating the melt is easier, because melt is largely Temperature dependent. Slight melt should appear whenever the temperature reach 0°C, which is hard to validate due to the large spread in daily RH across the different azimuth. The unset of the melt season however, should correlate with the first longer time period where the temperature is consistently above 0 °C. The dotted grey line seen in 4a,b marks the unset of melt from the temperature profile, which fall on the same day as the unset of melt from GNSS-IR.

References

P. Axelrad, K. Larson, and B. Jones. Use of the correct satellite repeat period to characterize and reduce site-specific multipath errors. In *Proceedings of the 18th International Technical Meeting of the Satellite Division of The Institute of Navigation (ION GNSS 2005)*, pages 2638–2648, 2005.

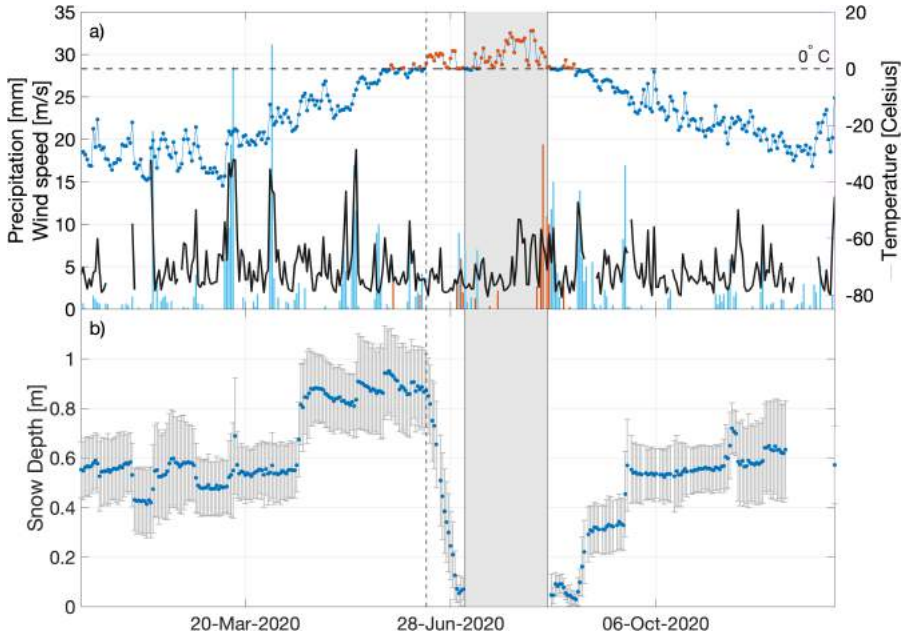

Figure 4: The light grey box indicate the time period used the estimate the summer surface. a) Weather station data from Station Nord provided by the danish meteorological institute online weather archive. The horizontal dashed black line mark 0°C. The full black line indicate the daily mean wind speed. The blue and orange bars both show daily precipitation, the orange colour indicate the precipitation on days with an average temperature of more than 0°C. The blue and orange both show daily average temperature, the orange colour indicate an average temperature of more than 0°C. Both average wind speed and precipitation are referenced to the left y-axis, whereas temperature is referenced to the right y-axis b) The daily snow thickness with respect to the derived summer surface. The vertical dashed line visible in both a) and b) marks the start of the melt season, with a longer time period where the average temperature is above 0°C and the light grey box marks the bare surface period.

Y. Georgiadou and A. Kleusberg. On carrier signal multipath effects in relative gps positioning. *Manuscripta geodaetica*, 13(3):172–179, 1988.

K. M. Larson. Gnss reflections code, 2021. URL `https://github.com/kristinemlarson/gnssrefl`.

K. M. Larson, M. MacFerrin, and T. Nylen. Brief communication: Update on the gps reflection technique for measuring snow accumulation in greenland. *The Cryosphere*, 14(6):1985–1988, 2020.

T. Moon, M. Fisher, H. Simonoko, and T. Stafford. Qgreenland, Mar. 2021. URL `https://doi.org/10.5281/zenodo.6369184`.

C. Roesler and K. M. Larson. Software tools for gnss interferometric reflectometry (gnss-ir). *GPS solutions*, 22(3):1–10, 2018.

Denne PhD afhandling består af tre artikler der bruger GPS-data til at undersøge forskellige aspekter Grønland og Indlandsisen. I starten af dette årtusinde blev et netværk af GPS-stationer sat op i Grønland. Oprindeligt var formålet med GPS-stationerne at måle bevægelser i det Grønlandske grundfjeld, men dataen fra stationerne kan bruges til meget mere. Dataen kan for eksempel bruges til at undersøge gletsjer dynamik, kortlægge smeltesæsonen og evaluere satellitter, hvilket alt sammen er med til kaste lys over de ændringer, Grønland og Indlandsisen gennemgår. Denne viden kan potentielt forbedre de modeller, der forsøger at forudsige fremtidens globale klimaforandringer og data fra Grønlands GPS-stationer kan derfor i sidste ende give os et bedre billede af, hvordan fremtiden kommer til at se ud.

Som nævnt var det oprindelige formål med GPS-stationerne at måle bevægelse, også kaldet deformation, af det Grønlandske grundfjeld. Deformationen af grundfjeldet sker som en reaktion på ændringer i Indlandsisens masse og GPS-stationerne kan derfor for eksempel måle, at det grønlandske grundfjeld bevæger sig ned, når det sner om vinteren. Dette skyldes at sneen gør Indlandsisens masse større og dermed Indlandsisen tungere, hvilket presser grundfjeldet både under og rundt om Indlandsisen ned. På samme måde kan GPS-stationerne måle, at grundfjeldet bevæger sig op, når sne og is smelter om sommeren. Forholdet mellem grundfjeldets deformation og ændringer i Indlandsisens masse er lineært, og det er derfor blandt andet muligt at undersøge, hvor lang tid der går fra istykkelsen bliver mindre til ishastighed bliver højere, hvis man sammenligner grundfjelds deformation med gletsjerhastighed, hvilket potentielt kan bidrage til den generelle forståelse af gletsjerdynamik.

Udover at måle grundfjelds deformation kan dataen fra GPS-netværket bruges til at måle snedybde, da en ny teknik gør det muligt at måle afstanden mellem en GPS-station og den omkringliggende sne overflade. Snedybden kan afsløre, hvornår smeltesæsonen starter, de steder hvor der falder meget sne. Da en stor del af den grønlandske kystlinje er ubeboedet og afsondret det meste af året, kan kortlæggelse af smeltesæsonen ved hjælp af GPS-data give indsigt i lokale klimaforhold, der ellers ville være ukendte.

Udover det eksisterende GPS-netværk på grundfjeld er der flere gange, med forskellige formål og tidsperioder, installeret GPS-stationer på Indlandsisen. De GPS-stationer, der har stået på Indlandsisen i længst tid, giver en unik mulighed for at evaluere, hvor gode satellitter er til at måle ændringer i Indlandsisens højde, da en GPS-station måler både hurtige og langsomme ændringer. Den årlige ændring af Indlandsisens højde er en af de parametre, der bruges til at estimere det årlige massetab og dermed Indlandsisens årlige bidrag til den globale havniveaustigning. Selvom en GPS-station måler isens højde ændringen mere præcist end satellitter, er satellitter den eneste mulighed når det kommer til at undersøge hele Indlandsisen, da man ville skulle sætte over 1 million GPS-stationer op for at dække det samme område.

Technical
University of
Denmark

Elektrovej, building 327 and 328
2800 Kgs. Lyngby
Tlf. 4525 1700

www.space.dtu.dk